

NASA Contractor Report 4601

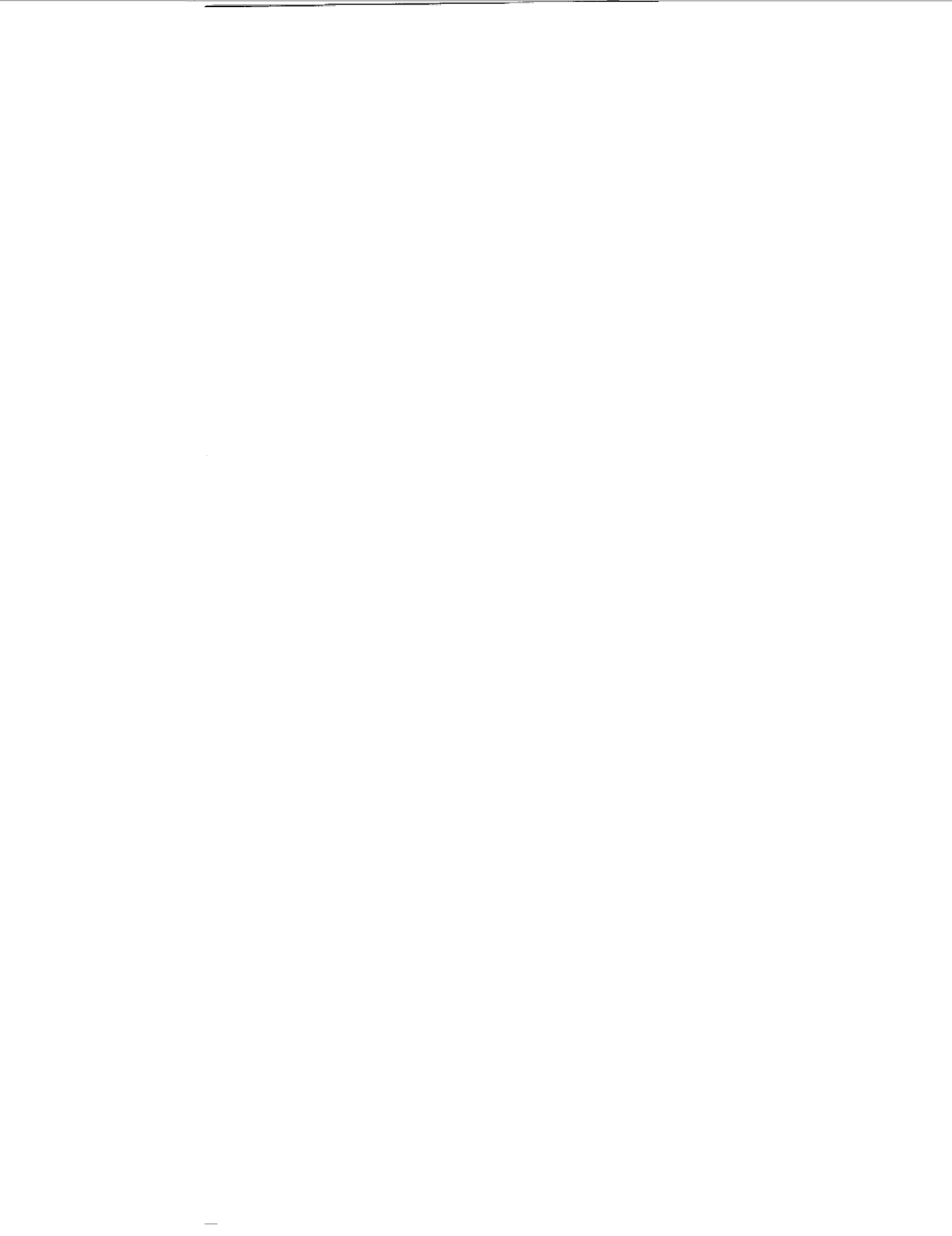
Effects of Fiber, Matrix, and Interphase on Carbon Fiber Composite Compression Strength

*John A. Nairn, Sheila I. Harper, and Willard D. Bascom
University of Utah • Salt Lake City, Utah*

National Aeronautics and Space Administration
Langley Research Center • Hampton, Virginia 23681-0001

Prepared for Langley Research Center
under Contract NAS1-18883

May 1994



Contents

1	Summary	3
2	Single-Fiber Interfacial Tests	9
2.1	Introduction	9
2.2	Materials and Methods	10
2.3	Results	16
2.3.1	Microtensile Testing	16
2.3.2	Microcomposite Compression Testing	19
2.4	Discussion and Conclusions	29
3	Single-Ply Compression Tests	47
3.1	Introduction	47
3.2	Single-Ply Compression Test Method	47
3.3	Materials	52
3.4	Experimental Observations and Results	53
3.5	Conclusions	66
4	Laminate Compression Strength	67
4.1	Introduction	67

4.2	Materials and Methods	67
4.3	Results	68
4.4	Discussion and Conclusions	70
5	Interface and Its Effect on Compression Strength	73
5.1	Introduction	73
5.2	Materials and Methods	75
5.3	Results and Discussion	83
5.3.1	Transverse Fracture Toughness	83
5.3.2	Microscopy	86
5.3.3	Compression Strength Testing	88
5.4	Conclusions	91
6	Mixed-Mode Precracking	95
6.1	Introduction	95
6.2	Materials and Methods	96
6.3	Experimental Results	99
6.4	Discussion and Conclusions	104
7	Bibliography	107

Chapter 1

Summary

One of the first fundamental results on the compression strength of composites was derived by Rosen in the early 1960's [1]. Rosen modeled a unidirectional composite as a two-dimensional array of parallel plates embedded in an elastic foundation (the matrix). Assuming that compression failure occurs when the plates initiate in-phase buckling, the compression strength, σ_c , of the model composite is

$$\sigma_c = \frac{G_m}{(1 - V_f)} \quad (1.1)$$

where G_m is the shear modulus of the matrix and V_f is the volume fraction of the fibers. Equation (1.1) is a simple and yet profound result. It shed much light on the mechanism of compression failure in composites. Unfortunately, Eq. (1.1) is an oversimplification. We can understand its problems by examining what is *not* included: σ_c is independent of the fiber properties and only depends on the *amount* of fiber; and σ_c is independent of the properties of the fiber/matrix interface. Since Rosen's work [1], there have been various attempts at more realistic models of compression failure. Most of these models build on the buckling model by including such effects as fiber waviness or matrix yielding. Very few models directly address fiber properties. To our knowledge, no models explicitly include the role of the fiber/matrix interface in compression failure.

Although buckling models, like Rosen's model [1], do not include the fiber or interface properties,

there are scattered reports in the literature of fiber and interface effects. For example, Ewins and Potter [42] measured the compression strength as a function of temperature in side-supported composites. At low temperatures the compression strength was controlled by shear fracture of the fibers; at high temperatures the compression strength was limited by the matrix support (*i.e.*, the Rosen buckling model). Although Ref. [42] strongly suggests that compression strength depends on fiber, matrix, and interface properties, changing the temperature simultaneously changes matrix properties and interface properties. It is thus not possible to definitively implicate one specific mechanism for compression failure of their materials. A major goal of this project was to get basic information on compression failure properties. In particular we wanted to investigate fiber effects, matrix effects, and fiber/matrix interface effects.

To investigate fiber effects we prepared a range of specimens using a set of nine specific fiber types. For best control of fiber types, we collaborated with Hercules through a subcontract. They supplied nine carbon fiber types summarized in Table 1.1: AS4, AS4G, AS4F, IM7, IM7G, IM7F, HMS4, HMS4G, and HMS4F. AS4, IM7, and HMS4 are Hercules fibers with a low modulus, intermediate modulus, and high modulus, respectively. Fibers followed by a "G" are fibers supplied with an epoxy-compatible "G" sizing; fibers followed by an "F" are fibers coated with a release agent Frekote 700; fibers without any additional designation are unsized and uncoated fibers. The above fiber types were each prepared in a single batch by Hercules. Using single batches eliminated batch-to-batch variations.

Samples of the Hercules-supplied fibers were analyzed for surface chemical composition using X-ray photoelectron spectroscopy. The results are listed in Tables 1.1 and 1.2. The percent elemental composition for the unsized and "G"-sized fibers are consistent with published data [3, 4]. Note the high silicon content on the AS4F, IM7F and HMS4F fibers. From Table 1.2, the silicon is present as an organo-silicon moiety, *i.e.* -Si-O-C-. These results indicate that the release agent coating

Table 1.1: Elemental surface analysis of carbon fibers supplied by Hercules (atomic elemental %)

Fiber	C	O	N	Si	Na	Cl	F	Ca
AS4	84	9.1	4.8	0.4	1.0	0.0	0.0	0.0
AS4G	82	14	2.5	0.7	0.6	0.3	0.0	0.0
AS4F	52	26	1.1	21	0.0	0.0	0.0	0.0
IM7	82	13	4.3	0.4	0.1	0.0	0.0	0.0
IM7G	84	13	3.1	0.0	0.1	0.0	0.0	0.2
IM7F	56	26	2.3	17	0.0	0.0	0.0	0.0
HMS4	93	5.1	0.0	0.3	1.4	0.1	0.0	0.0
HMS4G	88	10	0.0	0.0	1.6	0.0	0.0	0.0
HMS4F	59	22	0.0	18	0.0	0.0	0.0	0.0

Table 1.2: High Resolution ESCA for Carbon and Silicon (atomic elemental %)

Fiber	C-R or R-CH	C-OR	O-C-OR	Organic Si	SiO ₂
AS4	64	14	6.3	0.2	0.2
AS4G	61	21	0.0	0.2	0.5
AS4F	50	2.9	0.0	21	0.0
IM7	62	13	6.4	0.4	0.0
IM7F	49	5.6	0.9	17	0.0
HMS4	80	13	0.0	0.3	0.0
HMS4F	58	1.0	0.0	18	0.0

is a polysiloxane. Depth profiling of the "F" coating using Auger spectroscopy indicated that the coating was approximately 25 nm thick and was uniformly distributed.

In addition to fiber specimens, Hercules prepared prepreg material for each fiber type using Hercules 3501-6 epoxy as the matrix. We were fortunate that the preparation of the AS4F, IM7F, and HMS4F fibers and prepreg corresponded to a time when Hercules was planning to rebuild a fiber line. Had no such rebuild been anticipated, it is unlikely that Hercules would have been willing to risk possible contamination of release agent into their fiber or prepreg products. Because we were able to get "F" series fibers and prepreg, this project had a unique opportunity to study the effect of dramatic changes in the interface on compression strength.

We used the fibers and the prepreg material to produce embedded single fiber specimens (see Chapter 2), to cure single-ply specimens (see Chapter 3), and to produce full laminates (see Chapter 4). We tested all these specimens in compression. These results gave us information from the single fiber level through the ply level and up to the laminate level.

Chapter 2 describes single fiber fragmentation tests on the Hercules fibers and on some additional Amoco fibers. We did both tension tests and compression tests. A standard analysis of tension single fiber fragmentation tests suggests that the interface with unsized and "G" sized AS4 and IM7 fibers is good. In contrast, the interface with unsized and "G" sized HMS4 fibers is poor. The "F" coating had a dramatic effect on the interface with all fiber types. The simplest interpretation is that the "F" coating destroyed the interface giving effectively a zero interfacial strength. The compression results gave similar results with regards to interfacial properties. Besides standard fragmentation test analysis, we attempted to get additional information by measuring the fragmentation density as a function of strain from low strain up to the strain at which the fragmentation process ceases. The low crack density data gave us information about the distribution of flaws in the various fiber types. We suggest that there is potential for making use of low crack density data

to learn about fiber failure and fiber/matrix interfacial properties.

Chapter 3 describes compression experiments on single plies of the nine Hercules prepreg materials and of a few other materials. In brief, single plies were embedded in an epoxy and then end-loaded in compression while side supported. One of the side supports was made of transparent poly-methyl-methacrylate which permitted direct observation of the compression failure process. The single-ply results show that compression failure can be influenced by fiber type, by matrix type, and also by interfacial properties. A good correlation between interfacial properties reported in Chapter 2 and compression strengths reported in Chapter 3 was found. This correlation together with observations of failure suggested that the poor compression strength of HMS4 composites was due to a poor interface between HMS4 fiber and epoxy matrix and not to an inherent compression weakness of HMS4 fibers. The strong effect that the interface has on compression failure mechanisms was evident by examining kink-band damage zones. Composites with a poor interface had long kink band zones and composites with a good interface had short kink band zones.

Chapter 4 describes experiments on laminates made from the nine Hercules prepreg types. The results mostly agree with the results from the single-ply experiments, although the ultimate compression strengths of the laminates were higher than those of the single-ply specimens. Again, we found a strong effect of the interfacial properties. In retrospect, we could have done a reasonable job of predicting the relative compression strengths for each laminate type solely on the basis of the single-fiber experiments in Chapter 2.

The results in Chapters 3 and 4 strongly implicate the role of the interface in compression failure of composites. Unfortunately, with the Hercules material we were only able to test good and bad interfaces; we were not able to systematically control the interface. Chapter 5 describes a series of experiments on home-made carbon fiber/polycarbonate composites. Following the work of Brady and Porter [5, 6], we showed that annealing of carbon fiber/polycarbonate composites systematically

improves the fiber/matrix interface. The changes in the interfacial properties directly correlated with changes in the compression strength properties of these laminates.

The last chapter (Chapter 6) is a departure from the compression testing of the other chapters. It describes the new direction that this contract was taking before the untimely passing of the principal investigator (Prof. Willard D. Bascom). We subjected various laminates to precracking under mixed-mode loading conditions. Following the mixed-mode precracking, the laminates were subjected to standard mode I delamination testing. We found a large effect of the precracking conditions on the mode I toughness of the laminates. The most dramatic effect was after precracking of composites with a rubber-toughened epoxy matrix or with rubber-toughening interlayers between the plies. Following precracking with predominantly mode II loading, the mode I toughness of the toughened laminates was actually lower than comparable toughness of brittle-matrix laminates. These results suggest care is required when verifying the performance of toughened composites.

Chapter 2

Single-Fiber Interfacial Tests

2.1 Introduction

Many investigators have attempted to characterize the fiber/matrix interphase region of carbon fiber reinforced plastics. Several characterization techniques are based on single-fiber tests. These tests are direct tests that load a single fiber-matrix interface until failure and attempt to reduce the results to calculate an interfacial shear strength. The four most popular single-fiber methods are [7]:

1. fiber pull-out;
2. microbond;
3. single-fiber fragmentation; and
4. microindentation.

A sizable body of data for a number of carbon fiber types in a variety of matrix materials has been collected using method 3—the single-fiber fragmentation method [8–18]. Much of this data, however, is qualitative in nature because the data analyses have been restricted to simplistic elastic-plastic or to one-dimensional shear-lag analyses.

The single-fiber fragmentation tests described here attempt to go beyond the literature results, which only determined critical fiber lengths for high performance graphite fibers. We measured fiber crack density as a function of applied stress in both tension and compression. This technique contrasts with most literature results on the single-fiber fragmentation test which *only* measure the critical fragment length or the fiber crack density after the fragmentation process ceases. We attempted to make use of the extra data at low crack density to learn more about the fiber properties and more about the interfacial properties. We used some recent variational mechanics results on the single-fiber fragmentation test [19] to guide us in evaluating the experimental results. Results from seven of the nine Hercules fibers discussed in Chapter 1 and from some Amoco fibers are presented.

2.2 Materials and Methods

The carbon fibers used in the single-fiber experiments and their sizings or coatings are listed in Table 2.1. The T650 fibers manufactured by Amoco and all Hercules fibers were produced from a polyacrylonitrile (PAN) precursor. The T1000 fibers were manufactured from a different precursor. All fiber types were supplied as tows. A UC-309 designation following the Amoco fiber types indicates an epoxy-compatible sizing. A "G" following a Hercules fiber type designates Hercules's commercial, epoxy-compatible, "G" sizing. An "F" designates a fiber coated with Frekote 700, a siloxane-based release coating. Those fiber types which have none of these designations were unsized and uncoated.

The single-fiber specimens were made by embedding single fibers in an epoxy matrix material consisting of diglycidylether of Bisphenol A (DGEBA, Shell Epon 828) cured with 14 phr metaphenylene diamine (m-PDA).

Table 2.1: Graphite fibers used for interfacial tests

Fiber Type	Manufacturer	Diameter (μm)	Coating	Sizing
T1000 12K UC-309	Amoco	N/A	No	Yes
T650/50X 12K UC-309	Amoco	N/A	No	Yes
T650/50X 12K	Amoco	N/A	No	No
T650/42 12K UC-309	Amoco	N/A	No	Yes
T650/35 6K UC-309	Amoco	N/A	No	Yes
T650/35 6K	Amoco	N/A	No	No
AS4	Hercules	6.96	No	No
AS4G	Hercules	6.96	No	Yes
AS4F	Hercules	6.96	Yes	No
IM7	Hercules	5.00	No	No
IM7G	Hercules	5.00	No	Yes
IM7F	Hercules	5.00	Yes	No
HMS4	Hercules	7.4	No	No

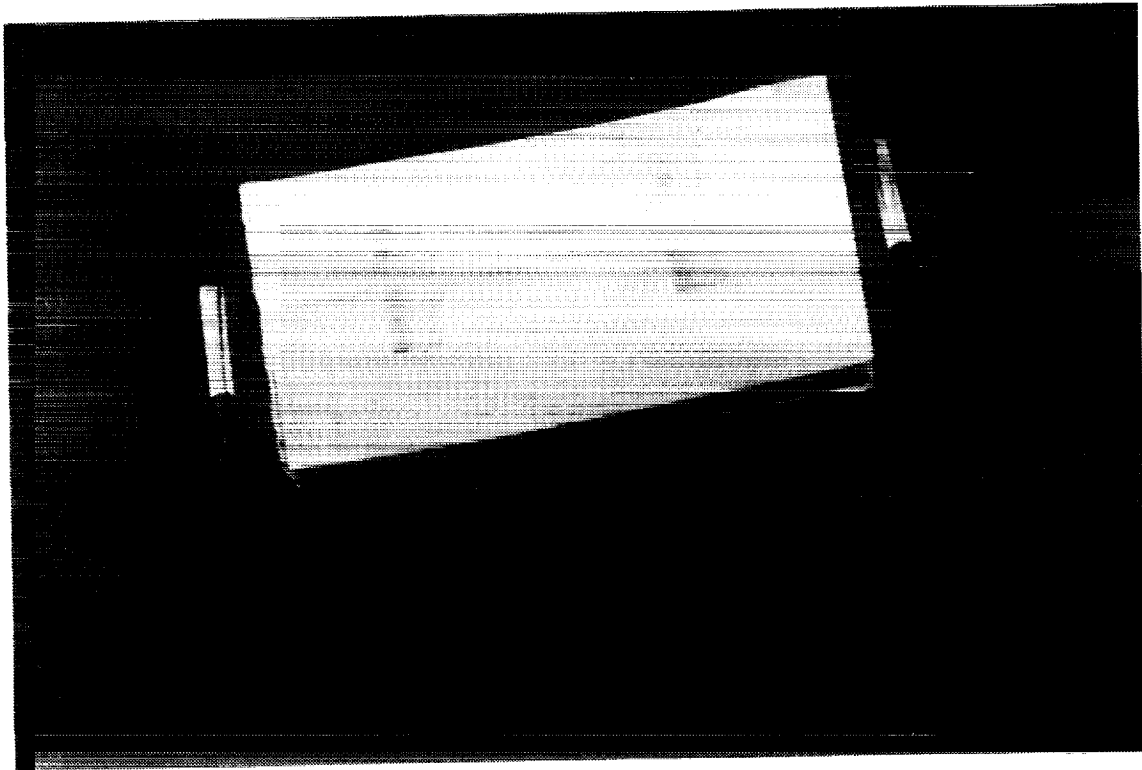


Figure 2.1: Single fiber positioned in a dog bone mold.

Fabrication of tensile dog bones was accomplished using single-cavity, silicone molds. The molds were constructed by pouring liquid silicone rubber into a preform and then placing a standard ASTM tensile dog bone blank in the center of the preform, level with the top surface. Following an eight hour cure cycle at a temperature of 125°C, the dog bone blank was removed from the preform and sprue slots were cut in the center of the mold at each end of the dog bone to an approximate depth of 1/32 inch.

Sections of fiber tows six to eight inches in length were placed on a clean, white surface with one end of the tow secured by a piece of double-faced tape. Single filaments were then selected from the tow section by hand using extreme care to avoid contamination of the gage-length zone of the single-fiber specimens. After removing the single filament from the tow, its ends were secured to a U-shaped wire using rubber cement. The U-shaped wire acted as a support for positioning the fiber in the sprue slots of the dog bone mold as depicted in Fig. 2.1.

After positioning the fibers in the mold, a resin mixture was prepared and degassed under vacuum to remove entrapped air. Addition of resin to the mold was accomplished in one continuous motion to prevent movement of the fiber. Any air bubbles introduced by this procedure were removed by hand with a wooden stick before beginning the cure cycle. The cast specimens were cured in a non-circulating oven for two hours at 75°C followed by three hours at 125°C. Additional information about the specimen fabrication method may be obtained from Ref. [13].

Tensile testing was performed using a motor-driven microtensile testing device equipped with a linear variable displacement transducer (LVDT) for measuring strain. The apparatus is depicted in Fig. 2.2. In a routine microtensile test, the dog bone specimen was elongated to a predetermined level of strain and statically maintained. Fragmentation of the embedded single fiber was observed at each strain level by placing the microtensile testing device on the stage of an optical microscope and illuminating the transparent specimen with polychromatic light. Crossed polarizing filters were used to observe the resultant stress birefringent patterns and fragment lengths were determined by measuring the distances between these patterns using a calibrated graticule mounted in the eyepiece of the microscope.

Although the specimen testing configuration of the microcomposite compression specimen was different than the tensile specimen, the fabrication method was identical. The cured compression specimens were nominally 3.56 cm in length, 1.0 cm in width, and 0.4 cm thick before grinding and polishing. After grinding and polishing to remove flashing and level any crown due to meniscus curvature of the epoxy liquid, the nominal thickness decreased to 0.29 cm.

The complete compression testing apparatus, as it appears when mounted on an optical bench, is depicted in Fig. 2.3. A close-up view of the compression loading fixture is shown in Fig. 2.4. Microcomposite compression specimens were placed in the side-supporting key-ways with a clearance of approximately 0.0012 mm. Load was applied hydraulically through an actuator (see Fig. 2.4)

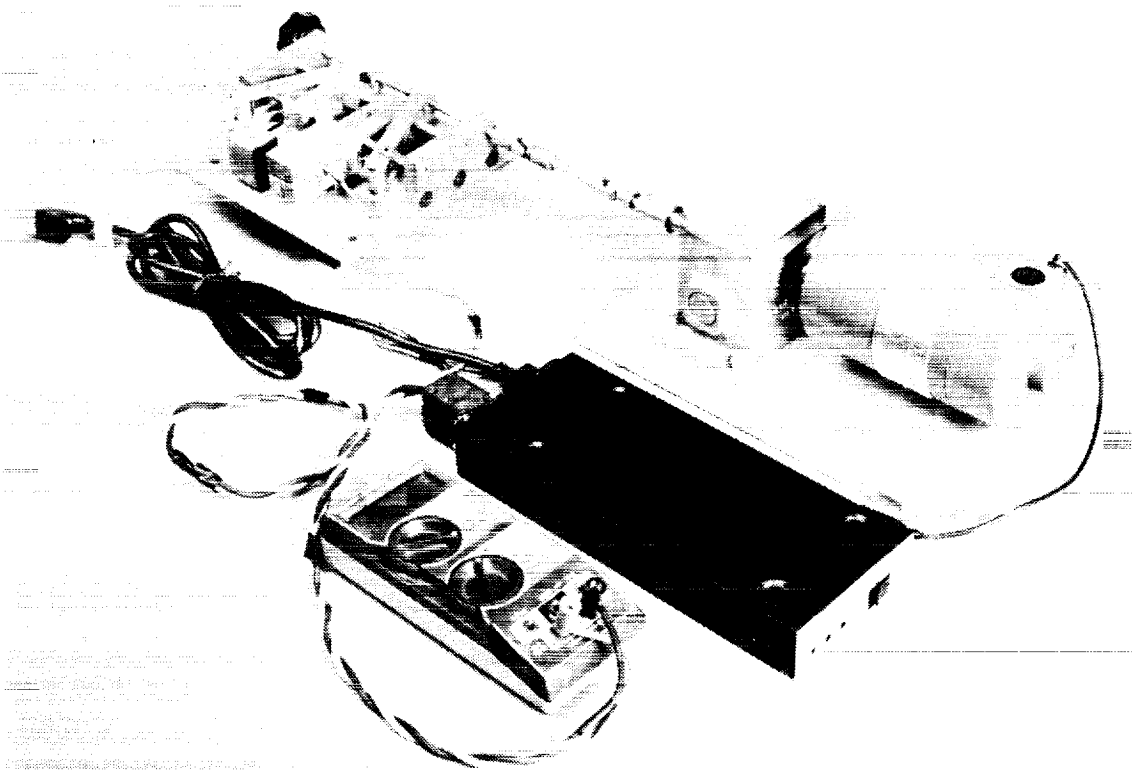


Figure 2.2: Microtensile test device.

to a steel bar (see Item B, Fig. 2.4) in contact with the specimen. A piezoelectric transducer (see Item C, Fig. 2.4) was used to detect the applied load and the analog signal output was directed to an x - y recorder for recording of a load-time trace.

During a typical compression test, the specimen was loaded to a predetermined stress level and static loading was maintained while the embedded fiber was observed using a light microscope equipped with a long working distance objective. A space between the side supports of the key way permitted light to be transmitted through the specimen. By introducing crossed polarizing filters into the light path, stress birefringent patterns were observed. Fragment lengths were determined by measuring the distances between the birefringent patterns using a calibrated graticule mounted in the eyepiece of the microscope.

It should be noted that none of the apparatuses described here are commercially-available. Both the microtensile testing device and the microcomposite compression device were custom designed

ORIGINAL PAGE
BLACK AND WHITE PHOTOGRAPH

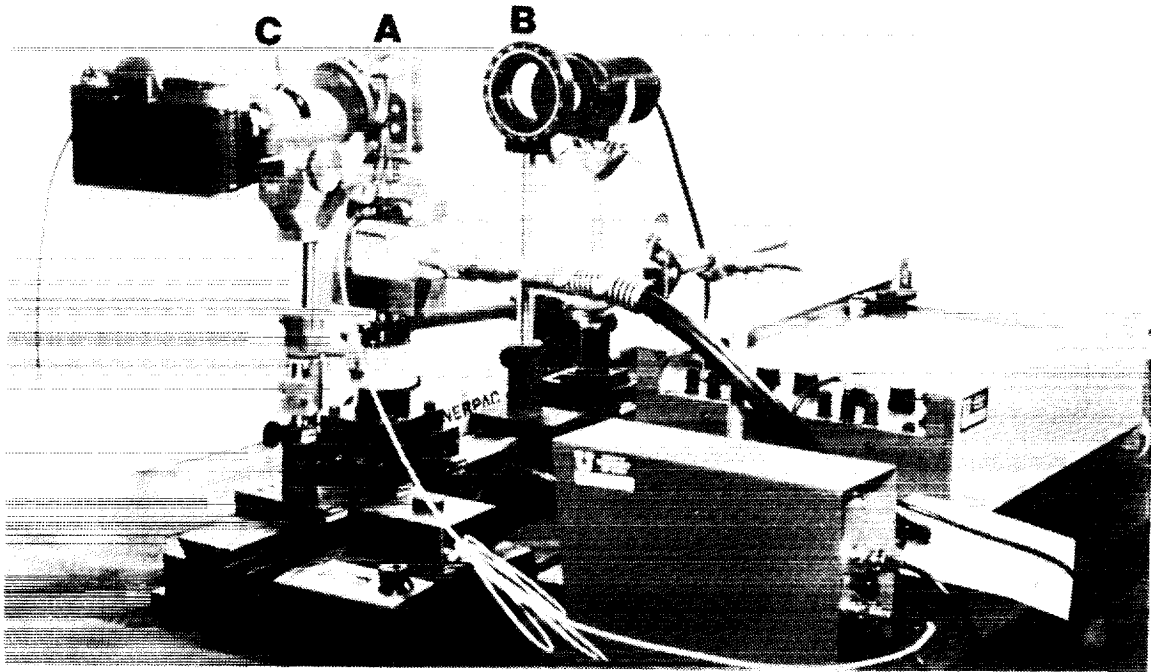


Figure 2.3: Optical bench for compression testing of microcomposites: A) compression test fixture; B) graduated polarizing fixture; and C) analyzer. (Not shown is a light condenser that fits between the polarizer and test fixture.)

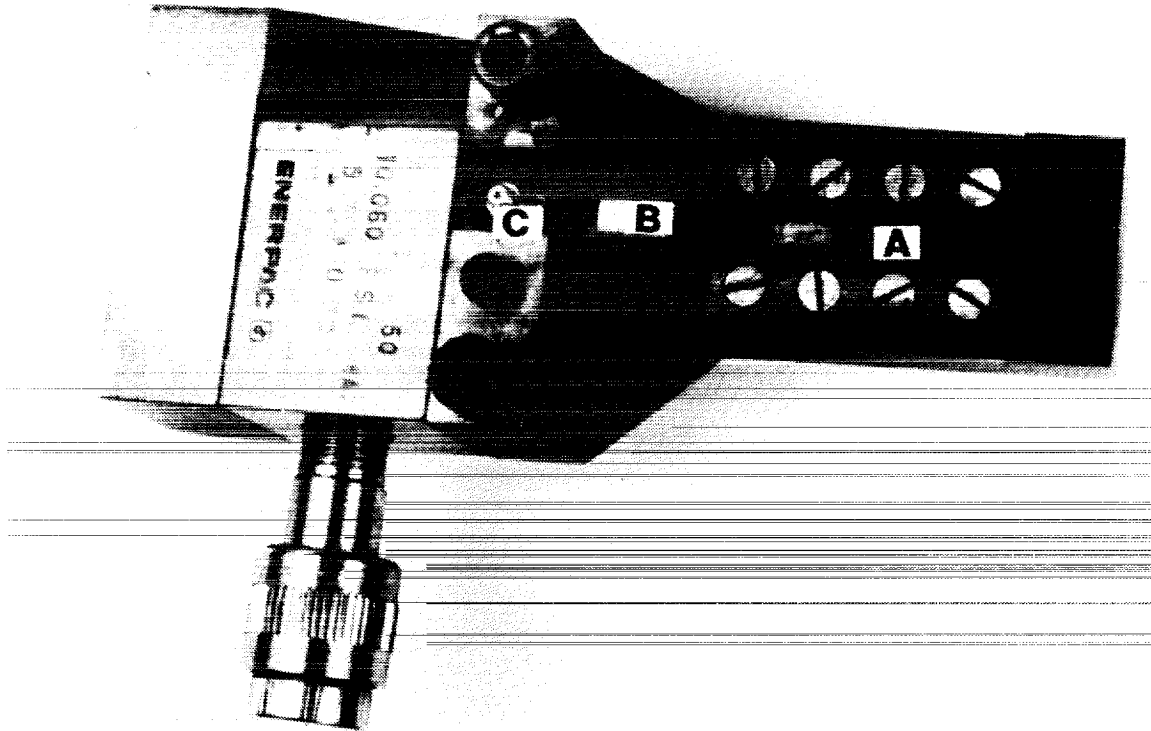


Figure 2.4: Hydraulic test device for compression testing: A) sample; B) steel bar; and C) stress transducer.

and fabricated for this project.

2.3 Results

2.3.1 Microtensile Testing

Microtensile testing of Hercules fibers included the following fiber types: AS4, AS4G, AS4F, IM7, IM7G, and IM7F [20]. The birefringent patterns associated with an induced stress field were observed for these fibers following the methods of Bascom and Jensen [13]. These patterns were found to be similar for the AS4, AS4G, IM7, and IM7G fibers. Typical birefringence patterns are shown in Fig. 2.5. During testing of AS4F and IM7F fibers, no birefringence patterns were observed. The lack of birefringence patterns was due to there being insufficient fiber/matrix adhesion to cause even a single fiber break. In other words, the embedding epoxy failed before any fiber fractures

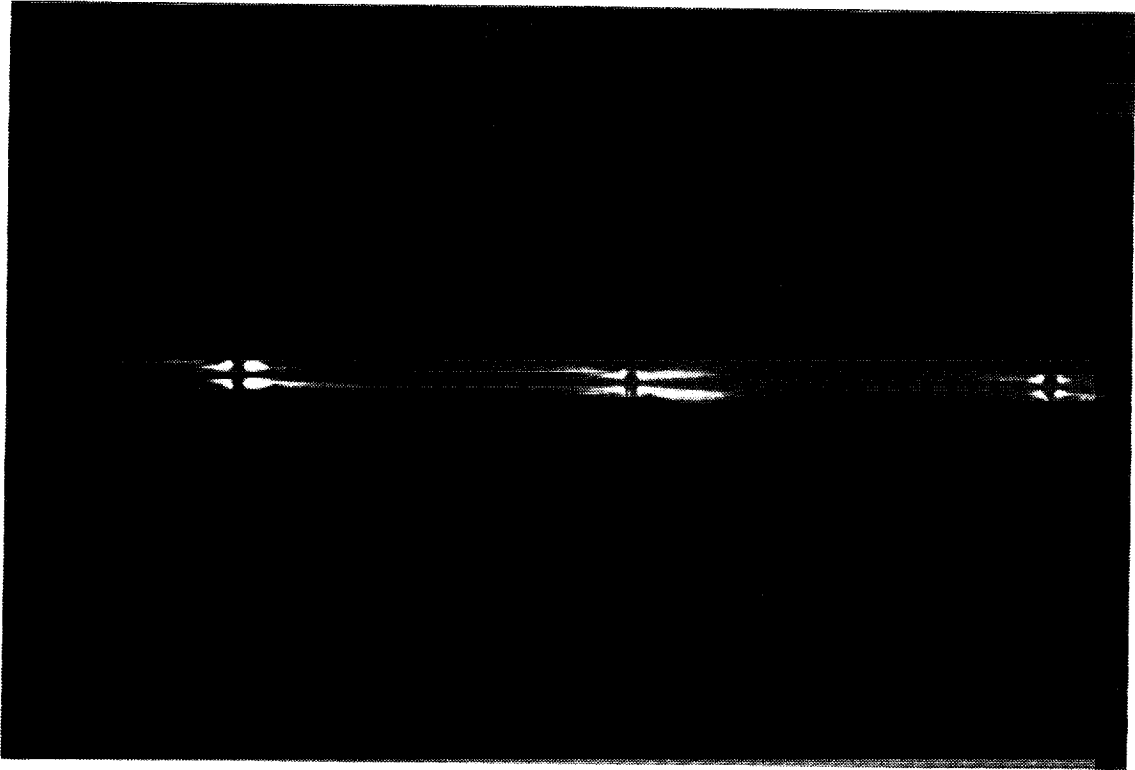


Figure 2.5: Stress birefringent pattern of an AS4 carbon fiber.

occurred. Alternatively, the critical length for these specimens was longer than the gage length of the specimen.

The average fragment length and its standard deviation at six levels of strain for the sized and unsized AS4 and IM7 fibers are given in Table 2.2 (data from Ref. [20]). The percent strains were calculated from the voltage output of the displacement LVDT. The stresses are fiber stresses; these were calculated from the strain using a variational mechanics stress analysis and the fiber and matrix material properties [19]. Fiber crack density (breaks per millimeter) was determined by calculating the inverse of the average fragment length.

Figures 2.6–2.9 plot the raw data as the fiber crack density (or breaks/mm) as a function of fiber stress for AS4, AS4G, IM7, and IM7G fibers, respectively. All results followed the same pattern. At low stress there were no breaks in the fibers; at some critical stress, fiber breaks begin to appear and their numbers increase roughly linearly with increasing stress; at high stress the linear increase

Table 2.2: Critical fragment length data for Hercules graphite fibers

		Percent Strain					
		3.04	3.34	3.65	3.95	4.26	4.56
AS4	Average length (mm)	1.95	0.707	0.399	0.342	0.320	0.313
	Standard Deviation (mm)	3.065	0.381	0.091	0.059	0.043	0.042
	Breaks/mm	0.513	1.42	2.51	2.93	3.12	3.19
	Stress (MPa)	376.1	405.7	432.5	464.4	499.9	535.5
AS4G	Average length (mm)	4.00	1.50	0.849	0.496	0.452	0.358
	Standard Deviation (mm)	4.88	1.46	0.685	0.236	0.089	0.057
	Breaks/mm	0.250	0.665	1.177	2.023	2.210	2.788
	Stress (MPa)	378.7	413.8	448.3	476.1	512.6	541.5
IM7	Average length (mm)	1.643	1.096	0.565	0.478	0.364	0.332
	Standard Deviation (mm)	0.988	0.611	0.233	0.163	0.069	0.043
	Breaks/mm	0.608	0.912	1.77	2.05	2.75	3.02
	Stress (MPa)	375.2	411.2	441.2	475.7	505.0	538.1
IM7G	Average length (mm)	7.13	6.66	5.74	2.19	0.455	0.332
	Standard Deviation (mm)	N/A	N/A	N/A	1.512	0.032	0.019
	Breaks/mm	0.140	0.150	0.174	0.456	2.20	3.02
	Stress (MPa)	379.8	419.4	460.2	496.2	512.7	538.1

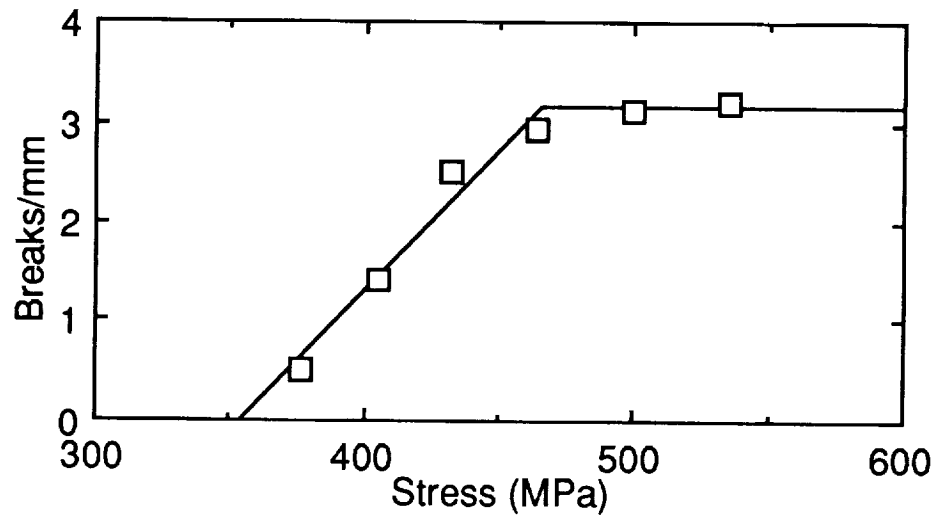


Figure 2.6: Microtensile behavior of Hercules AS4 graphite fiber (unsized) in an intermediate modulus epoxy matrix.

stops and the breaks/mm curve saturates at some critical crack density. The lines in each of these figures are “idealized” curves that represent the linear increase region and the saturation region using a bilinear fit. The significance of these types of curves will be explored in Section 2.4.

Microtensile testing of Amoco fibers included the following fiber types: T1000 12K, UC-309; T650/50X (unsized); T650/35, UC-309; and T650/42, UC-309. Testing was restricted to one strain level, therefore, only a limited data treatment is possible. The critical lengths and a qualitative assessment of the interfacial adhesion based upon birefringent patterns for these fibers are summarized in Table 2.3. Similar results for Hercules AS4 and HMS4 fibers in the same epoxy matrix have been included for comparison.

2.3.2 Microcomposite Compression Testing

Compression testing of Hercules fibers included the following fiber types: AS4, AS4G, AS4F, IM7G, and HMS4. Previous work with some of these fibers produced evidence to suggest that compression failure initiated as a microcrack which then propagated as a shear failure [21]. Although no

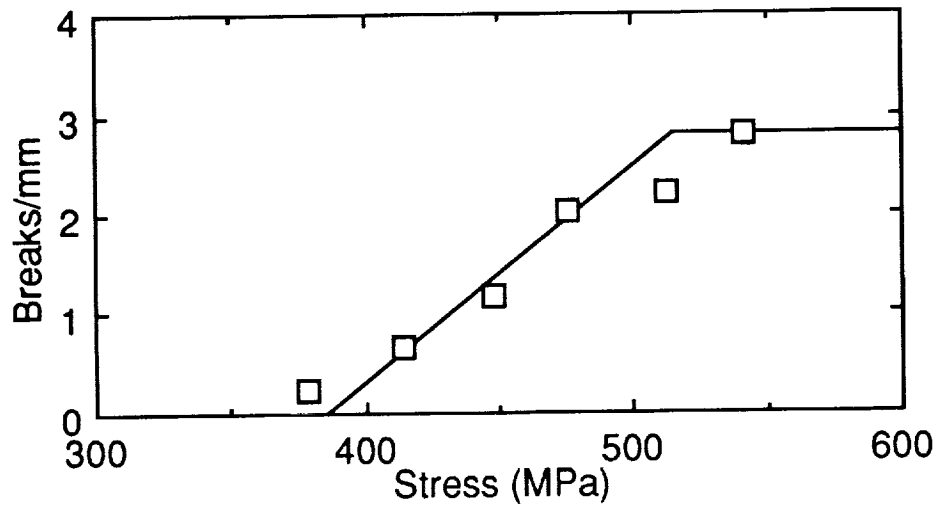


Figure 2.7: Microtensile behavior of Hercules AS4 graphite fiber with "G" size in an intermediate modulus epoxy matrix.

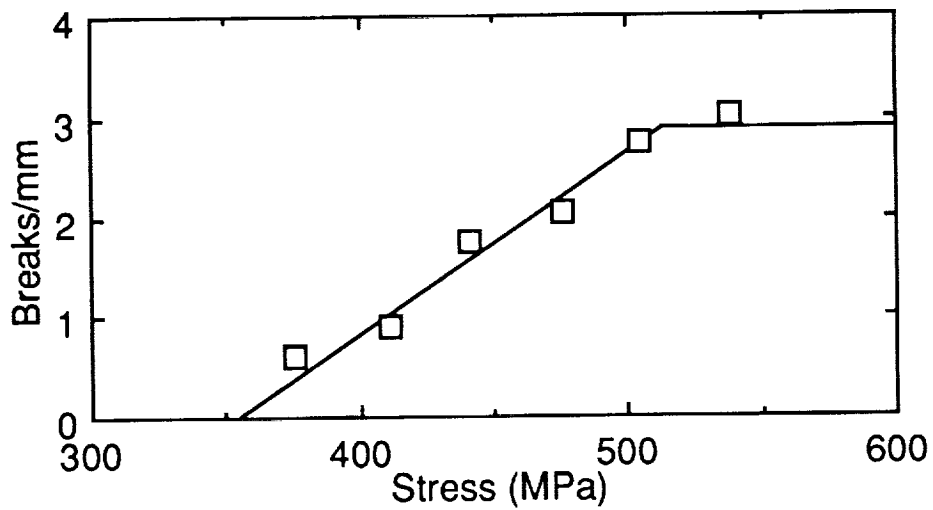


Figure 2.8: Microtensile behavior of Hercules IM7 graphite fiber (unsized) in an intermediate modulus epoxy matrix.

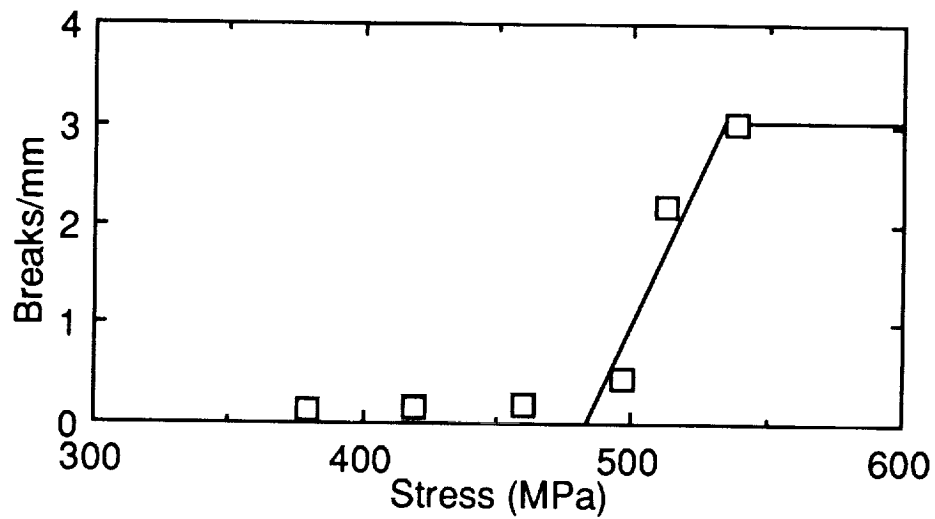


Figure 2.9: Microtensile behavior of Hercules IM7 graphite fiber with "G" size in an intermediate modulus epoxy matrix.

Table 2.3: Critical fragment length data for Amoco graphite fibers

Fiber Type	Critical Length (mm)	Standard Deviation (mm)	Adhesion
T1000 12K UC-309	0.454	0.146	Mixed
T650/50X 12K UC-309	0.554	0.197	Weak
T650/35 6K UC-309	0.403	0.115	Strong
T650/42 12K UC-309	0.357	0.105	Strong
AS4	0.411	0.141	Strong
HMS4	0.709	0.279	Weak

scanning electron microscopy (SEM) work was performed on the failed specimens from this experiment, reasonable magnification of the embedded fibers was provided with a long-working distance objective on the optical microscope used during the compression testing. Visual observations were made to assess the fiber failure mechanism at each failure initiation site. With only one possible exception, no microbuckling was observed. Fiber failure typically occurred without any prior evidence of fiber shift with respect to the vertical axis of the specimen. Furthermore, the ends of the failed fiber fragments appeared to have broken at an angle of approximately 45° with respect to the longitudinal axis of the fiber which is typical of a shear failure. The possible exception to this result was the HMS4 fiber type. It was difficult to make an accurate assessment of failure mode, however, because the sample size was limited. Furthermore, this particular fiber type exhibited more evidence of fiber crushing which may have masked other failure mechanisms.

Unlike the microtensile procedure, the crack densities (breaks per millimeter) of the microcompression samples were measured directly. Ordinarily, the overall specimen gage length would be used as the gage length of a compression coupon, however, a portion of the microcompression specimens was not visible when placed in the test fixture. A correction factor was easily determined by measuring the path length within the fixture where the specimens were obscured. This factor (a constant) was then subtracted from the overall specimen length to obtain the visible gage length. In a few instances, the overall specimen length was not measured prior to testing the specimen. The loss of valuable data was circumvented by using a "nominal" specimen length which had been determined from the average of other measured lengths. The percentage error introduced by use of a "nominal" value is estimated to be a few percent. Included in these results are two sets of data for the AS4G fiber type. The two sets of specimens were separately prepared and tested by different individuals in order to verify reproducibility and to gain insight into the magnitude of experimental error.

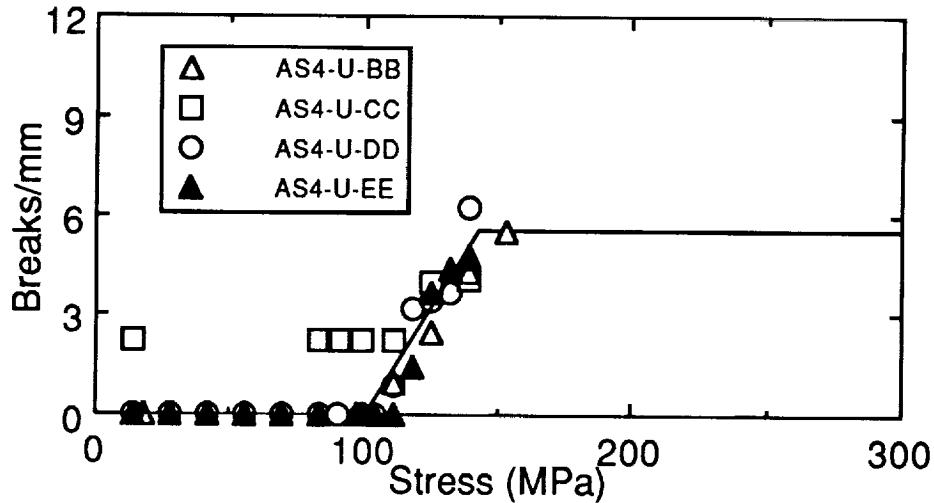


Figure 2.10: Microcompression behavior of Hercules AS4 graphite fiber (unsized) in an intermediate modulus epoxy matrix.

The fiber crack density as a function of applied compression stress for each of the Hercules fiber types is depicted in Figs. 2.10–2.15. As for the microtensile results, the bilinear fits in these figures represent an idealized behavior which has an onset period followed by a linear increase in crack density that terminates at some saturation crack density.

Fiber fragment length distributions were determined for the IM7G fiber type. These are presented as bar charts for specimens IM7G-5, -6, -7, -8, and -9 in Figs. 2.16–2.20, respectively. The stress level for each plot is indicated in the figure caption.

Compression testing of Amoco fibers included the following fiber types: T1000 12K, UC-309; T650/35 6K, UC-309; T650/42 12K, UC-309; T650/50X 12K (unsized); T650/35 12K (unsized); and T650/50 12K, UC-309. Visual observations were made to assess the fiber failure mechanism at each failure initiation site. The failure mechanisms of these fibers were more diverse than those of the Hercules fibers. There was more evidence of fiber crushing and possibly more evidence of microbuckling. A summary of these data is provided in Table 2.4.

The fiber crack density as a function of applied stress for each of the Amoco fiber types is depicted in Figs. 2.21–2.26. As before, the crack densities were measured directly. Again, the

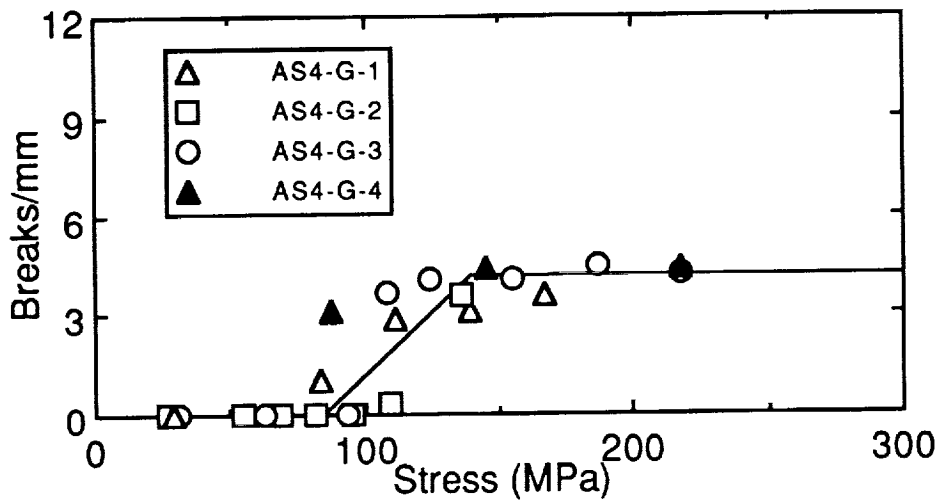


Figure 2.11: Microcompression behavior of Hercules AS4 graphite fiber with "G" size in an intermediate modulus epoxy matrix. (Test group No. 1.)

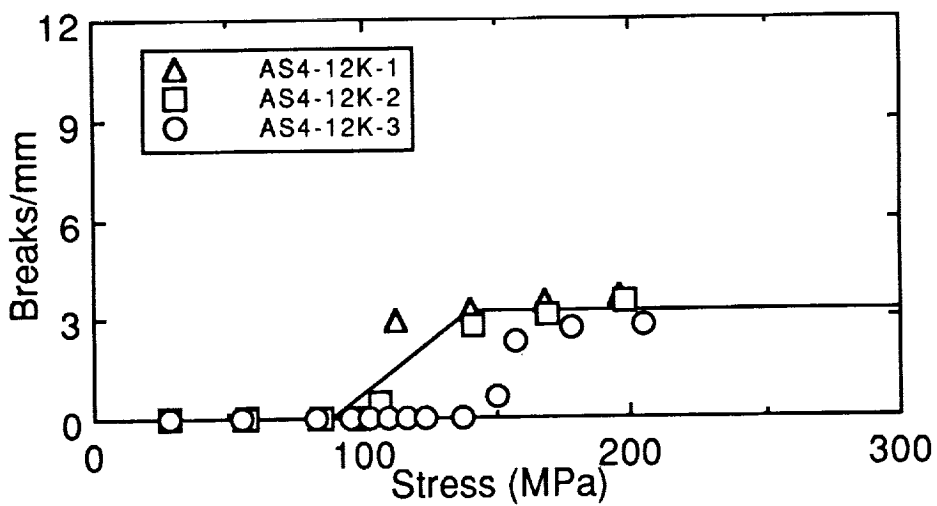


Figure 2.12: Microcompression behavior of Hercules AS4 graphite fiber with "G" size in an intermediate modulus epoxy matrix. (Test group No. 2.)

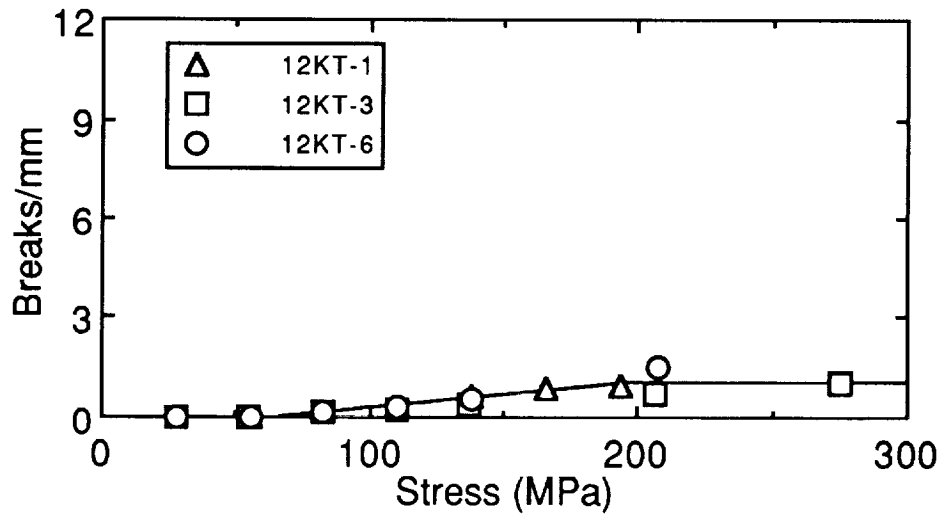


Figure 2.13: Microcompression behavior of Hercules AS4 graphite fiber coated with Frekote 700 in an intermediate modulus epoxy matrix.

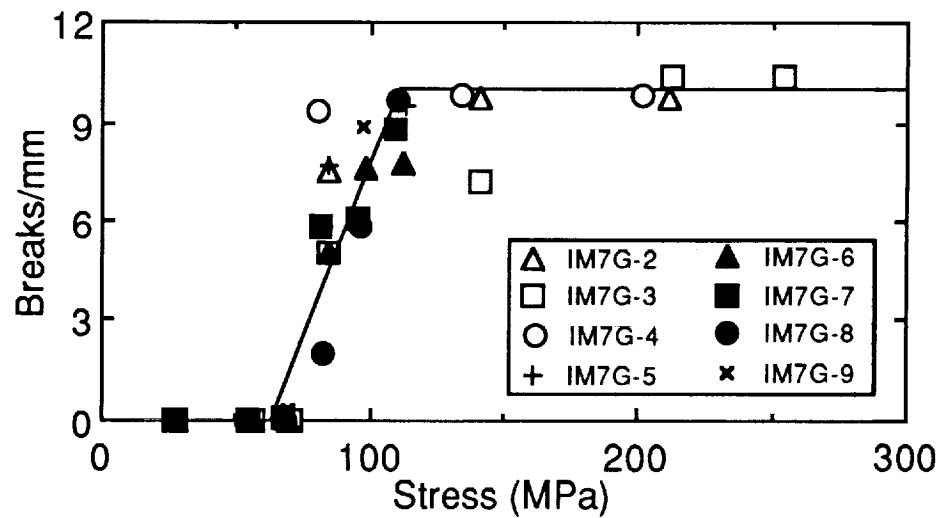


Figure 2.14: Microcompression behavior of Hercules IM7 graphite fiber with "G" size in an intermediate modulus epoxy matrix.

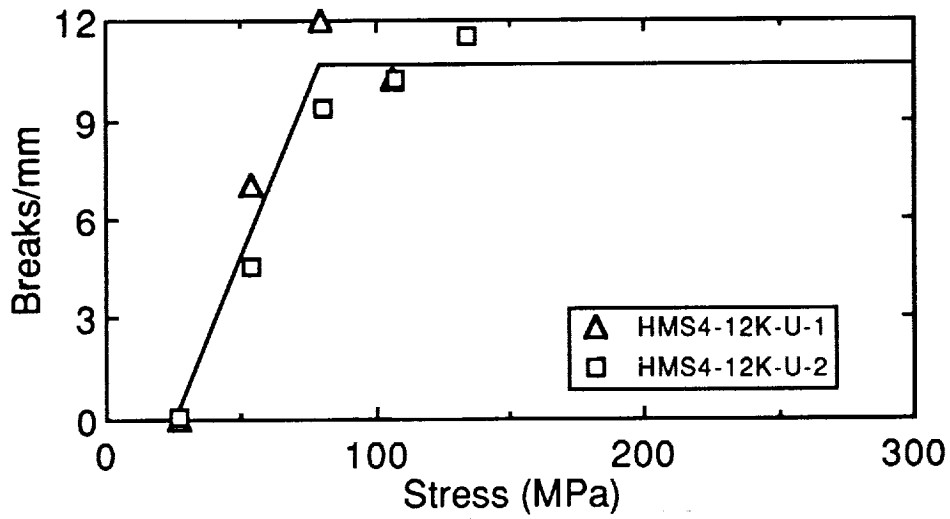


Figure 2.15: Microcompression behavior of Hercules HMS4 graphite fiber (unsized) in an intermediate modulus epoxy matrix.

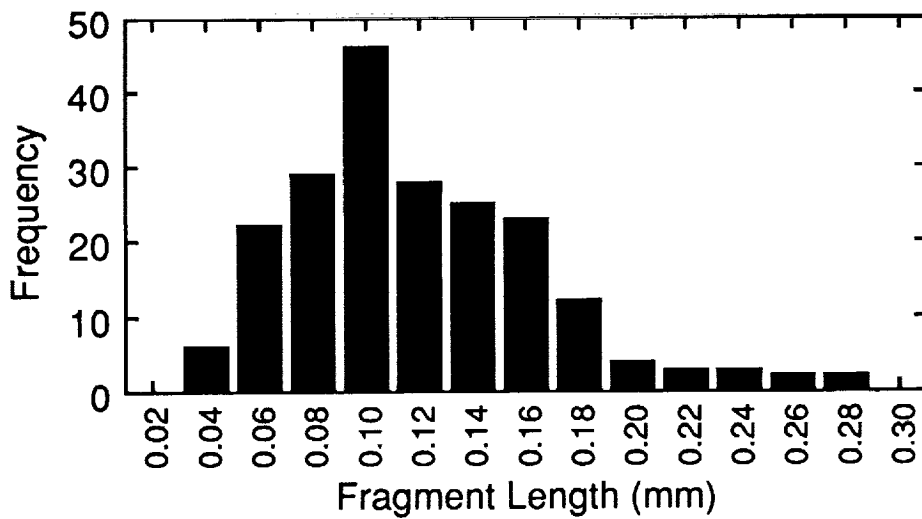


Figure 2.16: Fiber fragment length distribution for Hercules IM7 graphite fiber with "G" size in an intermediate modulus epoxy matrix. (Specimen IM7G-5 at a stress level of 85.64 MPa).

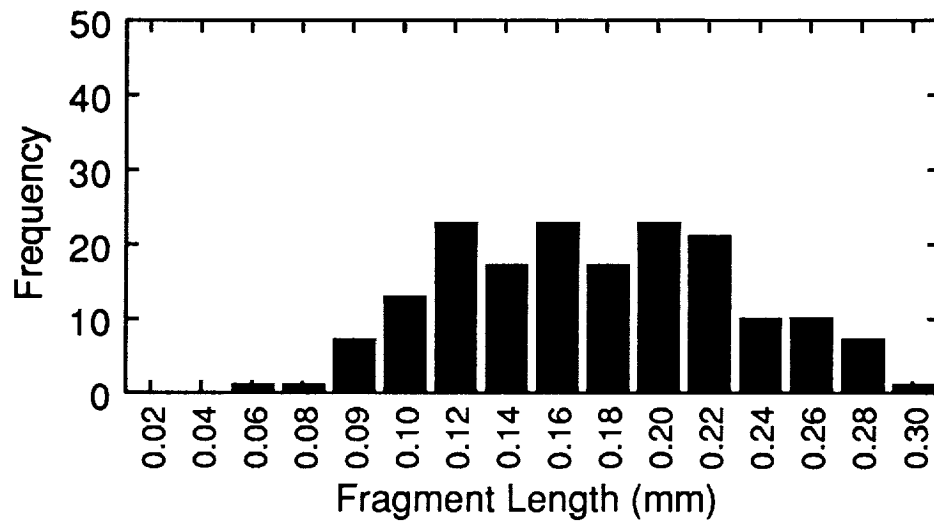


Figure 2.17: Fiber fragment length distribution for Hercules IM7 graphite fiber with “G” size in an intermediate modulus epoxy matrix. (Specimen IM7G-6 at a stress level of 83.97 MPa).

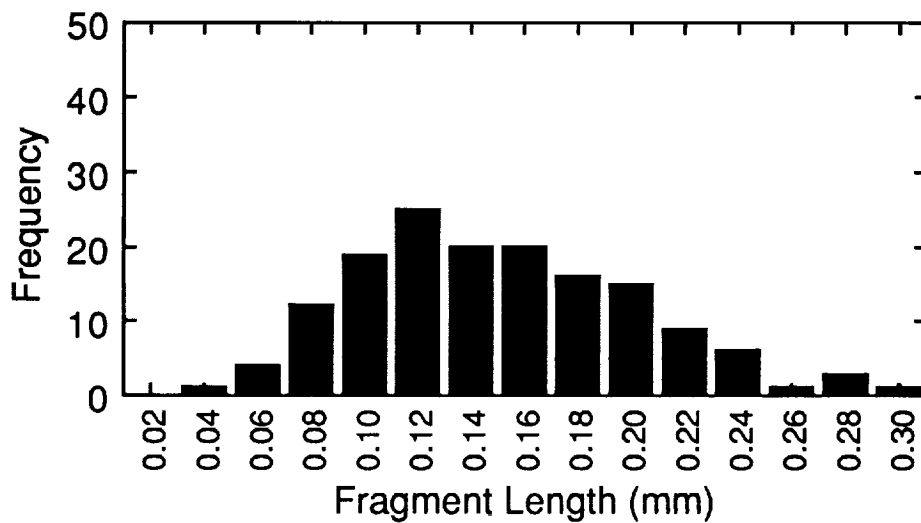


Figure 2.18: Fiber fragment length distribution for Hercules IM7 graphite fiber with “G” size in an intermediate modulus epoxy matrix. (Specimen IM7G-7 at a stress level of 81.60 MPa).

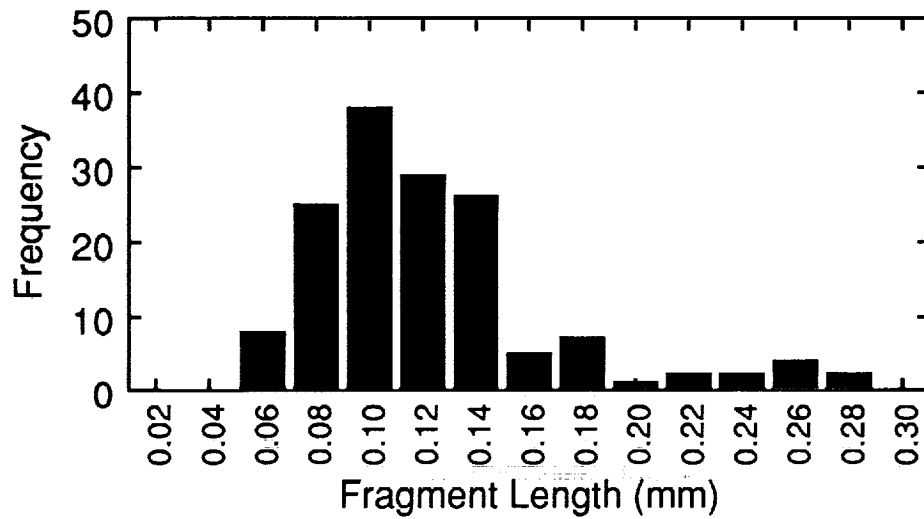


Figure 2.19: Fiber fragment length distribution for Hercules IM7 graphite fiber with “G” size in an intermediate modulus epoxy matrix. (Specimen IM7G-8 at a stress level of 96.45 MPa).

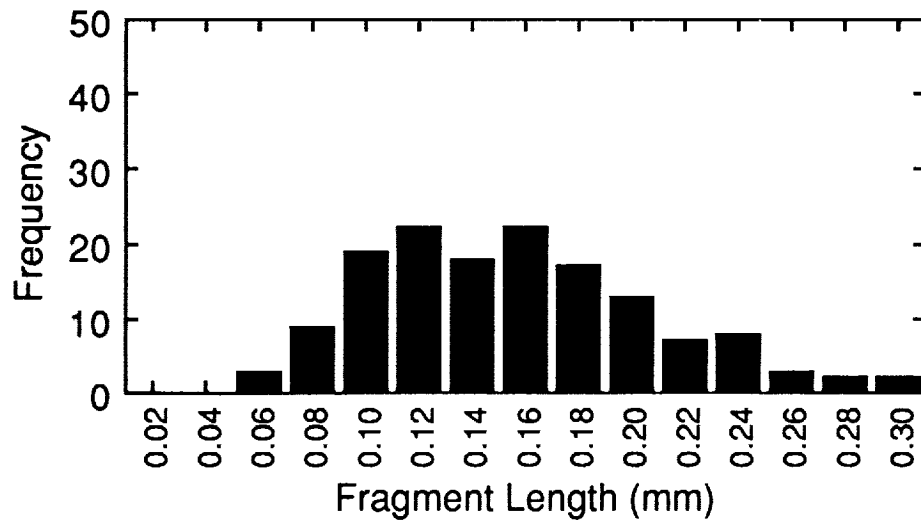


Figure 2.20: Fiber fragment length distribution for Hercules IM7 graphite fiber with “G” size in an intermediate modulus epoxy matrix. (Specimen IM7G-9 at a stress level of 83.74 MPa).

Table 2.4: Visual observations of failure mechanisms for Amoco graphite fibers

Fiber Type	Failure Mechanism(s)	Adhesion
T1000 12K, UC-309	Shear, Crushing	Poor (Weak)
T650/50X 12K, UC-309	Shear	Unknown
T650/50X 12K	Microbuckling, Shear	Unknown
T650/42 12K, UC-309	Microbuckling, Shear	Strong
T650/35 6K, UC-309	Shear, Crushing	Strong
T650/35 6K	Shear, Crushing	Intermittent (stick-slip)

bilinear fit in each of these figures represents an idealized crack density *vs.* fiber stress result.

2.4 Discussion and Conclusions

Until recently, most single-fiber fragmentation tests have focused on the fiber critical length. Little attention has been given to the manner in which the critical crack density is approached. Furthermore, most analyses of stress transfer between the matrix and the embedded fiber have relied upon simplistic, one-dimensional, shear-lag models or on elastic-plastic assumptions which fail to accurately describe the interfacial shear stress at a fiber break and breaks down completely when the applied stresses are compressive.

We believe there is important information to be gained by studying the manner in which the critical crack density is approached or, in other words, the shape of the fiber crack density *vs.* applied stress curve. In this discussion, we will give some interpretations of our results and draw some conclusions using the variational mechanics analysis in Ref. [19]. Where sufficient and appropriate data are available we will correlate these results with the more "typical" results obtained from single-fiber fragmentation tests.

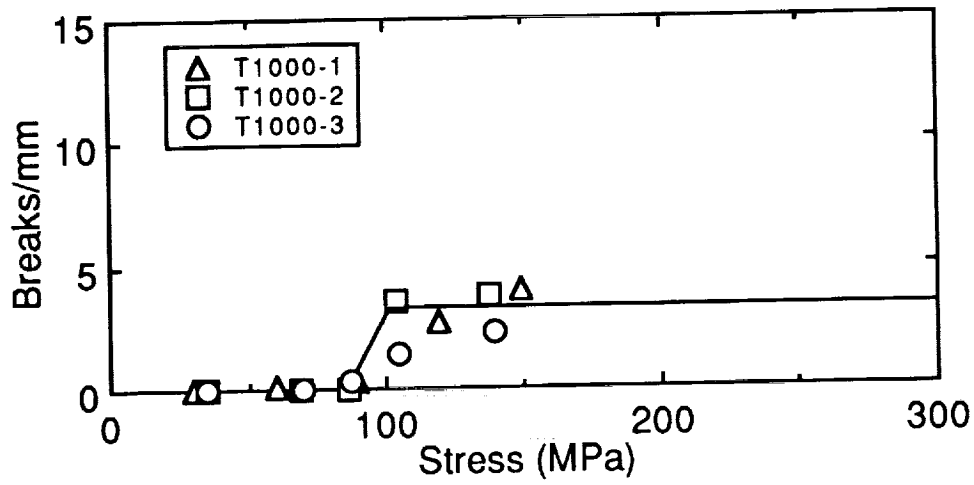


Figure 2.21: Microcompression behavior of Amoco T1000 12K graphite fiber with UC-309 size in an intermediate modulus epoxy matrix.

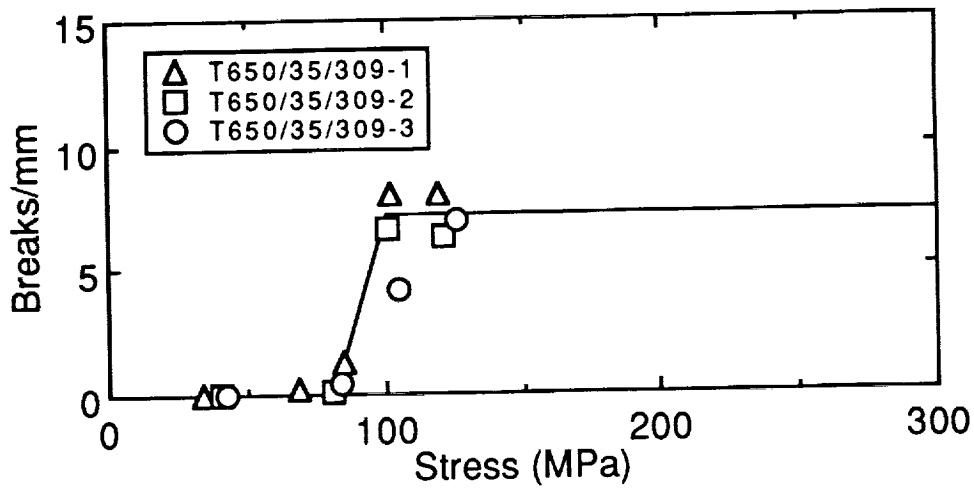


Figure 2.22: Microcompression behavior of Amoco T650/35 6K graphite fiber with UC-309 size in an intermediate modulus epoxy matrix.

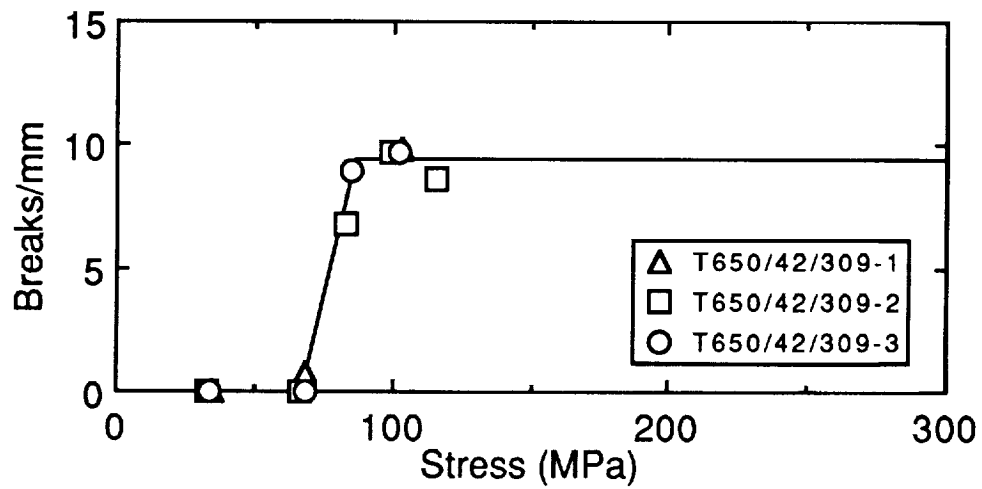


Figure 2.23: Microcompression behavior of Amoco T650/42 12K graphite fiber with UC-309 size in an intermediate modulus epoxy matrix.

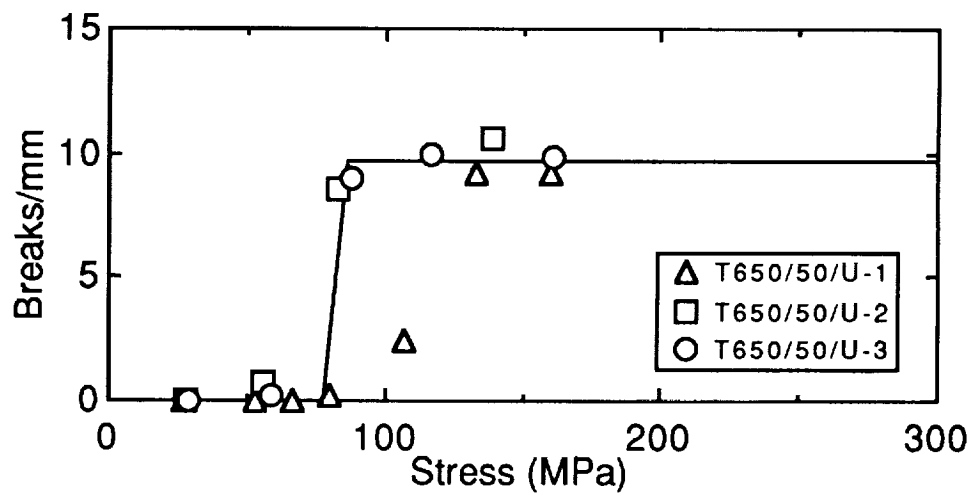


Figure 2.24: Microcompression behavior of Amoco T650/50X 12K graphite fiber (unsized) in an intermediate modulus epoxy matrix.

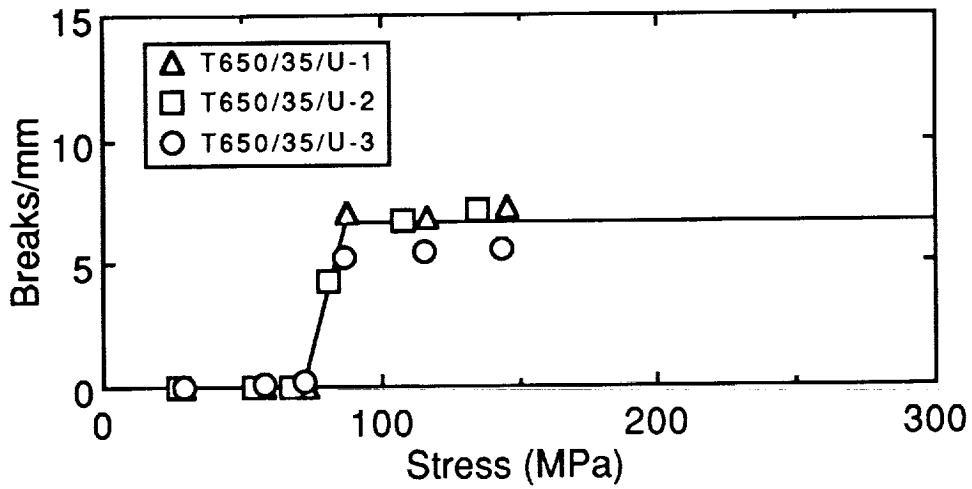


Figure 2.25: Microcompression behavior of Amoco T650/35 12K graphite fiber (unsized) in an intermediate modulus epoxy matrix.

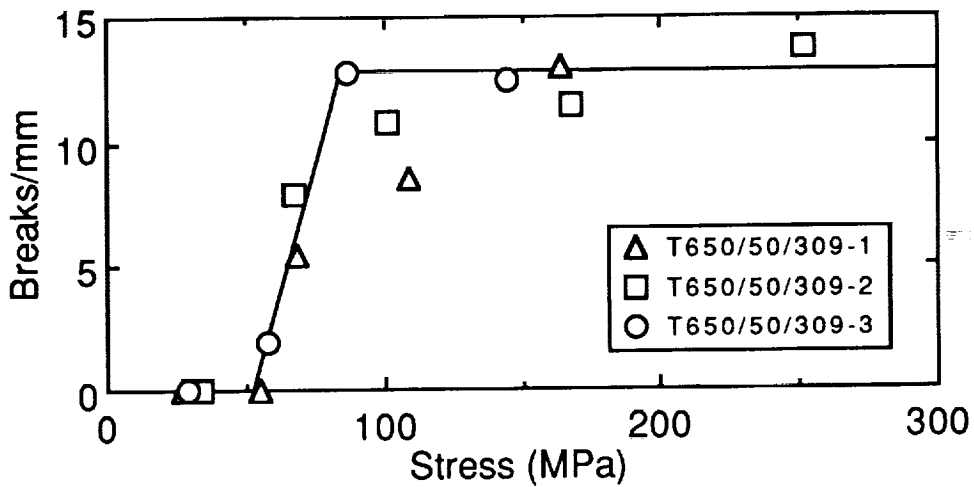


Figure 2.26: Microcompression behavior of Amoco T650/50 12K graphite fiber with 309 NT size in an intermediate modulus epoxy matrix.

The first step in interpreting the fiber crack density *vs.* applied stress curves is to examine the general shape of the curves and to look for similarities among them. All curves are roughly sigmoidal in shape and this shape becomes more definitive as more and more data points are represented. A similar trend has also been noted by Melanitis, *et al.* [18], in their work with carbon fiber/epoxy systems. We define three regions of the standard curve. The first region, Region I, which corresponds to very low (or zero) crack density and low to intermediate applied stress, can be considered the “critical flaw” region. In other words, cracks which occur in this region statistically correspond to fiber flaws or “weakest links.” These cracks are not truly representative of the fiber or of the interfacial strength. The second region, Region II, is defined by an increasing crack density with an increase in applied stress. The onset of this region and the rate of change varies from fiber to fiber and can potentially provide valuable insight into the affects of ultimate fiber strength and adhesion characteristics. This region may be correlated with the “ideal” adhesion curve described by a variational mechanics analysis [19]. In the third region, Region III, the crack density curve achieves a plateau and the fiber fragmentation can be considered complete. The Region III plateau density is the inverse of a critical fragment length.

We will neglect Region I, which is merely the start-up phase of the fragmentation process, and focus our attention on Regions II and III. As shown in Figs. 2.6–2.9, we choose to idealize Regions II and III using a bilinear fit.

The rising linear fit in Region II can be interpreted in terms of Weibull statistics. The Weibull cumulative distribution function can be derived from Poisson statistics. If a fiber of length L has $\Lambda(\sigma)$ flaws per unit length that have strengths less than or equal to σ , then, by Poisson statistics, the cumulative probability distribution function for failure of that fiber is

$$F(\sigma) = 1 - e^{-L\Lambda(\sigma)} \quad (2.1)$$

Comparing this to the cumulative Weibull distribution function for the same fiber

$$F(\sigma) = 1 - e^{-L\left(\frac{\sigma}{\sigma_0}\right)^m} \quad (2.2)$$

we see that the Weibull function makes the empirical assumption that the number of flaws per unit length is a power law in σ :

$$\Lambda(\sigma) = \left(\frac{\sigma}{\sigma_0}\right)^m \quad (2.3)$$

where m is the Weibull modulus and σ_0 is the scale parameter, or the load at which $1 - e^{-L}$ of the fibers have failed.

In Region II, the breaks/mm data can be viewed as a direct measurement of the flaw density, or of $\Lambda(\sigma)$. As the crack density increases, the existing flaws "shield" portions of the fiber from stress. The size of the shielded or exclusion zone depends on the ability of the interface to transfer the stress back into the broken fiber. When there are a significant number of flaws in the shielded zones, the observed crack density will differ from the true flaw density. Eventually the shielded zones dominate and no more cracks form. This situation corresponds to the plateau regions in Figs. 2.6–2.9. The earlier, linear portions of Figs. 2.6–2.9, however, correspond to the low crack density region which provides a direct measure of $\Lambda(\sigma)$. We therefore estimated m and σ_0 for the embedded fibers by fitting the Region II crack density data on a log plot using:

$$\log \Lambda(\sigma) = -m \log \sigma_0 + m \log \sigma \quad (2.4)$$

The results are summarized in Table 2.5. Except for IM7G, the Weibull modulus and scale parameters are reasonable for these fibers. A significant advantage of the analysis is that the Weibull parameters are determined from a *single* experiment on a *single* fiber. Conventional Weibull parameter estimation involves fracture tests on many fibers. A disadvantage of the *current* results is that they rely on the determination of breaks/mm at only a few strain levels. A more accurate analysis would require more experimental data in Region II

Table 2.5: Weibull parameters for Hercules graphite fibers

Fiber Type	σ_0 (MPa)	m
AS4	399	6.65
AS4G	432	9.41
IM7	401	5.57
IM7G	484	48.8

We can further interpret the Region II results by using the variational mechanics analysis in Ref. [19]. A variational mechanics analysis of the fragmentation process in a composite with a perfect interface predicts that the crack density should increase linearly with increasing stress [19]. We assume that the early parts of Region II correspond to conditions in which the interface is mostly intact and thus the observed linear increase is the one predicted by the variational mechanics analysis. The idealized fits in Figs. 2.6–2.9 for Region II are linear fits to all points judged to be within region II. Redoing the variational analysis in Ref. [19] reveals that the most significant parameter affecting the slope in Region II is the fiber strength. The higher the fiber strength, the steeper the slope in Region II.

Region III is the plateau region and is thus fit with a horizontal line at the saturation crack density. In most cases, these plateau values were determined from an average of density values where the rate of change had become negligible. However, in some cases it was unclear (due to insufficient data) whether or not fragmentation was complete. In these cases, the largest measured density was used to determine the plateau value.

To aid our interpretation of the Region II and Region III information, some typical fiber property data for the Hercules fibers used in this study are provided in Table 2.6. Similar data was not available for the Amoco fibers tested, however, it is known that relative strengths of these fibers

Table 2.6: Typical fiber property data for Hercules graphite fibers

Fiber Type	Diameter (μm)	Tensile Strength (MPa)	Ultimate Elongation (%)	Tensile Modulus (GPa)	Compression Strength (GPa)
AS4	6.96	4071	1.65	248	1723
IM7	5.00	5313	1.81	301	1862
HMS4	7.4	2484	0.70	345	N/A

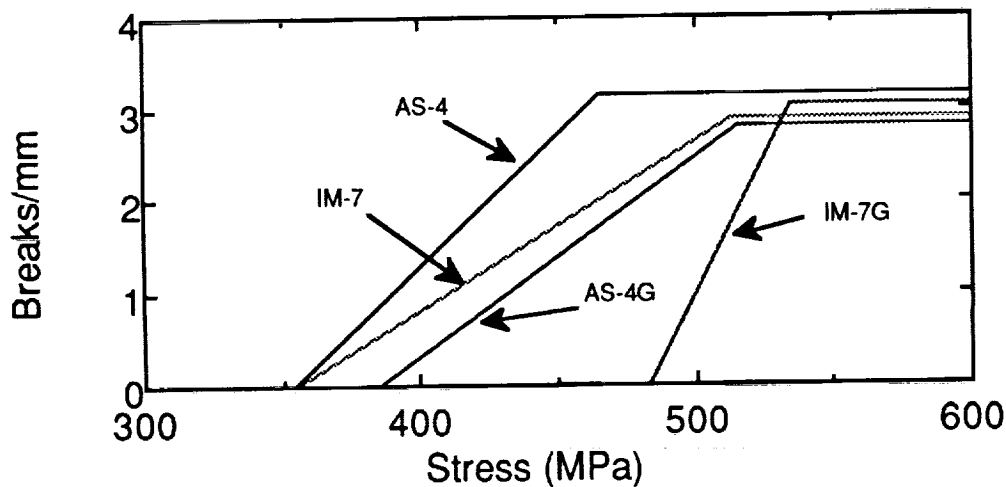


Figure 2.27: Microtensile behavior of Hercules graphite fibers.

are in descending order: T650/50 > T650/42 > T650/35 > T1000.

We begin with the microtensile behavior of the Hercules fibers. Table 2.7 summarizes the Region II and Region III information for these fibers and Figure 2.27 compares the idealized crack density vs. stress plots. The initiation load is the load at which the first fiber break appears, or the stress at the beginning of Region II. The initiation load depends on fiber type and sometimes on the presence or absence of sizing. The results are summarized as follows:

1. The application of "G" size to the AS4 fiber causes a modest increase in initiation load. There

Table 2.7: Microtensile behavior of Hercules graphite fibers. Summary of Region II and Region III information.

Fiber Type	Region II		Region II	
	Calculated Initiation Load (MPa)	Slope of Ideal Adhesion Curve (Breaks/mm/MPa)	Maximum Density (Breaks/mm)	Plateau Average (Breaks/mm)
AS4	354.8	0.028	3.19	3.15
AS4G	386.2	0.022	2.79	2.79
IM7	355.7	0.018	3.02	2.88
IM7G	483.5	0.059	3.02	3.02

is apparently a reduction in fiber flaws in the presence of sizing.

- The application of "G" size to the IM7 fiber causes a large increase in the initiation load. Sizing is thus even more effecting in reducing fiber flaws in IM7 fibers than in AS4 fibers.

Guided by the variational mechanics analysis in Ref. [19], the linear increase in crack density in Region II is assumed to reflect ideal behavior during which the fiber/matrix interface remains intact. The slope of Region II contains information about the fiber, matrix, and interface properties. For an ideal fiber with a single-valued strength, the slope is mostly controlled by the fiber strength [19]. This effect is evident when comparing IM7G to either AS4 or AS4G; the higher slope of Region II for the IM7G fibers agrees with the documented higher strength of those fibers.

The situation becomes confused, however, when we consider the IM7 fibers. The slope of the IM7 fibers in Region II is intermediate between the slopes for AS4 and AS4G, despite the fact that IM7's strength is higher. We suggest that the slope in Region II reflects more than just the fiber strength. For example, two fibers of identical strength but with different variances in strength

would have different slopes. The fiber with the more variable strength would have a lower slope; it would start cracking sooner, at the weak links that cause the strength variability, and finish cracking later. If we assume strength variability plays an important role we can conclude that:

1. Unsized IM7 fibers are more variable in strength than AS4 fibers.
2. Application of "G" sizing increases the strength variability of AS4 fibers, but decreases the strength variability of IM7.

The only information available from the crack density plateau, Region III, is the saturation crack density. This information is most commonly reported in reciprocal form as the critical fragment length. The results for tensile testing of AS4, AS4G, IM7, and IM7G were given in Table 2.2. Where a comparison is possible, our results are consistent with the work of other researchers [8-10,12-14].

Given the limited amount of tensile data obtained for the Amoco fibers, we were restricted to making only qualitative comparisons. The results presented in Table 2.3 suggest that the adhesion strengths of the T650/35 and T650/42 are comparable to that of Hercules AS4, whereas, the critical length of the T650/50X reflects a lower fiber tensile strength as compared to Hercules HMS4. It is difficult to classify the T1000 12K, UC-309 fiber, in part, because the fiber is manufactured from a different precursor than the other Amoco or Hercules fibers. Nevertheless, a relatively high proportion of long fragments in the fiber fragment distribution suggest low adhesion strength and/or low fiber strength.

The stress state in an embedded fiber in compression mode is very different than the stress state of the same fiber in tension. A major difference is the effect of Poisson's contraction. When a single embedded fiber is loaded in *tension*, the differential Poisson's contraction tends to promote *compressive* radial stress at the fiber/matrix interface. Conversely, a single fiber specimen loaded in *compression* is prone to radial *tensile* stresses at the fiber/matrix interface. This disparate behavior

at the interface between tensile and compressive stresses might be expected to have a significant effect on the interfacial failure properties and mechanisms. We turn again to the variational mechanics analysis for guidance in interpreting the results. The Region II and Region III information for all of the fibers tested in compression is summarized in Table 2.8.

Given the diversity of fiber types and fiber treatments (sizings or coatings) in the microcompression population, many quantitative comparisons can be made. Primarily this affords us an opportunity to examine:

1. the effects of fiber strength;
2. the effects of sizing;
3. the effects of release coating; and
4. the effects of precursor material.

In Figs. 2.28–2.31 fibers of varying strengths, but having equivalent surface treatments, are compared. Although the data are not entirely conclusive, the following dependencies are strongly suggested:

1. the failure initiation load increases with *decreasing* fiber strength;
2. the fiber fragmentation rate decreases with *decreasing* fiber strength; and
3. the crack density plateau value decreases with *decreasing* fiber strength.

The first observation is a direct contradiction of the microtensile behavior examined previously. This is not completely unexpected though because the stress state in the two situations is entirely different. Nevertheless, there are sufficient uncertainties within the data population to warrant more ambitious testing. The second observation is in accord with the variational mechanics predictions.

Table 2.8: Microcompression behavior of graphite fibers. Summary of Region II and Region III information

Fiber Type	Region II			Region III	
	Load at First Break (MPa)	Calculated Initiation Load (MPa)	Slope (Bks/mm/MPa)	Maximum Density (Bks/mm)	Plateau Average (Bks/mm)
AS4	13.92	101.2	0.13	6.28	5.50
AS4G (Group No. 1)	83.50	85.51	0.076	4.40	4.16
AS4G (Group No. 2)	105.8	89.11	0.063	3.66	3.22
AS4F	82.48	66.20	0.0078	1.52	1.02
IM7G	68.00	63.21	0.21	10.4	10.01
HMS4	26.79	25.68	0.20	11.5	10.63
T650/50X UC-309	57.82	52.59	0.39	13.7	12.7
T650/50X	55.60	78.38	1.08	10.6	9.64
T650/42 UC-309	68.60	67.20	0.47	9.80	9.35
T650/35 UC-309	42.17	81.87	0.36	8.05	7.20
T650/35	28.85	72.02	0.42	7.32	6.61
T1000 UC-309	59.56	86.29	0.21	3.98	3.26

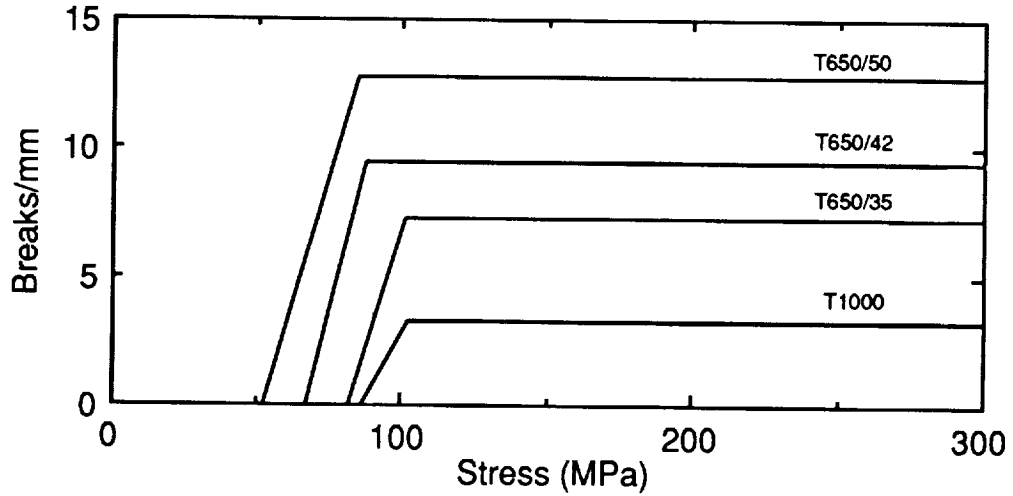


Figure 2.28: Effects of fiber strength on the microcompression behavior of Amoco graphite fibers treated with UC-309 size.

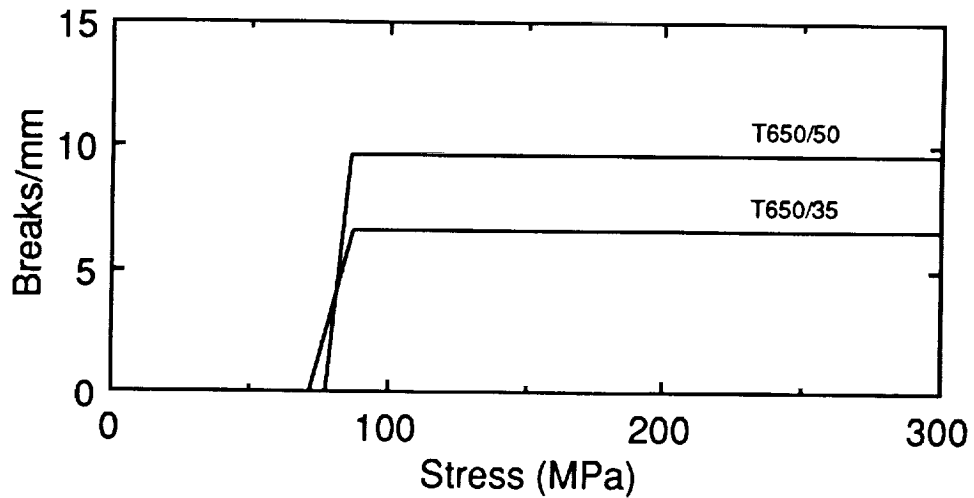


Figure 2.29: Effects of fiber strength on the microcompression behavior of unsized Amoco graphite fibers.

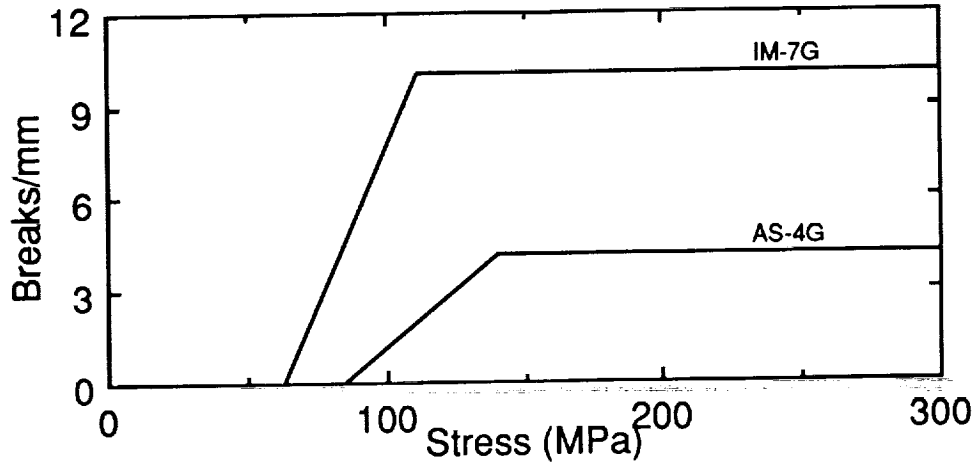


Figure 2.30: Effects of fiber strength on the microcompression behavior of Hercules graphite fibers treated with "G" size.

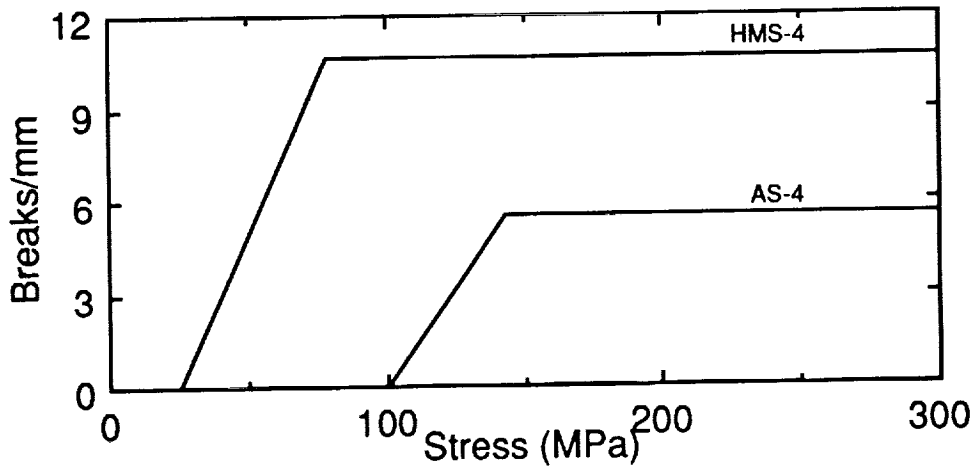


Figure 2.31: Effects of fiber strength on the microcompression behavior of (unsized) Hercules graphite fibers.

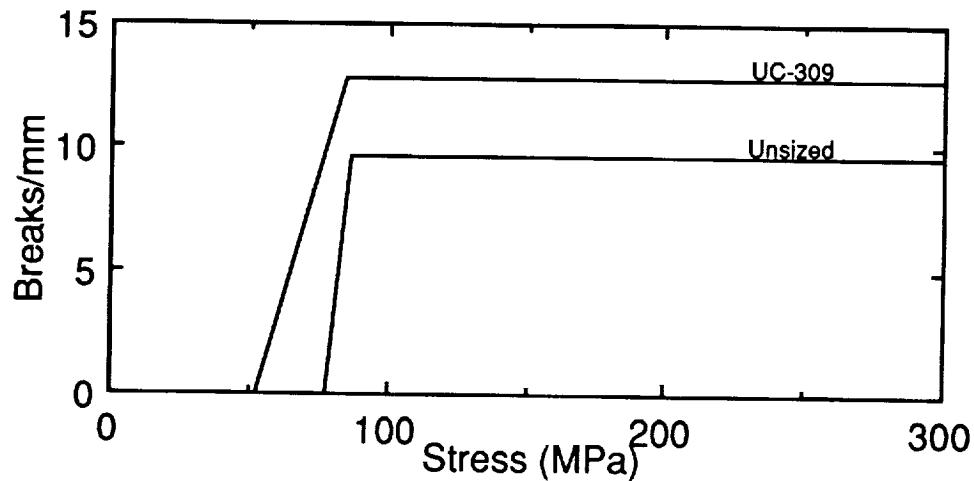


Figure 2.32: Effects of sizing on the microcompression behavior of Amoco T650/50K graphite fibers.

Figure 2.28 suggests that analogous with a decrease in fiber strength, a change in fiber precursor increases the failure initiation load, decreases the fragmentation rate, and decreases the crack density plateau value.

The effects of sizing are depicted in Figs. 2.32–2.34. The following dependencies are strongly suggested for the Amoco fibers with UC-309 size:

1. sizing decreases the fragmentation rate; and
2. sizing increases the crack density plateau value.

The effect of sizing on the failure initiation load is ambiguous for these fibers. The effects of “G” size on Hercules AS4 fibers are to decrease the fiber fragmentation rate, to decrease the crack density plateau value, and to decrease the failure initiation load (see Fig. 2.34). Given the lack of chemical information about UC-309 size (other than the fact that it is epoxy compatible) it was deemed inappropriate to combine the Hercules sized fibers and Amoco sized fibers in a single population.

Figure 2.34 bears closer examination to gain insight into the effects of the quality of adhesion

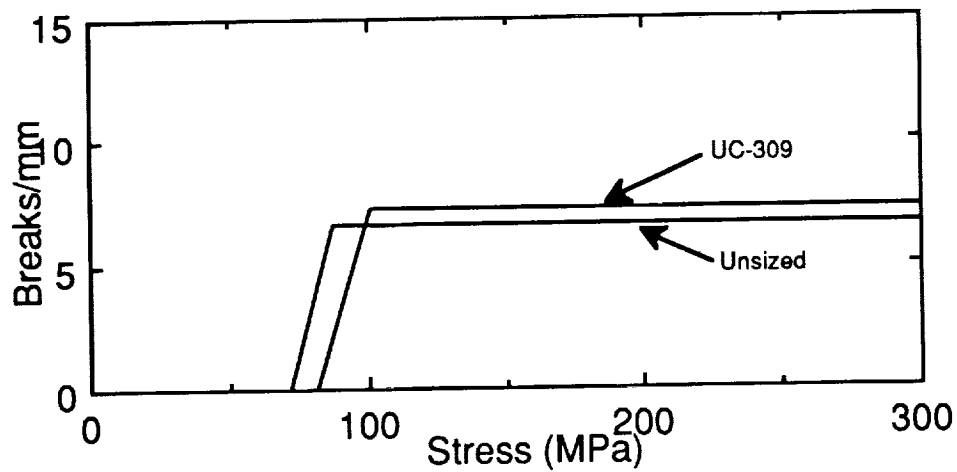


Figure 2.33: Effects of sizing on the microcompression behavior of Amoco T650/35K graphite fibers.

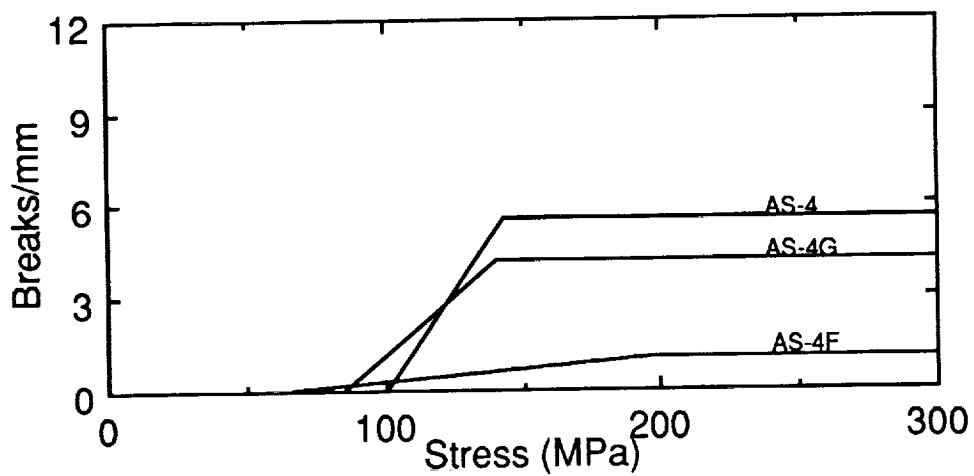


Figure 2.34: Effects of sizing and coating on the microcompression behavior of Hercules AS4 graphite fiber.

on the Region II and Region III parameters. We know from critical fragment length results that the Frekote 700 release coating on the Hercules fibers prevented good adhesion between the coated fiber and the matrix resin. With this fact established, the curves depicted in Fig. 2.34 suggest the following effects of release coating:

1. decreasing initiation load;
2. decreasing fragmentation rate (slope); and
3. decreasing crack density plateau value or weakening of adhesion.

The tensile results support these conclusions to the extent that the strength of the AS4 interface decreased in the presence of "G" size. Furthermore, it has been generally noted that the interfacial shear strength for a given fiber is inversely proportional to the critical fiber fragment length [13]. Thus, if the plateau values represented by these data are inversely proportional to the critical fiber fragment length, then they are directly proportional to the interfacial shear strength. This result, too, is consistent with the dramatic evidence provided by the AS4F fibers.

By examining the fiber fragment length distributions we can perhaps gain further into the combined effects of fiber strength and interfacial adhesion on the interfacial (shear) strength. Unfortunately, the data we have collected is very limited. Nevertheless, it is sufficient to allow us to obtain information about the shape(s) of the distribution and make some rudimentary comparisons with tensile results.

The bar charts depicted in Figs. 2.16–2.20 suggest the following:

1. the compression fiber fragment length distribution is roughly normal;
2. the width of the distribution gets narrower and the maximum frequency increases significantly as stress increases;

3. the maximum frequency of the distribution shifts to shorter fragment lengths with increasing stress; and
4. there is a small, but noticeable "tail" region in the distribution at longer fragment lengths that appears to be independent of stress.

Folkes and Wong [22], in their work with thermoplastic matrix composites in tension, have stated that "if a normal fibre fragment distribution histogram is obtained, the peak of the histogram should equal l_c ." If we compare the (compression) critical fragment length for IM7G with the average peak of the distributions obtained in Figs. 2.16–2.20, we see that in this case the Folkes and Wong prediction overestimates the critical fragment length by as much as 40%. Using the inverse of the critical plateau value to obtain the critical fragment length in compression, we find that the average peak of the distributions is slightly larger than the critical length. Given the distribution tail at higher fragment lengths, it is very probable that these distributions are skewed and a Gaussian representation is less than perfect.

In summary, we conclude that there is important information to be obtained from the manner in which a single embedded fiber approaches its critical crack density, or critical fragment length either in tension or compression. Furthermore, this behavior can be described by the Region II and Region III parameters defined here to permit quantitative comparisons of fiber and/or interfacial strengths. Caution must be exercised, though, in attempting to ascribe certain of these behaviors to fiber strength or fiber treatments alone. These two factors appear to interact by mechanisms which are poorly understood to produce a characteristic interfacial strength. In the final analysis, it is the interfacial strength which determines the ultimate microcomposite properties.

Chapter 3

Single-Ply Compression Tests

3.1 Introduction

Chapter 2 gives results of compression testing of single fibers embedded in a matrix. Chapter 4 gives results of compression testing of laminates. In an attempt to bridge the gap between single-fiber testing and laminate testing, we undertook a series of single-ply compression tests. This chapter begins by describing the development of a reliable single-ply compression test method. It then describes results of using that test method to study compression failure. Many of the single-ply specimens used the same batch of fibers used in single fiber tests in Chapter 2 and the same prepreg used in the laminates in Chapter 4.

3.2 Single-Ply Compression Test Method

To test single-ply composites in compression, we embedded mini-dog-bone specimens in about 20 mils of epoxy and uniaxially end loaded them while supported from the sides by guide blocks. End loading was done through shim stock with a thickness that matched each specimen's thickness. The sides of the guide blocks were coated with release agent to minimize friction effects. The dog-bone geometry and the test fixture are shown in Fig. 3.1.

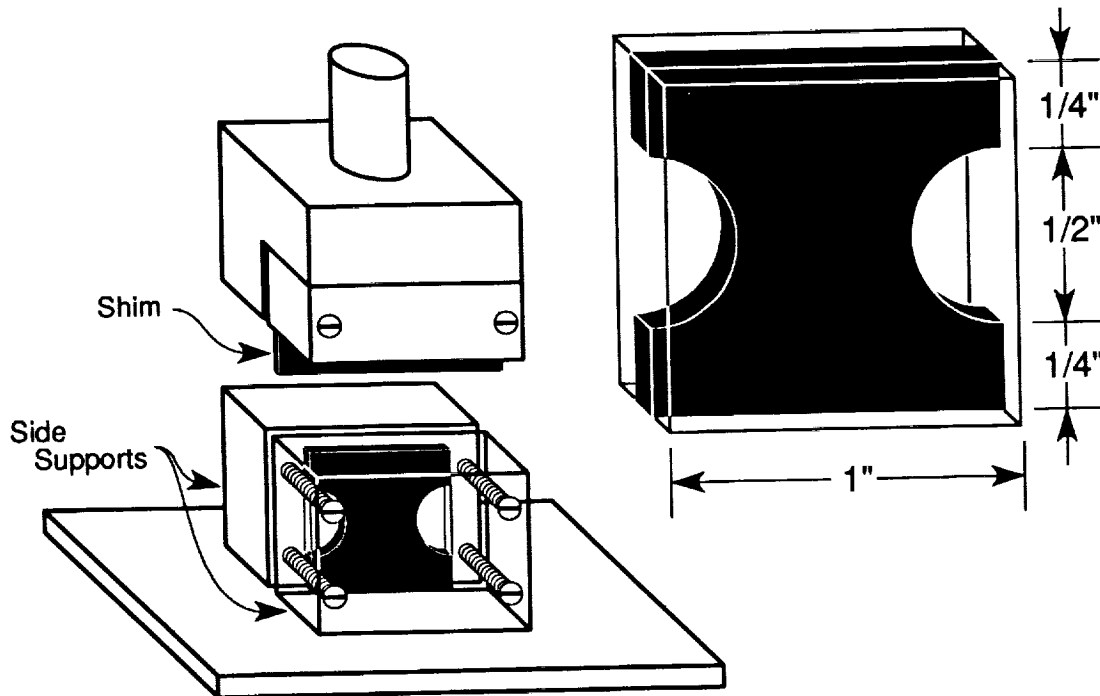


Figure 3.1: The single-ply composite compression test fixture and an enlargement of the embedded single-ply composite test specimen. The embedded single-ply composite specimens were positioned between two side supports. The rear side support was steel. A transparent, poly-methyl methacrylate front side support was used to permit observation of the failure process. Compression load was applied by a steel shim having a thickness matching that of the embedded single-ply composite specimen.

The composite compression strength was calculated from the failure load, P_{total} , by a simple rule-of-mixtures formula

$$\sigma_c = \frac{P_{total}E_c}{E_cA_c + E_eA_e} \quad (3.1)$$

where E_c and E_e are the moduli of the single-ply composite and of the embedding epoxy. A_c and A_e are the cross-sectional areas of the single-ply composite and of the embedding epoxy at the location of compression failure. Most specimens, and therefore those that were considered to be valid specimens, had compression failures at the midline of the specimen which corresponds to the location of minimum composite cross-sectional area. E_e was measured by compression tests on straight-sided specimens of pure epoxy. E_c was measured by compression tests on embedded single-ply composites in which the embedded composites had straight sides instead of the dog-bone shape in Fig. 3.1. These tests gave a specimen modulus; E_c was calculated by using a simple rule-of-mixtures analysis on the specimen modulus. The single-ply compression strengths in this chapter are results that were averaged from 15 to 20 nominally identical specimens.

The single-ply compression test seems to provide useful results. We next discuss some of the considerations that went into developing the test method:

1. The mini-dog-bone specimen geometry was used to reduce end effects. Compression tests on rectangular, single-ply composites always failed by end crushing.
2. The embedding epoxy was used to provide side support and hopefully to eliminate specimen buckling. Samples that were not embedded failed at low loads by global specimen buckling. To determine how much embedding epoxy was required, we measured the single-ply compression strength as a function of total specimen thickness. Figure 3.2 shows that σ_c , calculated by Eq. (3.1), increased up to about 20 mils of thickness, and then became constant. We concluded that when the embedding epoxy was too thin, specimens failed by global buckling, but that when the embedding epoxy was sufficiently thick, specimens failed by axial compressive failure

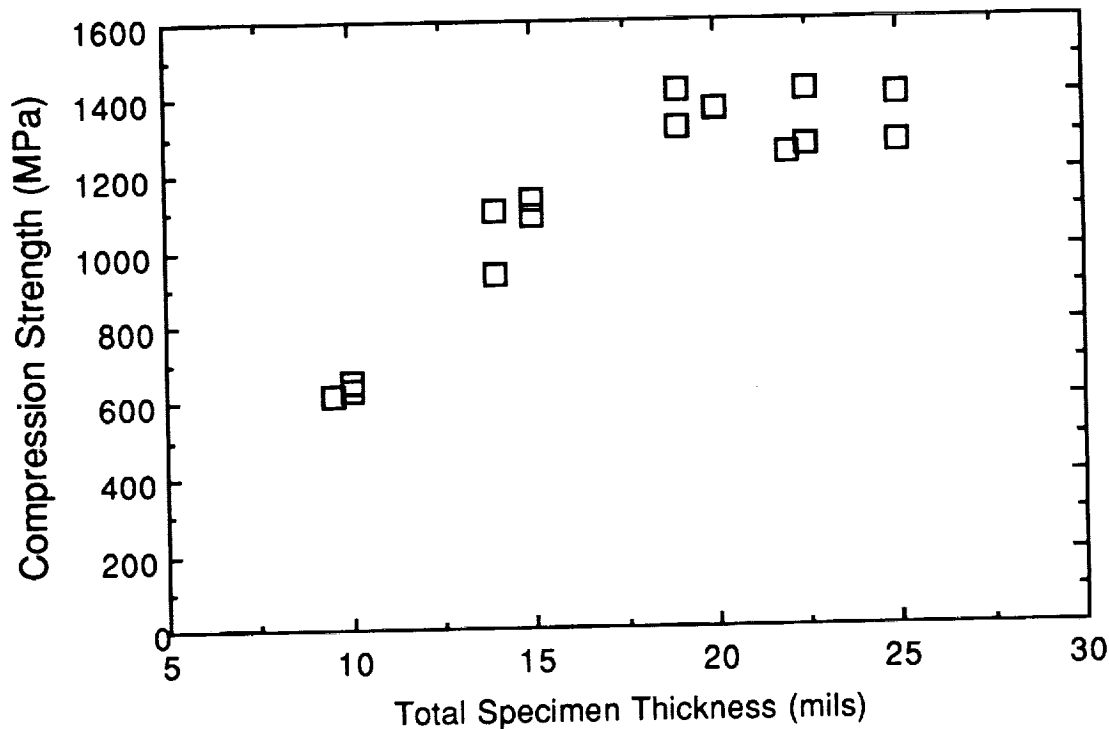


Figure 3.2: The compression strength of single-ply commercial Hercules AS4/3501-6 composites as a function of total specimen thickness

of the single-ply composite. These conclusions were supported by *in situ* observation of failure modes.

3. Any relatively stiff embedding epoxy can function to prevent buckling. The specimens in this chapter used Dow Chemical DER 332. This epoxy was cured with curing agent, Jeffamine D-230, and with Accelerator 399. Jeffamine D-230 and Accelerator 399 were purchased from Texaco Chemical Co.. We tried other embedding epoxies with different stiffnesses and found that as long as the epoxy is sufficiently stiff, the embedding epoxy does not affect the results [23].
4. Specimen alignment is critical to minimizing experimental scatter—the samples must be centered within the embedding epoxy. This centering was achieved by the following procedure. The embedded, single-ply composite specimens were made by curing the embedding epoxy in

a mold under pressure in a Carver Hot press. We waited until some initial cure had taken place before applying the pressure. If the pressure was applied too soon after the start of cure, the embedding epoxy viscosity was low and the pressure caused movement of the embedded single-ply composite resulting in poor centering. By waiting before applying pressure, however, the small amount of cure that takes place gave a higher viscosity embedding epoxy. With the higher viscosity embedding epoxy, there was much less movement of the embedded single-ply composite and specimens with good centering alignment could be obtained.

5. Another alignment problem is that the top and bottom of the mini-dog-bone specimen must be parallel. This was achieved by clamping the specimens in a steel jig and sanding their edges flush with the parallel edges of the jig.
6. The embedding epoxy had to be thoroughly degassed to avoid bubble formation during curing. When bubbles did form, they influenced the failure process. We often noted compression failures initiating near bubbles and at unusually low loads. Most results were obtained with bubble-free specimens. In some experiments we exploited the properties of bubbles. Unlike bubble-free samples, damage initiation in samples with bubbles became arrested after a small amount of damage growth. Damage arrest was probably due to the low loads for damage initiation in samples with bubbles. Because we could arrest damage in samples with bubbles, we used such samples to observe the early stages of compression damage.
7. We were somewhat concerned about premature failures caused by stress concentrations at the root of the cut-out in the mini-dog-bone specimens. Some crude three-dimensional, finite element calculations showed that the stress concentration factor at the root of the notch is between 2.5 and 3.5 but that the stress concentration zone is confined to a very small volume [23]. We suggest that the small stress concentration zone did not have a major influence on the

compression tests. Two experimental results support this suggestion. First, our measured compression strengths were within 20% to 30% of the compression strengths on straight-side laminates (see Chapter 4). If the stress concentration caused failure, we would have seen compression strengths 2.5 to 3.5 times lower than laminate results. Second, we loaded specimens in compression to 95% of their failure load and then followed this preload with tensile modulus measurements. If the stress concentration zone had significant fiber failure, we would have seen a reduction in tensile modulus. No such reduction was seen [23].

The compression experiments were done on a 25 kN Minnesota Testing Systems (MTS) 810 servohydraulic testing frame. All experiments were done under displacement control at cross-head speeds of about 0.001 mm/sec. Load and displacement information was collected on an IBM PC using custom developed software and an interface to an MTS 464 Data Display Device.

Besides measuring specimen strength and modulus, we observed compression failure modes in two ways. First, the front-support block was made of transparent poly-methyl methacrylate (see Fig. 3.1). We thus observed compression failures as they occurred. Second, following each single-ply composite compression test, the failed specimen was potted in the same embedding epoxy system (DER 332 + D-230 + AC 399) to preserve the state of the fracture damage. These potted specimens were cut at various locations and polished with 1 μm followed by 0.3 μm Al_2O_3 paste on a velvet cloth. The polished specimens were examined by optical microscopy.

3.3 Materials

We did single-ply tests on some of the same materials used for the single fiber tests in Chapter 2 and for the laminate tests in Chapter 4. These material systems were nine carbon fiber/epoxy resin composites (AS4/3501-6, AS4G/3501-6, IM7/3501-6, IM7G/3501-6, HMS4/3501-6, HMS4G/3501-6, AS4F/3501-6, IM7F/3501-6, HMS4F/3501-6). For some new materials, we added three carbon

fiber/thermoplastic resin composites (sized AS4/ULTEM, unsized AS4/ULTEM, and AS4/LARC-TPI-PAA+dopant). In the above notation, Hercules AS4, IM7, and HMS4 fibers are unsized carbon fibers. Hercules AS4G, IM7G, and HMS4G fibers are carbon fibers coated with an epoxy-compatible "G" sizing. Hercules AS4F, IM7F, and HMS4F fibers are carbon fibers treated with a release agent, Frekote 700. This coating significantly reduced the fiber/matrix interfacial strength (see Chapter 2). All 3501-6 resin matrix composite samples were obtained as B-staged prepreg tapes from Hercules. The prepreg was cured in an autoclave according to manufacturer's recommendations. The composites with thermoplastic matrices (ULTEM and LARC-TPI) were supplied by NASA Langley Research Center as single-ply composites.

3.4 Experimental Observations and Results

The experimental material systems were classified according to four variables. The first variable was fiber type for the same matrix system, such as AS4/3501-6, AS4G/3501-6, IM7/3501-6, IM7G/3501-6, HMS4/3501-6, and HMS4G/3501-6. The second variable was matrix type for the same fiber, such as AS4/3501-6, AS4/ULTEM, and AS4/LARC-TPI. The third variable was the presence or absence of applied fiber sizing, such as AS4/3501-6 and AS4G/3501-6 or sized AS4/3501-6 and unsized AS4/3501-6. The fourth variable was the presence or absence of release agent, Frekote 700, such as AS4/3501-6 and AS4F/3501-6. Table 3.1 lists the compression strengths of all single-ply composites tested. Table 3.1 also lists the critical fiber fragment lengths that resulted from single-fiber fragmentation tests (see Table 2.2 in Chapter 2 and Refs. [13], [16], and [20]) on single fibers embedded in an epoxy matrix. Qualitatively speaking, the interfacial shear strength for a given fiber is inversely proportional to the critical fiber fragment length [13, 16]. The samples showing infinite critical length resulted from single-fiber fragmentation tests in which the fiber could not be fragmented during tensile loading. These materials have essentially zero interfacial strength.

Table 3.1: The single-ply compression strengths and critical length results for various composite materials. The critical length results were measured by single-fiber fragmentation tests. A critical length of ∞ means that the fiber was not fragmented during the test and that the interfacial strength was effectively zero.

Material System	Compression Strength (GPa)	Critical Length (mm)	V_f (%)
AS4/3501-6	1.48	0.313	62
IM7/3501-6	1.37	0.332	62
HMS4/3501-6	0.73	0.709	62
AS4G/3501-6	1.47	0.358	62
IM7G/3501-6	1.38	0.332	62
HMS4G/3501-6	0.75	-	62
AS4F/3501-6	0.643	∞	62
IM7F/3501-6	0.629	∞	62
HMS4F/3501-6	0.695	∞	62
AS4/ULTEM sized	1.18	-	61
AS4/ULTEM unsized	1.09	-	56
AS4/LARC-TPI	1.24	-	-

For composites with the same matrix, but with different fibers, the low- and intermediate-modulus fibers, AS4 and IM7, gave high compression strengths of about 1.4 GPa. These compression strengths are similar to the compression strengths of multiply AS4/3501-6 laminates [24, 25] (see also Chapter 4). The similarity supports our claim that the single-ply composite compression test measures a true in-plane compression strength. The high modulus fiber, HMS4, had a much lower compression strength of about 0.74 GPa. The lower result for HMS4 composites may be due to the fiber being weaker in compression or to other effects unrelated to fiber strength. Some results discussed below suggest that the low compression strength of HMS4 composites was a consequence of the poor fiber/matrix interface in those composites.

The matrix also influenced compression strength. The most complete results were for AS4 fibers in 3501-6 epoxy, ULTEM, or LARC-TPI matrices. The epoxy matrix had the highest compression strength of 1.48 GPa. The two thermoplastic matrices, LARC-TPI and ULTEM, had lower compression strengths of 1.24 GPa and 1.18 GPa, respectively. In agreement with Rosen's buckling model [1], the compression strengths rank in the same order as the matrix modulus. The moduli for 3501-6, LARC-TPI, and ULTEM are 3.8 GPa, 3.5 GPa, and 3.0 GPa, respectively [26].

The presence or absence of fiber sizing had little or no effect on composite compression strength. The lack of a sizing effect was observed for AS4, IM7, and HMS4 fibers in a 3501-6 epoxy matrix where the fibers were coated or not coated with an epoxy compatible "G" sizing. A small effect was seen for sized and unsized AS4 fibers in an ULTEM matrix. The sized AS4/ULTEM had a compression strength of 1.18 GPa as compared to 1.09 GPa for unsized AS4/ULTEM composites. The sized AS4/ULTEM composites, however, had a higher volume fraction than the unsized AS4/ULTEM composites. The differences in compression strength may be due to the different fiber volume fractions and not to the fiber sizing.

The presence of release agent, Frekote 700, had a dramatic effect on compression strength. The

AS4F/3501-6, IM7F/3501-6 and HMS4F/3501-6 composites all had compression strengths lower than 0.70 GPa. These were the lowest compression strengths of all samples tested.

To consider the effect of interface on composite compression strength, we plotted the compression strength as a function of the reciprocal of the critical length. As discussed above, the critical length is inversely proportional to the interfacial strength and thus a plot of compression strength *vs.* the reciprocal of the critical length is a plot proportional to the interfacial strength. Such a plot, given in Fig. 3.3, suggests a correlation between composite compression strength and interfacial strength. At low interfacial strength the composite compression strength was also low. All samples having the fibers coated with the release agent (AS4F, IM7F, and HMS4F) had essentially zero interfacial strength ($l_c = \infty$) and a composite compression strength below 0.70 GPa. The HMS4 and HMS4G composites had a better, albeit still poor, interface and compression strengths of 0.74 GPa that were only marginally better than the composites with zero interfacial strength. The AS4 and IM7 composites had the highest interfacial strength and the highest composite compression strength. A conclusion consistent with these results is that there is some minimum critical interfacial strength. If the interfacial strength is below the critical minimum then the composite compression strength will be some low and relatively constant value. If the interfacial strength is high, the compression strength can also be high. The absolute value of the high compression strength will depend on the matrix type and probably on the fiber type. The compression strength cannot increase indefinitely with increases in interfacial strength and thus the curve we sketch in Fig. 3.3 levels off at high interfacial strength. The specific plateau compression strength sketched in Fig. 3.3 assumes it to be similar to the highest compression strengths we measured. This choice was not based on tests with composites having higher interfacial strengths. If we accept the above conclusions, we can further conclude that the poor compression properties of HMS4 composites were due to a poor fiber/matrix interface and not to an inherent weakness of HMS4 fibers in

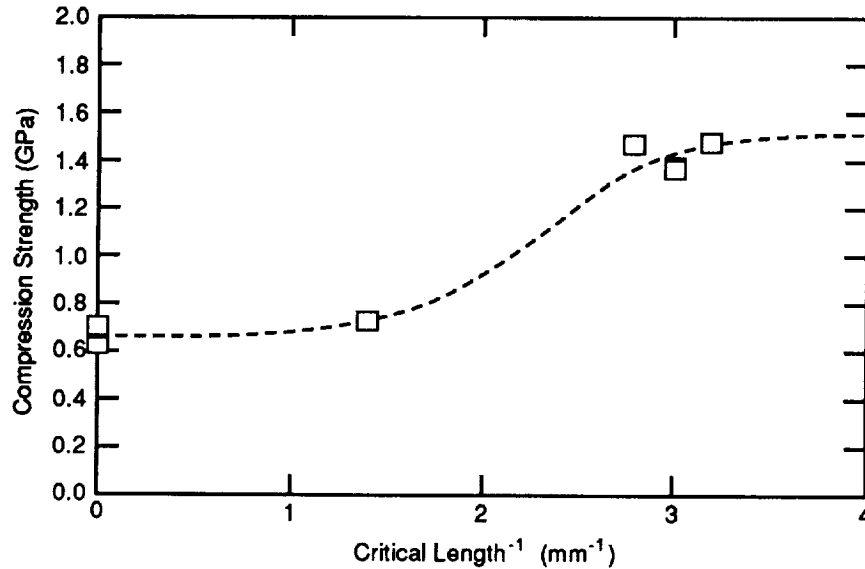


Figure 3.3: Single-ply composite compression strength as a function of the reciprocal of the critical length. The reciprocal of the critical length is proportional to the interfacial strength.

compression.

An advantage of the single-ply composite compression test is that we can observe compression failure take place. Most specimens fractured at or near the center of the dog-bone shaped specimen. Some fractures occurred suddenly and without warning, while others occurred slowly and could be observed to propagate across the width of the specimen. In all cases, we stopped the tests as soon as possible after observing failures and then further examined the failed specimens with optical microscopy. The quality of the fractured structure depended on how promptly the test was halted after observing the fracture. In some cases it was not possible to stop the test fast enough to be able to describe the failure process unambiguously.

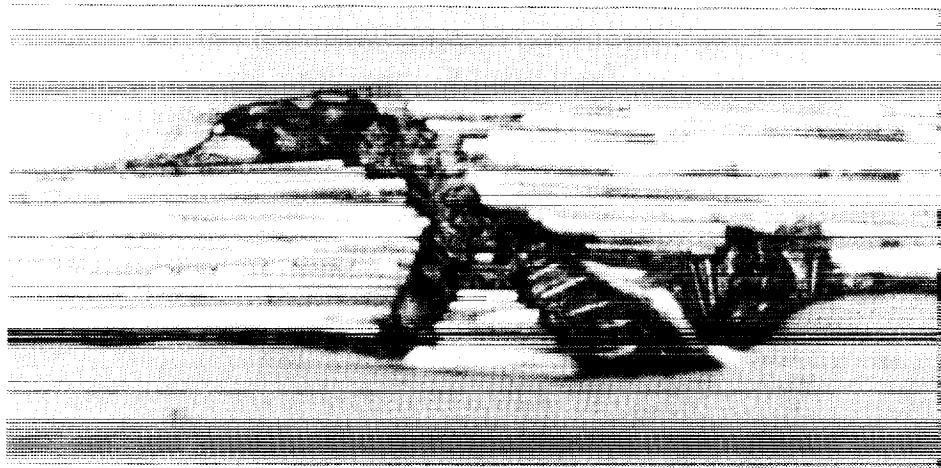
Compression failures of AS4/3501-6, IM7/3501-6, and AS4/LARC-TPI specimens were characterized by instantaneous and catastrophic failure accompanied by an audible acoustic event. This type of failure was universally observed for defect-free specimens; that is, for well-prepared and well-machined specimens. Typical fractures for these materials are shown in Fig. 3.4. These fractures can all be described by the same failure mechanisms. The failures occurred by kink banding

followed by longitudinal propagation of the compression damage parallel to the fibers and by out-of-plane slip along the kink band line. Longitudinal damage propagation results in multiple kink bands in the damage zone (see Fig. 3.4A). Out-of-plane slip along the kink band line is clearly shown in Fig. 3.4C. Because the test could not be stopped soon enough after failure, it was usually not possible to capture the details of kink bands or of the structure of the longitudinally propagated damage. We suggest that the catastrophic nature of the failure caused some or all of the fractured fibers within the kink bands to be removed during potting and polishing of the specimens.

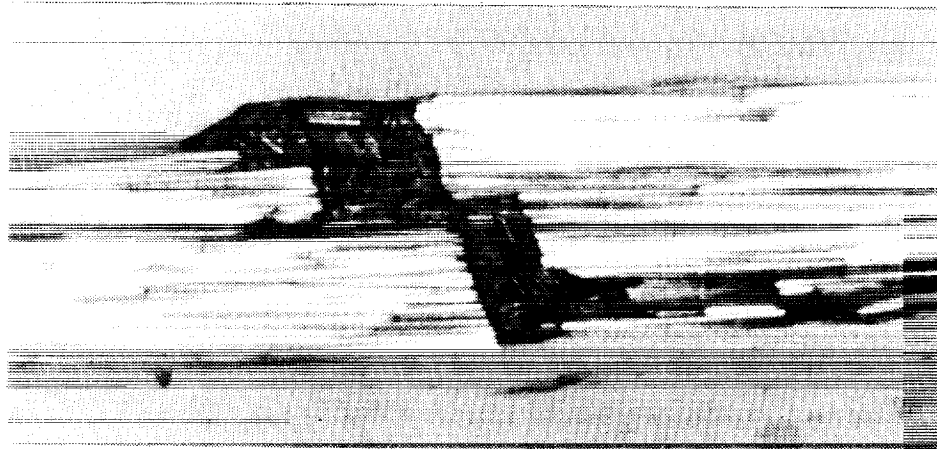
Because of the high compression strength of AS4/3501-6 and IM7/3501-6 composites and because the AS4 and IM7 fibers have low or intermediate modulus, these specimens were able to withstand the most compressive strain before failure. These material systems, therefore, accumulate high levels of strain energy. At failure, the rapid release of strain energy resulted in instantaneous, catastrophic, and audible failure by kink banding and out-of-plane slip. By microbuckling models, the fibers will be curved prior to failure. The kink band will start at the point of maximum curvature and proceed in a direction determined by the maximum shear force. The out-of-plane slip will also be along the kink band boundary or maximum shear direction. The amount of out-of-plane slip that is observed will be related to the amount of strain energy released at failure.

Although the failure mechanisms of AS4/3501-6, IM7/3501-6, and AS4/LARC-TPI were similar, the amount of longitudinal propagation of damage in these materials was different. The longitudinal damage propagation area depended on the modulus of the fiber and on the matrix. The longitudinal damage propagation area in AS4/3501-6 was typically longer than that of IM7/3501-6 (compare Fig. 3.4A to Fig. 3.4B). Likewise, the longitudinal damage propagation area in AS4/3501-6 was typically longer than that of AS4/LARC-TPI (compare Fig. 3.4A to Fig. 3.4C). These differences can be related to the amount of strain energy present at the time of failure. Comparing AS4/3501-6 to IM7/3501-6, both specimens had the same compression strength and thus the lower-

A. AS4/3501-6 composites



B. IM7/3501-6 composites



C. AS4/LARC-TPI composites

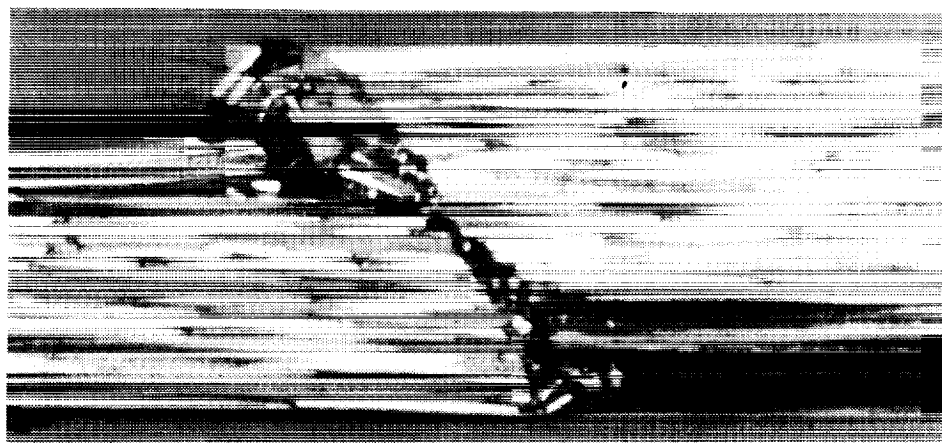


Figure 3.4: Typical cross sections of compression damage. The cross head speed was 0.001 mm/sec. The magnification is 200X.

modulus AS4/3501-6 composites had higher strain energy at failure. Comparing AS4/3501-6 and AS4/LARC-TPI, both specimens had the same modulus and thus the higher strength AS4/3501-6 composites had higher strain energy at failure. Therefore, the higher the strain energy at failure, the more extensive was the longitudinal damage propagation area. To be more precise about the longitudinal propagation of damage it would be desirable to observe earlier stages of damage. Although the cross head speed was decreased from 0.001 mm/sec to 0.0001 mm/sec for AS4/3501-6 and IM7/3501-6, it was not possible to observe the initiation and longitudinal propagation of compression damage. Fortunately, the results from some specimens described later were less instantaneous and less catastrophic. Such specimens allowed us to better study the early stages of compression damage.

The failure modes of AS4G/3501-6 and IM7G/3501-6 were similar to those of AS4/3501-6 and IM7 3501-6. The "G" sizing on the fiber thus had no effect on the compression strength as well as no effect of the failure modes of these composites.

The fracture phenomena of sized and unsized AS4/ULTEM composites were characterized by compression damage that rapidly propagated perpendicular to the fiber direction and across the mid-line of the dog-bone. We characterize rapid propagation as damage propagation taking about 0.5 sec to cross the sample width. The rapidly propagating failure of AS4/ULTEM composites was thus less catastrophic than the instantaneous damage observed in AS4/3501-6, IM7/3501-6 and AS4/LARC-TPI composites. The results for AS4/ULTEM composites were not affected by the presence or absence of fiber sizing. Fig. 3.5A. shows a fracture that is typical of both sized AS4/ULTEM and unsized AS4/ULTEM composites. As in AS4/3501-6 composites, the failure occurred by kink banding, out-of-plane slip, and longitudinal propagation of damage. Due to the less catastrophic nature of the failure event and our ability to stop the test sooner, the amount of slip and longitudinal damage propagation was typically less in AS4/ULTEM composites than it

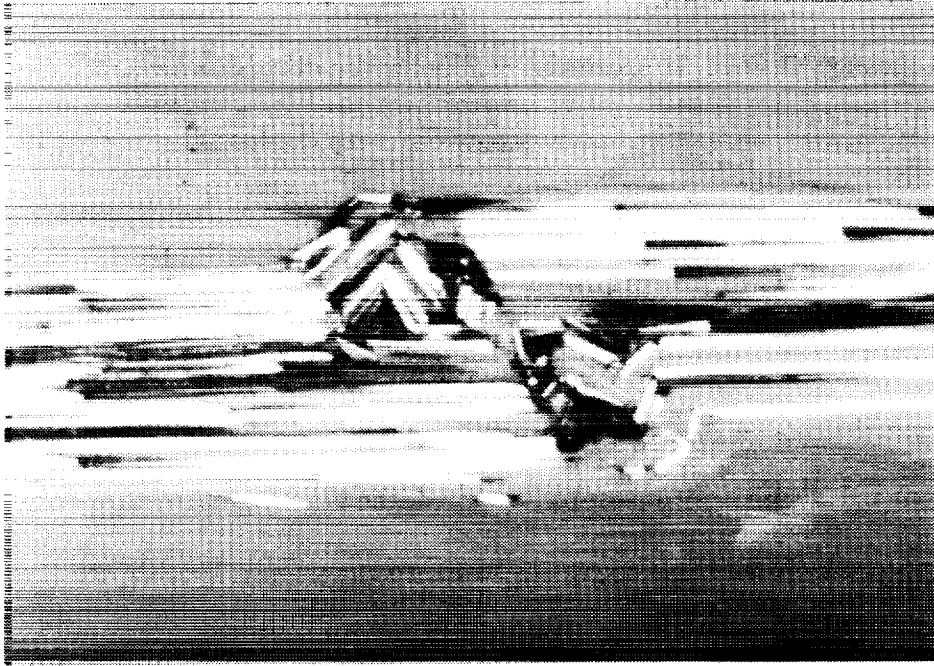
was in AS4/3501-6, IM7-3501-6, and AS4/LARC-TPI.

Some results from composites that contained pre-existing defects helped us observe the earliest stages of compression damage. In specimens containing pre-existing defects, the damage propagation was less rapid, typically taking 1 to 10 seconds to cross the specimen width. These specimens thus gave us an opportunity to stop the test during the compression failure process. By sectioning near the damage zone tip or just behind it, we observed early forms of compression damage. A typical result for an AS4/ULTEM composite having defects is shown in Fig. 3.5B. It shows a clear kink band and a longitudinal split. The kink band is just beginning longitudinal propagation into a second kink band. Because less damage had occurred, the fibers remained in the kink band during the polishing process. From these specimens alone we cannot say whether the kink band or the longitudinal split was the first form of damage or whether these events occurred simultaneously.

Like defective AS4/ULTEM specimens, *defect-free* HMS4/3501-6 and HMS4G/3501-6 failed by slow damage propagation typically taking 2 to 10 seconds to cross the specimen width. Figure 3.6A shows a typical compression damage zone. There is a clear kink band with intact fibers, some longitudinal splitting, and evidence of the initiation of longitudinal propagation of kink banding damage. There is little or no out-of-plane slip along the kink band. We associate the lower amount of out-of-plane slip with the much smaller amount of strain energy released and with our ability to stop the test sooner after failure. The HMS4 laminates failed at a lower load and had a higher modulus. Both of these factors contributed to a lower sample strain energy at the time of failure.

Figure 3.6B shows the compression damage at the tip of the compression damage zone from a test that was stopped while the compression damage was propagating across the specimen width. There is a clear longitudinal split, but only a *partial* kink band. The implication is that the longitudinal split occurred first and that it initiated the kink band. The kink band then propagated from the longitudinal split and across the thickness of the specimen. Despite careful efforts, however,

A. A defect-free sized AS4/ULTEM composite



B. A sized AS4/ULTEM composite having a minor defect

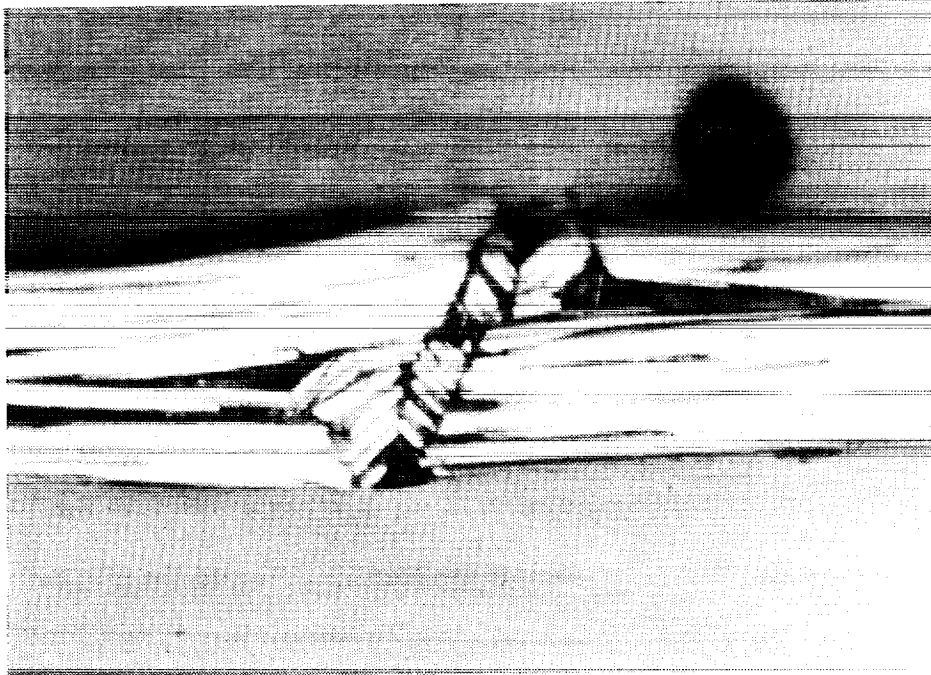
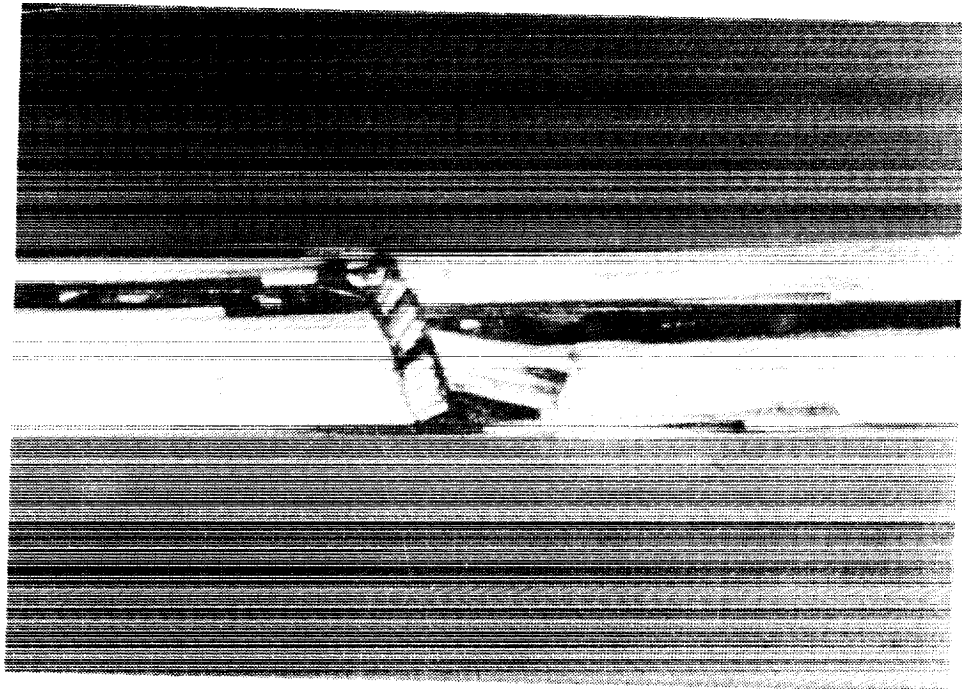


Figure 3.5: Typical cross sections of compression damage. The cross head speed was 0.001 mm/sec. The magnification is 200X.

A. HMS4/3501-6 composites



B. HMS4/3501-6 composites sectioned near the top of the damage zone

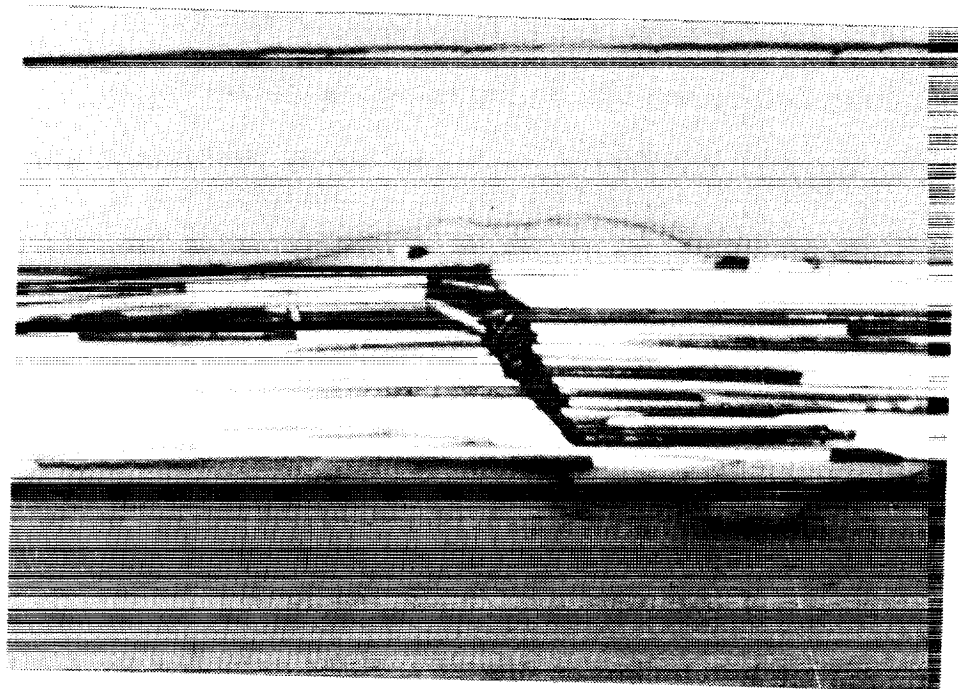


Figure 3.6: Typical cross sections of compression damage. The cross head speed was 0.001 mm/sec. The magnification is 200X.

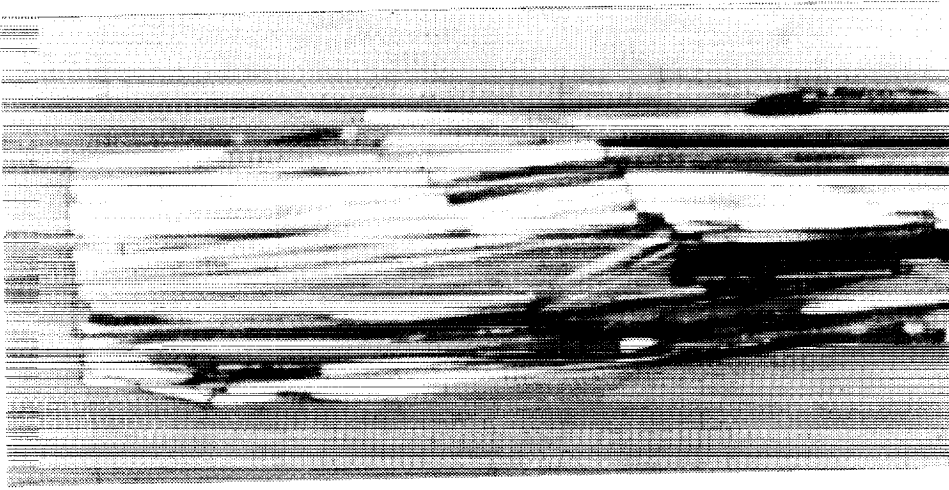


Figure 3.7: Typical cross sections of compression damage in composites having the fibers treated with release agent Frekote 700. The cross head speed was 0.001 mm/sec. The magnification is 200X.

we were unable to temporally resolve longitudinal split initiation and kink band initiation on the experimental stress-strain curves. It is possible that both failure processes occurred simultaneously. Earlier, we concluded that the low compression strength of HMS4 composites was due to the poor fiber/matrix interface. It is possible that the poor interface promotes longitudinal splitting. The longitudinal splitting then initiates kink banding followed by specimen failure.

Figure 3.7 shows typical fracture features of AS4F/3501-6, IM7F/3501-6, and HMS4F/3501-6 specimens. These specimens had essentially zero interfacial strength and failed by longitudinal splitting initiating at the sample ends. At later stages of damage the longitudinal splits caused kink bands. The kink band lengths (δ in Fig. 3.8) in composites with zero interfacial strength were always much longer than those of composites with a stronger interface (see Fig. 3.7). The observation of kink bands being caused by longitudinal splits in these composites with zero interfacial strength and the parallel observation of longitudinal splits causing kink bands in HMS4 composites reinforces the suggestion that the low compression strength of HMS4 composites was a result of its poor fiber/matrix interface.

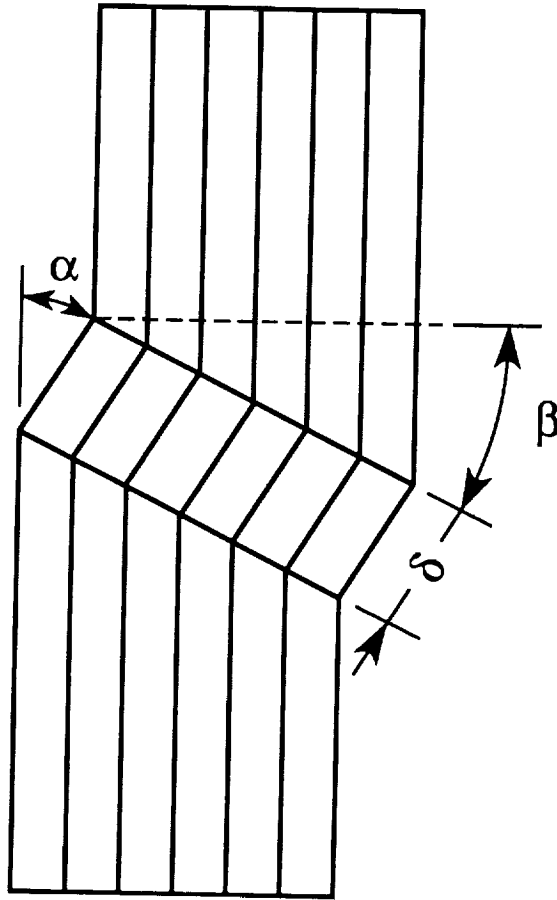


Figure 3.8: A schematic drawing of a kink band in a composite that fails under compression. The three parameters characterizing a kink band are the kink band orientation angle (α), the kink band angle (β), and the kink band length (δ).

3.5 Conclusions

Individual tests of samples where only the fiber or the matrix change show that both the fiber and the matrix can affect compression strength. The AS4 and IM7 carbon fiber composites have a much higher compression strength than the HMS4 carbon fiber composites. The higher-modulus 3501-6 epoxy matrix composites have a higher compression strength than the two lower-modulus thermoplastic matrix composites.

Because changing the fiber or the matrix also affects the interfacial strength, it is not possible to separate fiber and matrix effects from interfacial strength effects. A plot of all our results as a function of interfacial strength suggests that interfacial strength is crucial to determining the compression strength. More experiments are required to find out under what conditions interfacial strength is important and under what conditions other strength-limiting mechanisms, such as fiber failure, become active (see Chapter 5).

In composites with low compression strengths, such as HMS4 carbon fiber composites or composites with fibers treated with Frekote 700 release agent, it was possible to observe the earliest stages of compression damage. The results show that longitudinal splitting starts first and that kink bands initiate from the longitudinal splits and propagate across the specimen thickness. At later stages of compression damage the kink banding damage propagates longitudinally resulting in the formation of multiple kink bands. Some samples failed too rapidly to allow observation of the earliest stages of compression damage. Although we have no direct evidence, we hypothesize that these samples also initiate compression failure by longitudinal splitting followed by kink banding. It is possible, however, that samples with high interfacial strength will not show longitudinal splitting. The first form of damage in such specimens would instead be kink banding.

Chapter 4

Laminate Compression Strength

4.1 Introduction

Chapter 2 gives results of compression testing of single fibers embedded in a matrix. Chapter 3 gives results of compression testing of single plies. This chapter describes work completed as a subcontract to Hercules, Inc. (associate investigator was David J. Boll), to measure the compression properties of laminates. All fibers used to make the laminates were from the same batch of fibers used in the single-fiber tests (Chapter 2) and in the single-ply tests (Chapter 3). The prepreg material used to make the laminates was from the same batch of prepreg used to make the single-ply specimens in Chapter 3. This chapter thus completes the discussion of an extensive program on compression failure ranging from the most basic specimens (single-fiber specimens) to realistic structures (laminate specimens)

4.2 Materials and Methods

The material systems used included six carbon fiber/epoxy resin composites (AS4/3501-6, AS4G/3501-6, IM7/3501-6, IM7G/3501-6, HMS4/3501-6, HMS4G/3501-6, AS4F/3501-6, IM7F/3501-6, and HMS4F/3501-6). The Hercules AS4, IM7, and HMS4 fibers were unsized carbon fibers. The Hercules AS4G, IM7G, and HMS4G fibers were carbon fibers coated with an epoxy compatible

"G" sizing. The Hercules AS4F, IM7F, and HMS4F fibers were carbon fibers treated with a release agent—Frekote 700. This coating significantly reduced the fiber/matrix interfacial strength (see Chapter 2). The prepreg material for each laminate type was manufactured by Hercules in single batches. Enough prepreg material was made to supply both the single-ply tests (Chapter 3) and the laminate tests. The laminates were cured in an autoclave by Hercules, Inc..

Compression strength measurements were done using a modified ASTM D695 procedure. In brief, specimens that were $3.180 \pm .005$ inches long by $0.500 \pm .005$ inches wide and about 0.040 inches thick (7 or 8 plies) were end tabbed with graphite/epoxy end tabs. The end tabs extended to near the center leaving a gage section of $0.188 \pm .005$ inches. These specimens were end loaded, while side supported, until failure. To prevent end crushing, the ASTM D695 procedure was modified by incorporating a metal end cap.

Compression modulus measurements were done with the same type of specimens except that no end tabs were used. The samples were end-loaded in the same fixture. Axial compression strain was measured using an axial strain gage in the center of the sample.

4.3 Results

Axial (0°) compression tests were done on all materials. The compression strength results for dry specimens are given in column 2 of Table 4.1. Each section of the table includes all fiber types for a single type of fiber treatment. We begin with the unsized fibers in the first section of the table; these are the baseline results. The compression strengths for AS4 and IM7 laminates were similar while the compression strength for HMS4 laminates was about 50% lower. Adding the "G" sizing had no significant effect on the compression strengths. In contrast, the release coating in the "F" series laminates had a large effect. The poor interface in the "F" series laminates caused them all to have low compression strengths.

Table 4.1: Axial (0°) compression strengths of various fibers in a Hercules 3501-6 epoxy matrix. Results are given for both dry and wet conditions. The numbers in parentheses after the wet results are the percent retention of the dry results. Where given, numbers following \pm are the standard deviation of the results

Fiber Type	Dry		Wet	
	Strength (GPa)	Modulus (GPa)	Strength (GPa)	Modulus (GPa)
AS4	1.97 \pm .149	136	1.71 (87%)	132 (97%)
IM7	2.05 \pm .095	160	1.70 (83%)	153 (96%)
HMS4	1.03 \pm .058	193	0.87 (84%)	188 (97%)
AS4G	1.92 \pm .108	128	1.75 (91%)	126 (98%)
IM7G	2.08 \pm .103	164	1.77 (85%)	137 (84%)
HMS4G	1.00 \pm .038	203	0.85 (85%)	190 (94%)
AS4F	0.72 \pm .08	122	0.55 (76%)	118 (97%)
IM7F	0.87 \pm .10	195	0.70 (80%)	160 (82%)
HMS4F	0.79 \pm .08	239	0.67 (85%)	170 (71%)

The compression modulus results for dry specimens are given in column 3 of Table 4.1. The compression modulus results all rank as expected—the compression modulus increases as the modulus of the fiber increases. There were no clear trends in the modulus due to fiber treatments. Versus the unsized fibers, the “G” sized fibers had the same modulus. For the “F” series fibers, the AS4F laminates had a decreased modulus while the IM7F and HMS4F laminates had increased moduli.

Wet specimens were prepared by soaking to saturation in distilled water. The average weight gain was 1.14%. The compression strength and compression modulus for wet specimens are given in columns 4 and 5 of Table 4.1. The compression strength retentions ranged from 76% to 91% with an average of $84.0 \pm 4.2\%$. Except for three laminates, the compression modulus retentions were all over 94% and thus somewhat higher than the compression strength retentions. The average modulus retention was $90.7 \pm 9.5\%$.

4.4 Discussion and Conclusions

The “G” sizing had no discernible effect on the compression strength or the compression modulus. The release coating in the “F” series laminates, however, had a large effect on compression strength.

Clearly, a reduction in the fiber-matrix adhesion significantly reduces axial (0°) compression strength. The facts that the compression strengths of the HMS4 and HMS4G laminates were significantly lower than compression strengths of the AS4, AS4G, IM7, and IM7G laminates, and that applying a release coating to the HMS4 fibers had less of an effect than applying it to the AS4 or IM7 laminates, suggest that the adhesion between HMS4 fibers and 3501-6 matrix is inherently low. This conclusion is supported by adhesion measurements using single-fiber fragmentation tests [9, 14] and by short beam shear tests [27](see also Chapter 2). The low adhesion of HMS4 has been attributed to a cohesively weak skin of highly oriented graphite basal planes that have a low

resistance to interfacial shear stresses. Application of the release coating to HMS4 fibers reduces adhesion even further (as suggested by the small decrease in compression strength). It probably also shifts the interfacial failure from the fiber skin to the fiber-matrix interface. If no such shift took place, the compression strength would have been unaffected by the release coating.

The conclusions drawn from the laminate tests are very similar to the conclusions drawn from the single-ply tests in Chapter 3. This similarity supports the utility of the single-ply test method. It can give useful results with a very minimal amount of material. The absolute compression strengths measured by the laminate tests are 20% to 30% higher than the compression strengths measured by the single-ply tests. When the goal is to measure the most accurate compression strength, the laminate tests are preferred. When the goal is to discover trends and to develop understanding about compression failure, the single-ply test has much potential.



Chapter 5

Interface and Its Effect on Compression Strength

5.1 Introduction

There are at least two important factors that can influence the fiber/matrix interface in thermoplastic matrix composites; neither factor has a significant effect on the interface in thermoset matrix composites. The first is matrix crystallinity. Fibers can act as nucleating agents and promote transcrystalline regions in an interphase region between the fiber and the bulk matrix [28–36]. Transcrystallinity will almost certainly influence the mechanical properties of the interface (albeit not necessarily for the better [30]). In the absence of transcrystallinity, or even in conjunction with transcrystallinity, the second factor is adsorption of the polymer matrix onto the fiber. Adsorption is probably a prerequisite for achieving good fiber/matrix adhesion and even for achieving transcrystallinity [6]. Because the molecular weight of thermoplastic matrices is much higher than that of monomers in thermosetting matrices, the adsorption process can be much slower for thermoplastic matrices. It should not be surprising to find that it takes long times at high temperature to promote good adhesion in thermoplastic matrix composites [5, 6].

Kardos *et al.* [28, 29] found that annealing polycarbonate (PC) composites with random chopped carbon fibers at 245°C for three hours increases both the tensile strength and the modulus. On the basis of electron diffraction results, they attributed the increases to a transcrystalline region along the fibers. Brady *et al.* [5, 6], did annealing experiments on unidirectional PC/carbon fiber composites. They found that the interfacial toughness, as measured using a buckled plate specimen [6, 37], increases with annealing time and increases faster at higher annealing temperatures. Because increased toughness could be induced by annealing above the melting point of PC (i.e. above 220-260°C [38] for their conditions), they concluded that adsorption of the matrix onto the fiber, and not transcrystallinity, was the primary mechanism for the improved interface. They supported their adsorption interpretation by qualitatively fitting interface toughness data to Langmuir-type adsorption isotherms with kinetic parameters following Arrhenius activation energy theory [5].

Three important consequences follow from the work of Brady *et al.* [5, 6]. First, adsorption of a thermoplastic matrix onto carbon fibers can be an important step in the processing of thermoplastic composites. If a composite sees insufficient processing time at high temperature, it is possible to get a composite in which the matrix has fully penetrated the fibers, but lack of adsorption has caused a poor fiber/matrix interface. In other words, results from optical microscopy alone is inadequate for assessing the processing of thermoplastic composites. Second, adsorption of high-molecular-weight thermoplastics onto carbon fibers can be a slow process; it can take several hours at elevated temperatures. Third, annealing treatments provide a useful scientific tool for studying the effect of the interface on composite properties. Provided the annealing treatment does not change the bulk properties of the matrix (e.g. by degradation or by changes in crystallinity), annealing of thermoplastic matrix composites provides a method for systematically changing the interface while all other composite properties remain the same.

In this project we used the annealing methods of Brady *et al.* [5, 6] to further study the

interface in unidirectional PC/carbon fiber composites. In agreement with previous results [5, 6], we found that annealing PC/carbon fiber composites leads to a significant increase in transverse toughness. The increase, however, can be inhibited by pressure. Processing conditions that include long times at high temperature under high pressure give a smaller increase in toughness than those that include long times at high temperature but under low pressure. We further studied the longitudinal compression strength of a series of unidirectional composites with varying interfacial toughness. We found an increase in compression strength that paralleled the increase in interfacial toughness. We suggest that these results give experimental proof that the fiber/matrix interface has a direct and large effect on compression strength.

5.2 Materials and Methods

12K Magnamite AS4 carbon fiber yarns (lot number 758-4B) were supplied by Hercules, Inc., Magna, Utah. AS4 is classified as a Type II intermediate strength fiber with a density of 1.796 g/cm^3 . General Electric Lexan[®] polycarbonate was purchased as a roll of 3-mil film. Its measured density was 1.172 g/cm^3 .

Unidirectional three-ply composite plates of PC/AS4 carbon fiber were fabricated by a film stacking technique. 6 inch \times 6 inch steel plates with rounded edges were covered with 3 mil DuPont Kapton[®] polyimide film and then with PC film. These plates were loaded into a hand-cranked, card-winding machine. AS4 yarns, whose width had been approximately doubled by air spreader bars, were wrapped around the plates using the card-winding mechanism. Two more layers of PC film and AS4 fibers were added followed by final layers of PC and Kapton[®] film. The Kapton[®] film provided a release layer that helped in sample removal from the steel plate. The steel plates with the three-ply composites were placed in a vacuum oven for a minimum of 12 hours at approximately 100°C to eliminate any moisture and to desorb volatiles prior to high-temperature

processing. Each plates was then placed inside a vacuum bag of 3-mil Kapton[®] film, sealed with Tacky Tape (Schnee-Morehead Chemicals), and collapsed by application of laboratory vacuum. The vacuum-bagged composites were consolidated in a Carver Hot Press for selected processing times and temperatures under a pressure of 0.96 MPa (139 psi). The pressure was allowed to stabilize for approximately 2 minutes before starting the process timer. After selected processing times, the composites were cooled in the press, under pressure, to room temperature by passing laboratory distilled water through the channels inside the two heated platens. The composite cooling rate was approximately 25°C per minute. The thicknesses of the three-ply composites produced by this procedure ranged from 0.44 to 0.69 mm (17 to 27 mils). Fiber volume fractions were determined by measuring composite density and extrapolating between the density of carbon fiber (1.796 g/cm³) and PC (1.172 g/cm³). Composite densities were measured with a density gradient column prepared according to the guidelines of ASTM D-1505-68, Method C [39]. A water-calcium nitrate system was used to cover the desired density range of 1.3–1.5 g/cm³.

We used transverse buckled plate tests [6, 37] to evaluate the effect of processing time on the fiber/matrix interface. When a unidirectional composite is notched parallel to the fibers and transversely loaded in compression, it buckles at a critical load of

$$P_c = \frac{\pi^2 E w h^3}{12 \ell^2} \quad (5.1)$$

where ℓ is length, $w = W - a$ is the total width (W) minus the notch depth (a), h is thickness, and E is the composite transverse modulus. During post-buckling, the displacement will increase until the crack propagates causing catastrophic failure. Chang and Donovan [37] showed that the energy release rate for crack growth is independent of the initial notch depth and is given by the expression

$$G = 0.82 \frac{E h^2 (\ell - x)}{\ell^2} f^*(\epsilon) \quad (5.2)$$

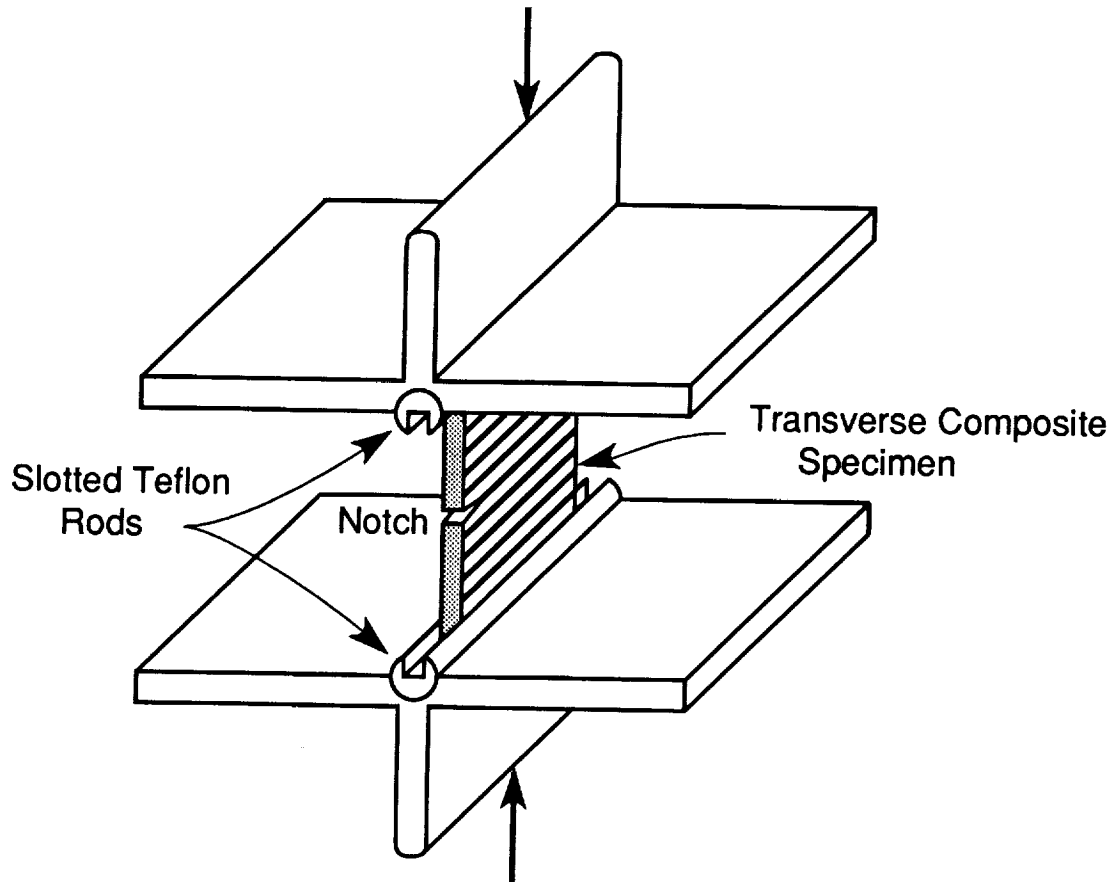


Figure 5.1: Testing fixture for the buckled plate (BP) test. The transverse composite specimen (fibers perpendicular to the applied load) is compressed between two plates. The ends of the specimen are held in slotted Teflon® rods to allow free rotation of the ends.

where x is the chord length of the buckled plate (thus $\ell - x$ is total measured displacement), and

$$f^*(\epsilon) = 0.158\epsilon^2 + 0.229\epsilon + 1 \quad (5.3)$$

is a function of strain, $\epsilon = (\ell - x)/\ell$. For low strains ($\epsilon \leq 30\%$), $f^*(\epsilon)$ is close to unity; we treated it as equal to unity in this study.

The buckled plate (BP) testing apparatus is shown in Fig. 5.1. The BP specimen dimensions were 30 mm high by 15 mm wide. These dimensions were achieved by sanding with 220- and 400-grit silicon carbide sandpaper with the sample clamped in a stainless steel jig. The upper and lower edges (parallel to the fiber direction) were sanded gently to roundness with 400-grit silicon carbide sandpaper. 1- or 2-mm notches parallel to the fiber direction were cut with fresh razor blades along

the mid-line of each specimen. These notched samples were mounted in slotted Teflon[®] rods and buckled in compression until fracture. Teflon[®] fluorinated ethylene-propylene rods, lubricated with Sprayon 708 TFE Dry Lube, were used to allow free rotation of the ends. At the instant of fracture, Eq. (5.2) gives the transverse fracture toughness, G_c . Because G is independent of notch depth, the notches did not need to be measured prior to testing. In principle, the transverse modulus, E , can be calculated from the buckling load of the notched specimen prior to its fracture. This practice, however, tends to overestimate the effective buckling modulus [6]. As recommended in Ref. [6], we measured E from the buckling loads of unnotched plates.

Compression testing of the thin three-ply specimens was done using the method described in Refs. [23] and [40] and in Chapter 3. In brief, three-ply composites were cut into mini-dog-bone specimens 25 mm long by 20 mm wide. These specimens were embedded in a clear epoxy resin consisting of Dow Chemical DER 332 + Texaco Jeffamine D-230 + Texaco Accelerator 399 in the weight ratio of 10 : 3.5 : 1. These embedded specimens were loaded in compression with shim stock that matched the total embedded specimen thickness. To prevent premature buckling failures, the specimens were side supported during testing. The compression testing apparatus and specimen geometry are illustrated in Fig. 5.2.

The composite compression strength was calculated from the failure load, P_{total} , by a simple rule-of-mixtures formula

$$\sigma_c = \frac{P_{total} E_c}{E_c A_c + E_e A_e} \quad (5.4)$$

where E_c and E_e are the moduli of the three-ply composite and of the embedding epoxy. A_c and A_e are the cross-sectional areas of the three-ply composite and of the embedding epoxy at the location of compression failure. With the mini-dog-bone specimens, the compression failure was always at the point of minimum composite cross-sectional area. E_e was measured by compression tests on straight-sided specimens of pure epoxy [23, 40].

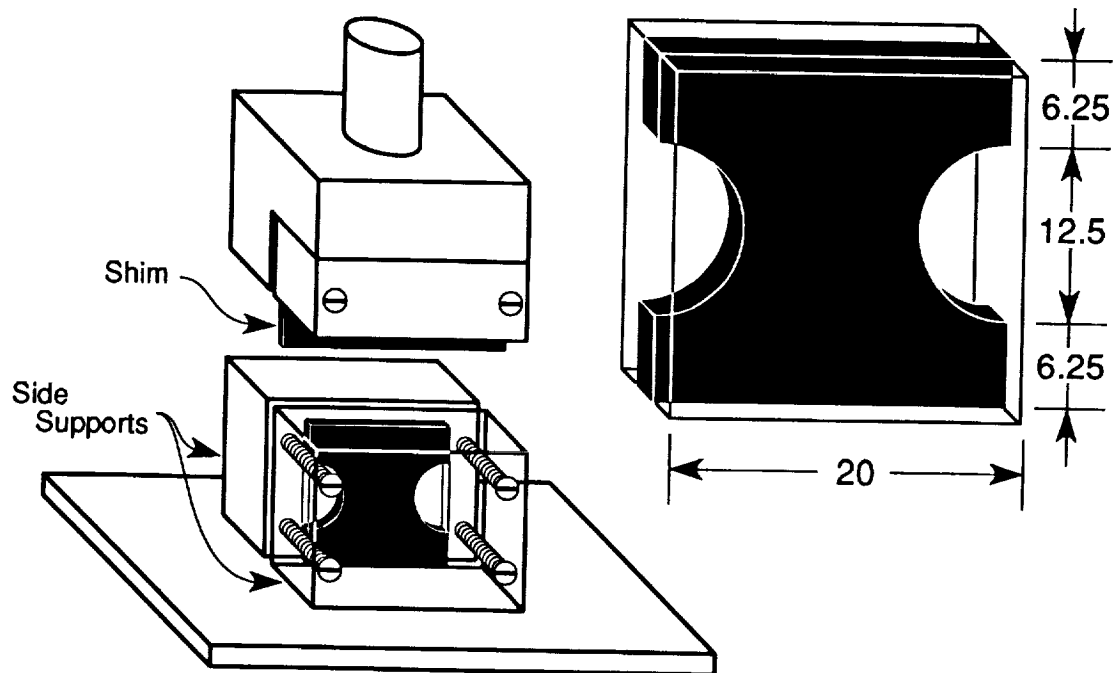


Figure 5.2: The composite compression test fixture and an enlargement of the embedded three-ply composite test specimen. The embedded three-ply composite specimens were positioned between two side supports. The rear side support was steel. A transparent, poly-methyl methacrylate front side support was used to permit observation of the failure process. Compression load was applied by a steel shim having a thickness matching that of the embedded three-ply composite specimen. Specimen dimensions are nominal and are in mm.

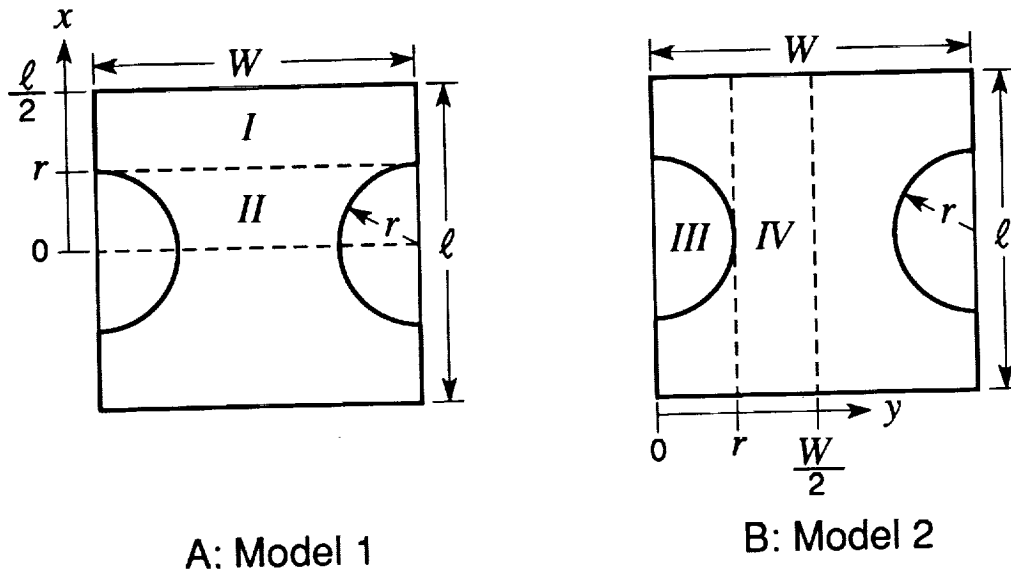


Figure 5.3: Regions of the embedded mini-dog-bone composite specimen used to calculate upper and lower bound composite moduli. A. Regions for the chain-of-disks model (model 1). B. Regions for the rack-of-disks model (model 2).

E_c can be measured by compression tests on embedded straight-sided composite specimens using a simple rule-of-mixtures [23, 40]. For the home-made specimens in this study, it was preferable to measure E_c on the same mini-dog-bone specimens used to measure compression strengths. We thus discuss a simple procedure for estimating upper and lower bounds on E_c from knowledge of E_e , E_{eff} (the specimen modulus), and specimen dimensions.

For model 1 (Fig. 5.3A) we consider a specimen of length ℓ , width W , thickness t , and cross-sectional area A , whose stiffness varies along its length. By making horizontal slices, we divide it into a chain of disks where each disk has the same cross-sectional area, but a different modulus. Modeling the chain of disks as springs in series and passing to the limit of an infinite number of disks, the specimen modulus is

$$\frac{1}{E_{eff}} = \frac{1}{\ell} \int_{-\ell/2}^{\ell/2} \frac{1}{E(x)} dx \quad (5.5)$$

where $E(x)$ is the modulus as a function of position along its length. Model 1 splits the symmetric compression specimen into two regions. In region I, the composite cross-sectional area is constant.

Therefore, $E(x)$ is constant; by a rule-of-mixtures analysis it is

$$E(x) = E_R = \frac{E_e(t - t_c) + E_c t_c}{t} \quad \text{for } r < x < \ell/2 \quad (5.6)$$

where t_c is composite thickness. The cut-out in region *II* is an arc of radius r . By a rule-of-mixtures analysis, the modulus at position x is

$$E(x) = \frac{E_e(A - A_c(x)) + E_c A_c(x)}{A} = E_R \left(1 + \beta_1 \sqrt{r^2 - x^2} \right) \quad \text{for } 0 < x < r \quad (5.7)$$

where $A_c(x)$ is the cross-sectional area of the composite at position x and

$$\beta_1 = -\frac{2t_c}{tW} \frac{E_c - E_e}{E_R} \quad (5.8)$$

Combining Eqs. (5.5), (5.6), and (5.7), the specimen modulus by model 1 is

$$\frac{1}{E_{eff}} = \frac{1}{\ell E_R} (\ell - 2r + 2I(\beta_1)) \quad (5.9)$$

where

$$I(\beta) = \int_0^r \frac{dx}{1 + \beta \sqrt{r^2 - x^2}} \quad (5.10)$$

For model 2 (Fig. 5.3B) we consider a specimen whose stiffness varies along its width. By making vertical slices, we slice it into a rack of disks where each disk has the same cross-sectional area, but a different modulus. Modeling the rack of disks as springs in parallel and passing to the limit of an infinite number of disks, the specimen modulus is

$$E_{eff} = \frac{1}{W} \int_{-W/2}^{W/2} E(y) dy \quad (5.11)$$

Figure 5.3B splits the symmetric compression specimen into two regions. In region *IV*, the composite longitudinal-sectional area is constant and $E(y)$ is equal to E_R (a constant). We model each position in region *III* as three springs in series. The middle spring is the region of pure embedding epoxy ($|x| < \sqrt{r^2 - y^2}$). Its length is

$$\ell_2 = 2\sqrt{r^2 - y^2} \quad (5.12)$$

and its modulus is E_e . The top and bottom springs are regions of composite embedded in epoxy ($|x| > \sqrt{r^2 - y^2}$). Their lengths are

$$\ell_1 = \ell_3 = \frac{\ell}{2} - \sqrt{r^2 - y^2} \quad (5.13)$$

and their moduli are both E_R . Analyzing the three series springs, the modulus in region III is

$$E(y) = \frac{E_R}{1 + \beta_2 \sqrt{r^2 - x^2}} \quad \text{for } 0 < y < r \quad (5.14)$$

where

$$\beta_2 = \frac{2}{\ell} \frac{E_R - E_e}{E_e} \quad (5.15)$$

Combining Eqs. (5.11) and (5.14), the specimen modulus by model 2 is

$$E_{eff} = \frac{E_R}{W} (W - 2r + 2I(\beta_2)) \quad (5.16)$$

The same $I(\beta)$ function appears in each model. It can be integrated in closed form:

$$I(\beta) = \begin{cases} \frac{1}{2\beta} \left(\pi - \frac{4}{\sqrt{1-\beta^2 r^2}} \tan^{-1} \frac{\sqrt{1-\beta^2 r^2}}{1-\beta r} \right) & \text{for } 1 - \beta^2 r^2 > 0 \\ r & \text{for } 1 - \beta^2 r^2 = 0 \\ \frac{1}{2\beta} \left(\pi - \frac{2}{\sqrt{\beta^2 r^2 - 1}} \ln \frac{1+\beta r + \sqrt{\beta^2 r^2 - 1}}{1+\beta r - \sqrt{\beta^2 r^2 - 1}} \right) & \text{for } 1 - \beta^2 r^2 < 0 \end{cases} \quad (5.17)$$

To find the composite modulus for a mini-dog-bone composite embedded in an epoxy, we numerically solved Eqs. (5.9) and (5.16) for E_c . We claim (without proof) that the series model (model 1) gives a lower bound to E_c and that the parallel model (model 2) gives an upper bound to E_c . These upper and lower bound moduli can then be substituted into Eq. (5.4) to find upper and lower bounds for the compression strengths. Because E_c was always much greater than E_e , the bounds on σ_c calculated with Eq. (5.4) were always very tight. The bounds on σ_c and on E_c are incorporated within the errors bars in Figs. 5.8 and 5.9 (See *Results and Discussion* section).

A servohydraulic Minnesota Testing Systems (MTS) Model 810 load frame under displacement control with a 2.5-kN reversible load cell was used for all testing. Data was collected on an IBM PC

Model 5153 system using custom-developed software interfaced to an MTS Data Display Device. All buckled plate specimens were compressed at a rate of 0.33 mm/sec. All embedded, mini-dog-bone, compression specimens were loaded at a rate of 0.01 mm/sec. All experiments were done under ambient conditions.

Scanning electron micrographs (SEM) of BP specimens were collected on a Stereoscan 240 manufactured by Cambridge Instruments, Limited, of Cambridge, England. Samples were coated with gold using a Hummer V pulsed, planar, magnetron-type sputtering system, manufactured by Technics Corporation of Alexandria, Virginia. The SEM specimens were prepared by mounting the BP specimen with the cracked region opened upward by bending the specimen into an inverted "V." Atomic force microscopy (AFM) force-modulation images of PC/carbon fiber composites were collected with a NanoScope II AFM manufactured by Digital Instruments, Inc., of Santa Barbara, California. Sample data were processed with force-modulation software.

5.3 Results and Discussion

5.3.1 Transverse Fracture Toughness

Transverse fracture toughness measured in the buckled plate (BP) test characterizes some combination of crack growth through the matrix and crack growth along the fiber/matrix interface. The relative importance of matrix cohesive fracture and interfacial adhesive failure depends on the relative magnitudes of the toughnesses for these two fracture mechanisms. In a series of specimens with identical matrices and nominally identical microstructures, it is logical to ascribe most of the changes in transverse fracture toughness to changes in the interfacial properties of the composite. We thus used transverse buckling of notched, unidirectional composite specimens [6, 37] to study the effect of processing conditions on interfacial properties.

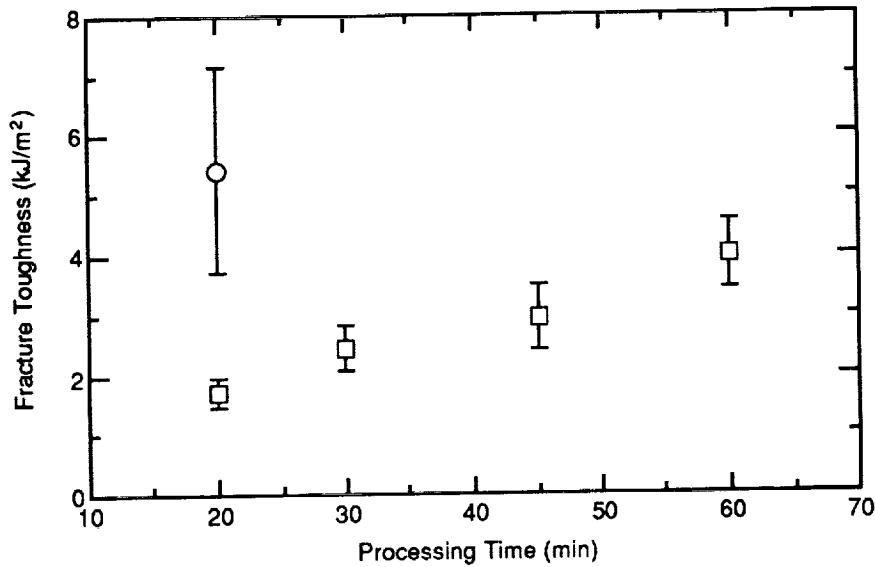


Figure 5.4: Transverse fracture toughness *vs.* processing time of PC/carbon fiber composites processed at 300°C under a constant 0.96 MPa consolidation pressure. The circle is for a composite annealed for three hours at 275°C after initial processing at 300°C and 0.96 MPa for 20 minutes. Error bars represent one standard deviation.

A series of three-ply PC/carbon fiber composites was molded in a 300°C hot press under a constant consolidation pressure of 0.96 MPa. Figure 5.4 plots the transverse fracture toughness as a function of molding time. The toughness increased 133% from 1.71 kJ/m² for the 20-min composite to 3.98 kJ/m² for the 60-min composite. Figure 5.4 shows an additional point (a circle) corresponding to 20-min composites that were further annealed for three hours at 275°C with the pressure maintained at 0.96 MPa. For this composite the fracture toughness was 217% larger (5.42 kJ/m²) than the corresponding unannealed 20-min composite. These results indicate that longer molding times, at 300°C or at 275°C, give improvements in the interphase of PC/carbon fiber composites. The findings are similar to the results reported by Brady *et al.* [5, 6], except that consolidation pressure was held high throughout the processing, and that the magnitude of the increase was smaller (133% *vs.* about 200% [5, 6]).

We agree with Brady *et al.* [5, 6] that the improvements in transverse fracture toughness are due to the time required for the PC matrix to adsorb onto the carbon fibers. The improvements

in interfacial toughness were clearly unrelated to crystallization of PC near the interface. Both the molding (300°C) and the annealing (275°C) temperatures were above the melting point of PC for these annealing conditions [38]. For all processing conditions, the final step was to cool rapidly to room temperature at about 25°C/min. Thus even if the difficult-to-crystallize PC could form crystals, the level of crystallinity would be relatively constant from specimen to specimen. The improvements in the interface were also unrelated to composite quality—by quality we mean macroscopic extent of matrix/fiber interpenetration. Two observations support this conclusion. First, both optical microscopy and atomic force microscopy reveal no obvious differences in the fiber/matrix distribution between the 20-min composites and the 60-min composites. Second, annealing without any applied pressure improved the interface. Pressure is probably a prerequisite for significant changes in interpenetration.

We supplemented the work of Brady *et al.* [5, 6] by studying the effect of composite consolidation pressure. A series of three-ply, PC/carbon fiber composites was molded at 300°C for 60 minutes. During molding, the composites were under a pressure of 0.96 MPa for a variable amount of time and for the remaining time there were under vacuum-bag pressure only. Figure 5.5 plots the transverse fracture toughness as a function of time under 0.96 MPa pressure. There was some benefit to applying consolidation pressure. The toughness after 2 minutes of pressure was higher than the toughness achieved without any applied pressure. After the initial improvement in toughness, however, no further benefit was found by continued application of pressure. Rather, continued application of pressure caused the composite toughness to decrease. A possible explanation for these results is a pressure effect on adsorption of the matrix onto the fiber surface. Pressure could inhibit adsorption either by increasing the melt viscosity of PC or by causing fiber/fiber contact zones that cannot be penetrated by the matrix.

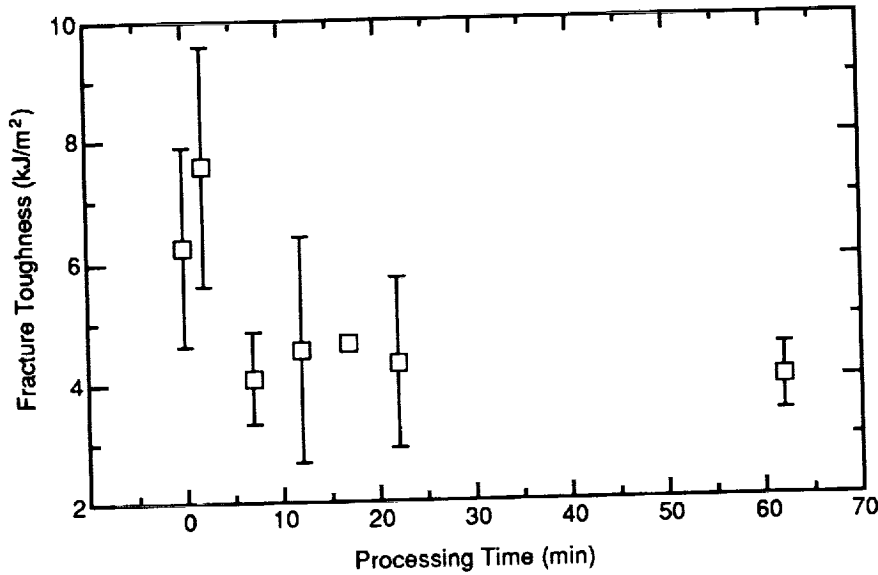


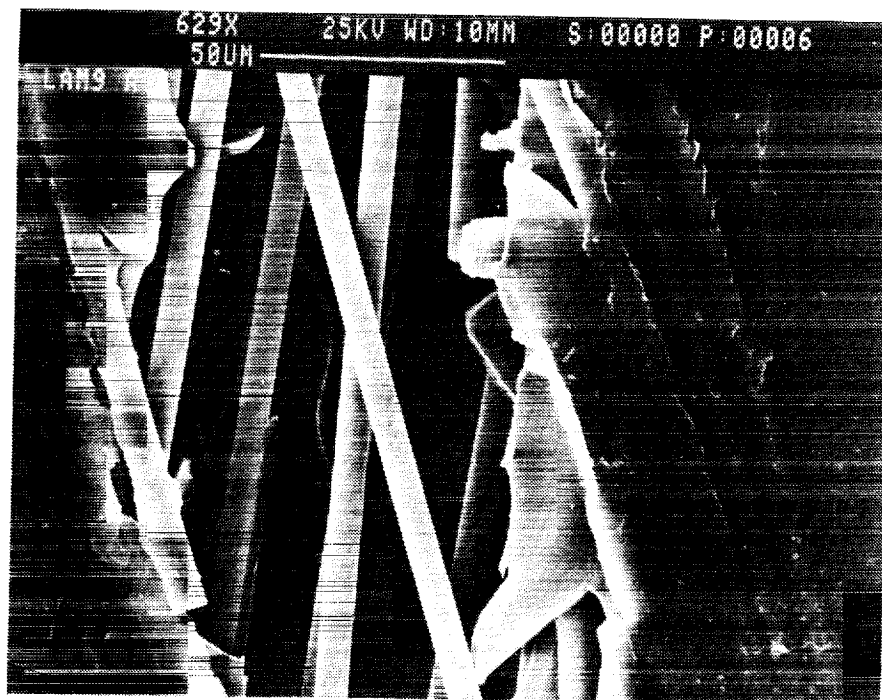
Figure 5.5: Transverse fracture toughness vs. composite processing pressure hold time at 0.96 MPa. Vacuum-bag pressure only is defined as zero hold time. All composites were processed at 300°C for 60 minutes. Error bars represent one standard deviation.

5.3.2 Microscopy

The SEM micrographs in Fig. 5.6 are consistent with an interpretation of an improved fiber/matrix adhesion following annealing treatments. Figure 5.6A shows a composite that was processed at 300°C for 20 minutes under a pressure of 0.96 MPa. The fibers appear bare, indicating weak adhesion. Figure 5.6B shows a composite that was processed at 300°C for 20 minutes under a pressure of 0.96 MPa and 40 minutes under vacuum bag pressure only. The 60-min composite showed more evidence of the PC matrix sticking to the fibers and elongating during failure.

Maivald *et al.* [41] evaluated elasticity atomic force microscopy (AFM) using a force-modulation mode to image a Celion G-30 carbon fiber/Fiberite 941 epoxy resin composite in cross-section. In brief, a nano-probe is moved over the surface of an object and the force is held approximately constant through a feedback loop. At each scanned position, a small motion with an amplitude of about 25 nm, Δz_m , is introduced into the z -direction of the specimen position. This motion causes a small motion of the nano-probe of Δz_d . The magnitude of $\Delta z_m/\Delta z_d$ provides a measure of surface elasticity. The quantity $\Delta z_m/\Delta z_d$ approaches one over hard areas and is smaller over soft

A: Specimen that was processed for 20 minutes at 300°C and 0.96 MPa.



B: Specimen that was processed for 60 minutes at 300°C. The first 20 minutes were at 0.96 MPa. The remaining 40 minutes were at vacuum-bag pressure only.

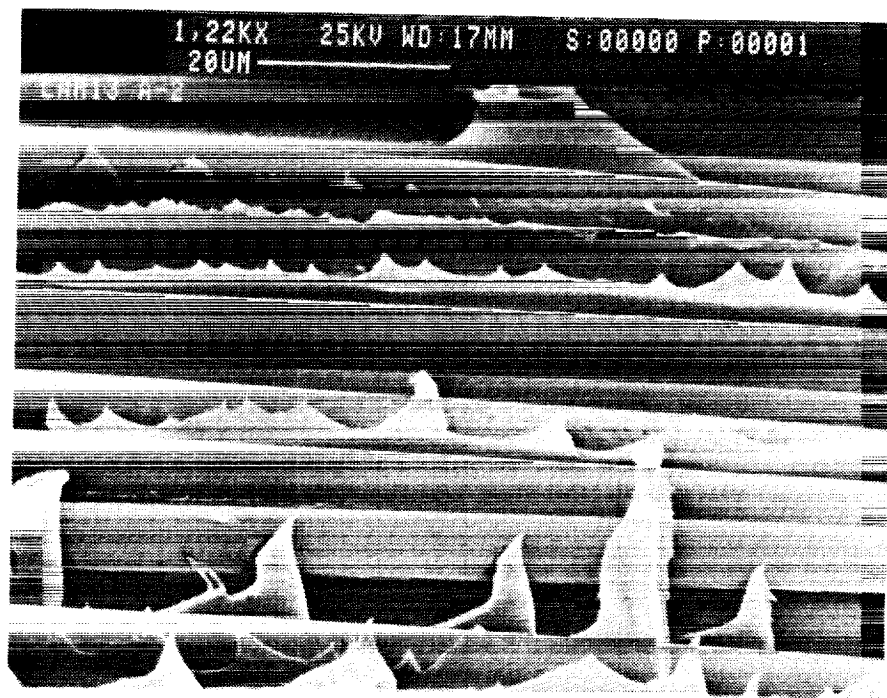


Figure 5.6: SEM micrographs of fracture surfaces of buckled plate specimens.

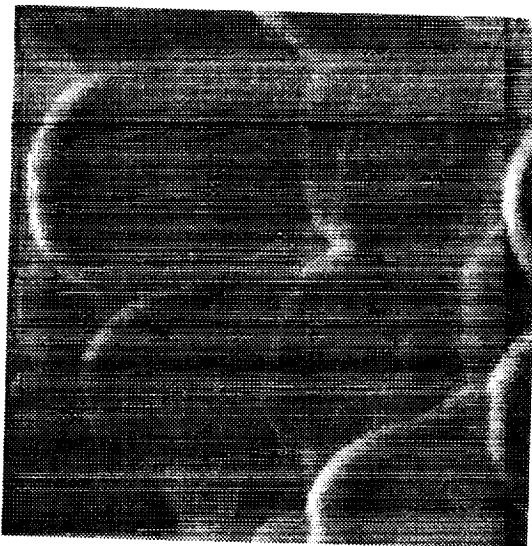
areas. Thus, imaging $\Delta z_m/\Delta z_d$ over the scanned surface images differences in surface elasticities [41]. The resolution of AFM is more than adequate to image 7- μm carbon fibers.

We used force-modulation AFM to image cross-sections of composites processed under different conditions. The AFM images of polished cross sections of PC/carbon fiber composites are shown in Fig. 5.7. The force-modulation surface images were obtained by scanning in a raster pattern over a selected region of the composite. The area imaged in the figures is 15796 nm \times 15796 nm. Our qualitative interpretation of the AFM images focused on image contrast as a descriptor of differences in surface elasticity. Figure 5.7A shows a 20-min composite. There is sharp contrast between the fibers and the matrix. We attempted no quantitative analysis, but the interfacial region is easily detected by the AFM probe. In contrast, the 60-min composite in Fig. 5.7B shows much lower contrast. The process of the matrix adsorbing onto the fiber makes the interfacial region more transparent to the AFM probe. The AFM contrast changes at the interface correlated with the changes in interfacial properties measured by the BP test. In other words, AFM imaging can be a useful tool for making direct observations of changes at the interface.

5.3.3 Compression Strength Testing

The effect of processing time on the interfacial properties of PC/carbon fiber composites has important implications about the optimal processing of thermoplastic matrix composites. A side-benefit is that processing time provides a method for controlling the interface. By processing composites for different amounts of time it is possible to get a series of specimens in which the only variable is interfacial toughness. The matrix, the fiber, and the nominal microstructure will be identical while only the interface is changing. Such a series of composites provides ideal specimens for studying the effect of the interface on any composite property. In this section we discuss the effect of the interface on compression strength.

A. Composite processed for 20 minutes at 300°C under a consolidation pressure of 0.96 MPa.



B. Composite processed for 60 minutes at 300°C under a consolidation pressure of 0.96 MPa.



Figure 5.7: An AFM force-modulation images of PC/carbon fiber composites

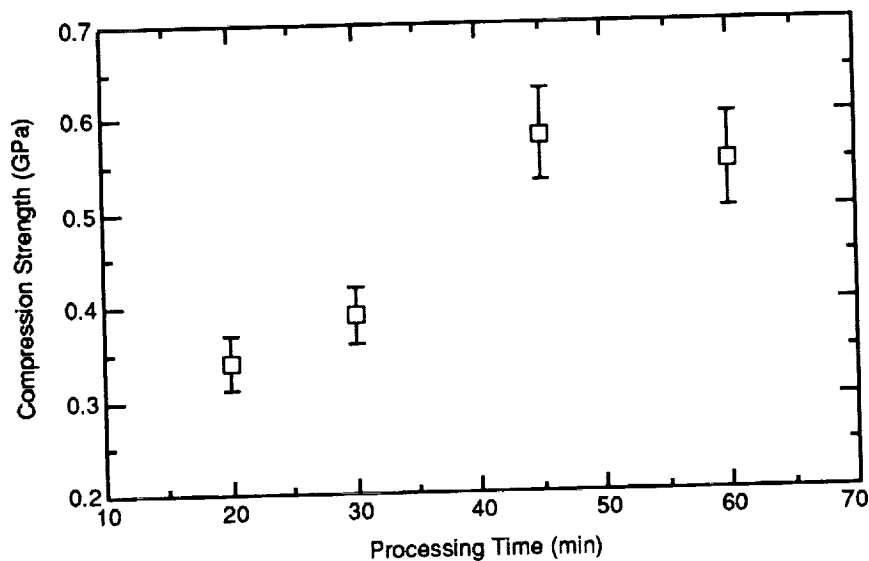


Figure 5.8: Longitudinal compression strength *vs.* processing time of PC/carbon fiber composites processed at 300°C and 0.96 MPa consolidation pressure. Error bars represent one standard deviation.

A series of three-ply composites, identical to those used for Fig. 5.4, were molded at 300°C under a constant consolidation pressure of 0.96 MPa for variable amounts of time. The compression strength was measured, as described in the *Materials and Methods* section, by embedding mini-dog-bone specimens in a clear epoxy and end-loading side-supported specimens in compression. Figure 5.8 plots the compression strength as a function of composite processing time. The plot shows a significant increase in PC/carbon fiber compression strength with increased processing time. This increase in strength parallels the increase in interfacial toughness shown in Fig. 5.4 and suggests a direct relation between interfacial toughness and compression strength.

The 0° compression strengths reported for several commercial unidirectional AS4 carbon fiber/thermoplastic composites fall in the range of 0.9–1.4 GPa [26]. In contrast, our results range from 0.32 GPa to 0.58 GPa. These differences mainly reflect the fiber volume fractions. Commercial composites normally strive for high volume fractions— $V_f = 60\%$ or higher. Our home-made composites had fiber volume fractions of $35 \pm 5\%$.

Polycarbonate is a matrix of relatively low modulus. In PC/carbon fiber composites under

0° longitudinal compression, it is therefore likely that fiber buckling dominates or influences the failure mode [1, 42]. In our test, the bulk matrix properties were constant, and only the interphase properties were changed by the processing conditions. The increase in compression strength for PC/carbon fiber composites with processing time thus indicates that fiber buckling failure was inhibited by improved interfacial properties and improved fiber-matrix bonding.

The longitudinal compression modulus data are plotted against composite processing time in Fig. 5.9. An unexpected result was a significant increase in compression modulus with processing time. We suggest that the low modulus for composites with a poor fiber/matrix interface (short processing times) was caused by fiber microbuckling. Thus, the same mechanism that was responsible for a low compression strength may also be responsible for a low compression modulus. As the interface was improved by longer processing times, the microbuckling mechanism became inhibited and both the compression strength and the compression modulus increased. Other possible variables, such as bulk matrix modulus, were disregarded because only the fiber/matrix interface was altered by varying the processing conditions. A way to verify the effect of microbuckling on compression modulus is to do tension testing. Under tensile loading fiber buckling cannot occur. Therefore, unlike the compression modulus, the tensile modulus should be independent of composite processing time. This work is in progress.

5.4 Conclusions

In agreement with previous results by Brady *et al.* [5, 6], annealing PC/carbon fiber composites for long times at high temperature increases the toughness of the fiber/matrix interface. Besides annealing temperature, pressure is also an important processing variable. If pressure is held high for too long, the improvements in the interface suffer. If no pressure is used, however, the interface can also be poor. We suggest that pressure must be used initially until the matrix fully interpenetrates

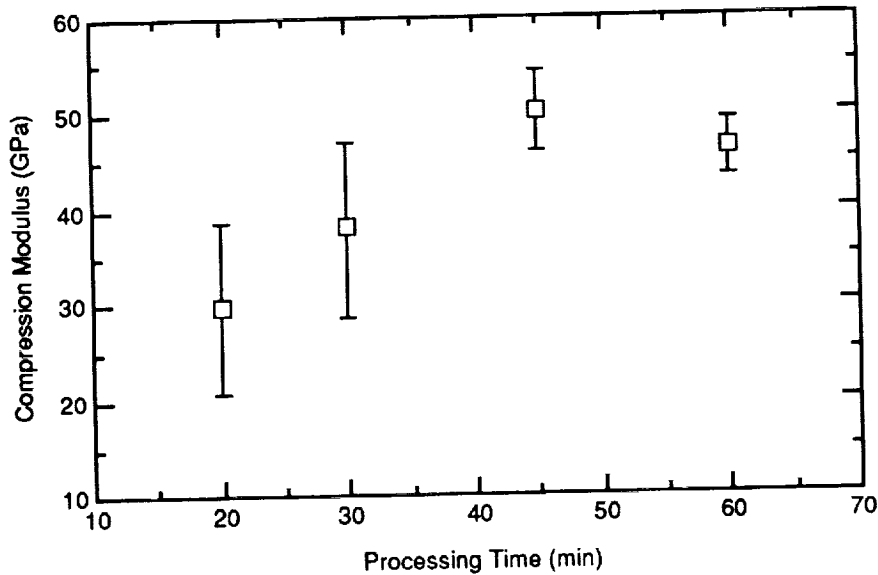


Figure 5.9: Longitudinal compression modulus *vs.* processing time of PC/carbon fiber composites processed at 300°C and 0.96 MPa consolidation pressure. Error bars represent one standard deviation.

with the fibers. The optimal processing conditions are to remove the pressure, once the fiber tows are penetrated, and to hold for enough time at high temperature to permit the matrix to adsorb onto the fibers.

Three pieces of experimental evidence suggest that the interface changes with high-temperature annealing. First, transverse fracture toughness measured by a BP test increases with annealing time. Second, SEM micrographs suggest more matrix adhering to the fibers in composites that were annealed for longer times. Third, AFM force-modulation images indicate changes in the interfacial region that are associated with elastic properties of the interface. The AFM images alone cannot differentiate between good and poor interface properties. AFM is interesting, however, as a potential tool for direct observation of interfacial regions.

This study is possibly the first one to measure compression strength where the only material variable is interfacial toughness. By using annealing treatments to change the interfacial toughness, we were able to isolate effects of the fiber/matrix interface—that is, the interfacial toughness was varied while other composite material properties were held constant. Both the compression strength

and the compression modulus increased significantly as the fiber/matrix interface improved. We suggest that inhibition of fiber microbuckling by an improved interface played a role in increasing the compression strength and modulus properties.

The performance of PC/carbon fiber composites is representative of thermoplastic composites in general. Thus, long processing times, similar to those of thermosetting systems, may be required to achieve satisfactory fracture toughness in thermoplastic composites. Pressure is also an important processing variable. Too much pressure for too long lengthens the time required to manufacture good composites.



Chapter 6

Mixed-Mode Precracking

6.1 Introduction

Delamination, or propagation of an interlaminar crack, is a common mode of failure in composite laminates. The presence of delaminations may cause complete fracture, but even partial delaminations will cause at least a loss of stiffness. The most common method for studying delaminations is to use fracture mechanics where the characterization is via the critical energy per unit crack growth— G_c . Because of the extreme anisotropy of the toughness of composite laminates, delamination crack growth is almost always interlaminar. By varying loading conditions, it is possible to study different modes of propagation. Some of the propagation modes observed in composites are not commonly observed in isotropic materials. The most obvious failure mode is mode I, the opening mode, which gives G_{Ic} . In certain bending geometries, the crack may propagate by sliding or shear motion, which is characterized by G_{IIc} . A combination of opening and shear loadings can give mixed-mode crack propagation which is characterized by a failure envelope of G_{II} vs. G_I .

In this project we looked at the effect of crack history on the mode I toughness or G_{Ic} . We subjected various specimens to mixed-mode precracking prior to a standard mode I test. We tested four different material types and found that crack history can have a significant effect on mode I toughness. The implication is that delamination is a complex process that not only depends on the

current loading conditions, but also depends on the delamination formation history.

6.2 Materials and Methods

The experiments were conducted on four different carbon fiber composite materials—AS4/3501-6, IM7/8552, IM7/XLASC, and IM7/2600. AS4/3501-6 and IM7/2600 are characterized as having homogeneous, untoughened epoxy matrices. IM7/8552 has a rubber toughened epoxy matrix. IM7/XLASC has a bismaleimide matrix with toughening interlayers between the plies. AS4/3501-6, IM7/8552, and IM7/XLASC were all made by autoclave processing according to the manufacturer's instructions. IM7/2600 was made in a hot press. All tested laminates were unidirectional laminates. The AS4/3501-6, IM7/8552, and IM7/XLASC laminates were 32 ply laminates. The IM7/2600 laminates were 24 ply laminates. All specimens were six inches long and one inch wide. Aluminum foil was inserted as a crack starter in the prepreg lay-up before autoclave curing. Hinges were glued to the ends of the specimens over the insert for mounting in the fixture described below.

There are various mixed mode testing methods available. In this study, the fixture developed by Reeder and Crews [43, 44] was used. Their mixed-mode bending (MMB) fixture combines a mode I double cantilever beam (DCB) test with a mode II end notch flexure (ENF) test. This combination is achieved by adding an opening mode load to a mid-span loaded ENF specimen as shown in Fig. 6.1. The additional load separates the arms of the unidirectional laminate as in a DCB test. A single applied load produces two reactionary forces, tensile and bending, at the hinge and at the lever. The loading position, c , determines the relative magnitude of the two resulting loads on the specimen and, therefore, determines the mixed-mode delamination ratio. Pure mode II loading occurs when the applied load is directly above the beam mid-span ($c = 0$). Pure mode I loading can be achieved by removing the loading beam and pulling up on the hinge. Mixed mode loading is achieved by varying c .

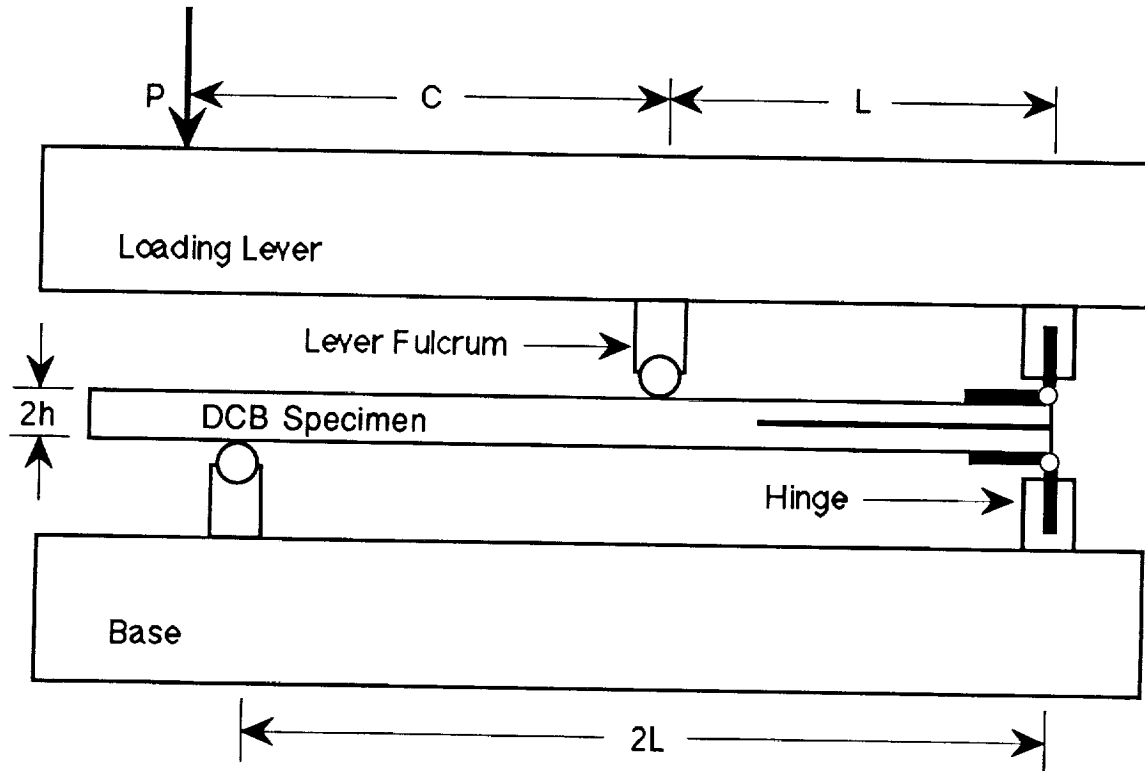


Figure 6.1: The mixed-mode bending fixture from Ref. [1] used to precrack DCB specimens at various mode I to mode II ratios. The mode I to mode II ratio was changed by varying c .

The Reeder and Crews [43, 44] MMB fixture was used to precrack the unidirectional delamination specimens. The initial crack length created by the aluminum foil crack starter was 20–35 mm. We precracked each specimen at a selected constant mixed-mode ratio until the delamination length was about 50 mm (15–30 mm of precrack growth). The precracking was done using three different ratios of mode I to mode II loading—4 to 1, 1 to 1, and 1 to 4. After precracking, each specimen was subjected to a pure mode I delamination test. During the mode I delamination test, the load and displacement were noted after each 5 mm of delamination crack propagation. This data was used, as described below, to calculate fracture toughness as a function of delamination length. Both the mixed-mode precracking and the mode I test were done in a 25 kN servohydraulic Minnesota Testing Systems (MTS) testing frame under displacement control. The displacement rate was always 0.03 inches/min.

As described above, the mixed-mode precracking was followed by a mode I delamination test.

According to the area method, the fracture toughness, or critical strain energy release rate in a mode I test is

$$G_{Ic} = \frac{P_1\delta_2 - P_2\delta_1}{2B(a_2 - a_1)} \quad (6.1)$$

where subscripts 1 and 2 refer to load (P), displacement (δ), or crack length (a) before and after a small amount of crack growth; B is the specimen thickness. Equation (6.1) is an exact definition of G_{Ic} , but it is imprecise because what is, in effect, a derivative must be determined numerically from two experimental measurements. Area methods suffer from other disadvantages. They determine only an average value of G_{Ic} over some change in delamination length. They are influenced by hysteretic energy losses and zero offset effects as discussed by Hashemi, Kinloch, and Williams [45].

It is often desirable to use beam theory, instead of the above area method, to analyze fracture results. According to beam theory of a DCB specimen, the mode I toughness is:

$$G_{Ic} = \frac{3P\delta}{2Ba} \quad (6.2)$$

This equation assumes that the compliance, C , at the crack root is zero, but in reality there is some deflection and rotation at the crack tip. It has been shown experimentally by Hashemi, Kinloch, and Williams [45] that this effect can be modeled by adding a length χh to the real crack length where χh is a constant which depends on the elastic properties of the material. It can be found experimentally from the intercept of a plot of $\sqrt[3]{C}$ vs. the measured delamination length, a . The corrected value of G_{Ic} becomes,

$$G_{Ic} = \frac{3P\delta}{2B(a + \chi h)} \quad (6.3)$$

We used Eq. (6.3) to measure mode I fracture toughness as function of delamination length. For each material and each precracking condition we determined χh by plotting $\sqrt[3]{C}$ vs. a . A typical result for IM7/8552 is given in Fig. 6.2. The intercept when $C = 0$ gives $\chi h = 3.5$ mm. For all specimens, the measured values of χh ranged from 0 mm to 12 mm.

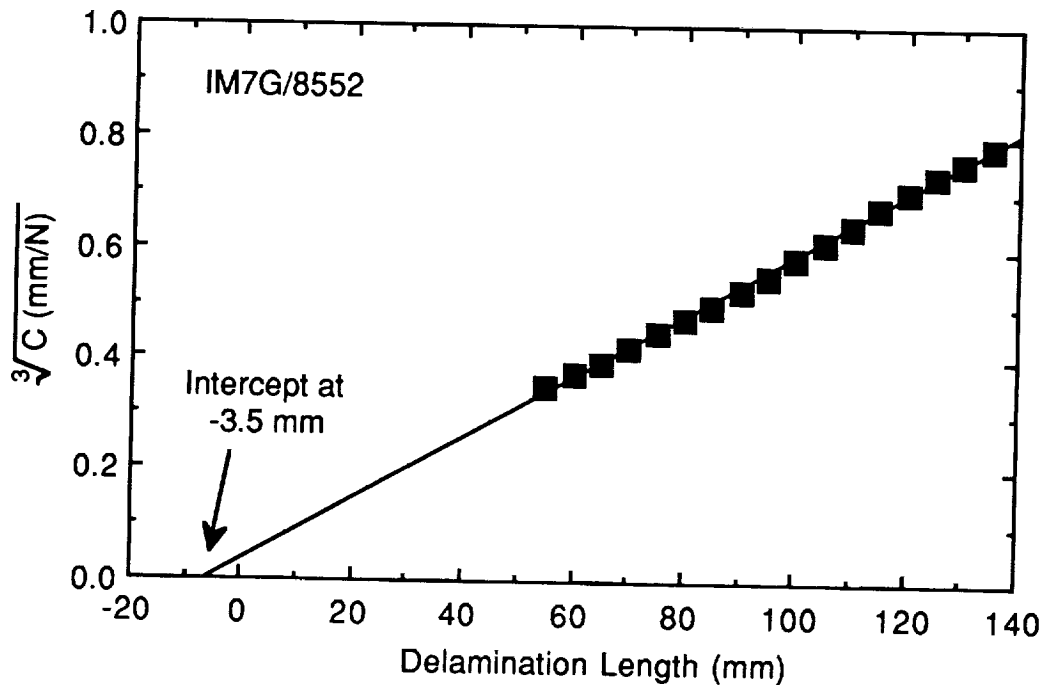


Figure 6.2: A plot of $C^{1/3}$ as a function of delamination length for a IM7/8552 laminate. The intercept on the x axis defines the crack length correction factor for this material.

6.3 Experimental Results

For each material and for each precracking mode ratio, we measured the mode I fracture toughness as a function of delamination growth length. Some typical results at a mode I to mode II precracking ratio of 4 to 1 are given in Fig. 6.3. All results follow a similar pattern. They begin with some mode I toughness (which may be high or low) and eventually level off at some steady state value. The steady state value occurs after there has been enough crack growth to insure that the mode I crack *forgets* about the precracking mode ratio. Surprisingly it can take as much as 60 mm of mode I crack growth to reach the steady state value. The steady state toughnesses of the four materials were as follows:

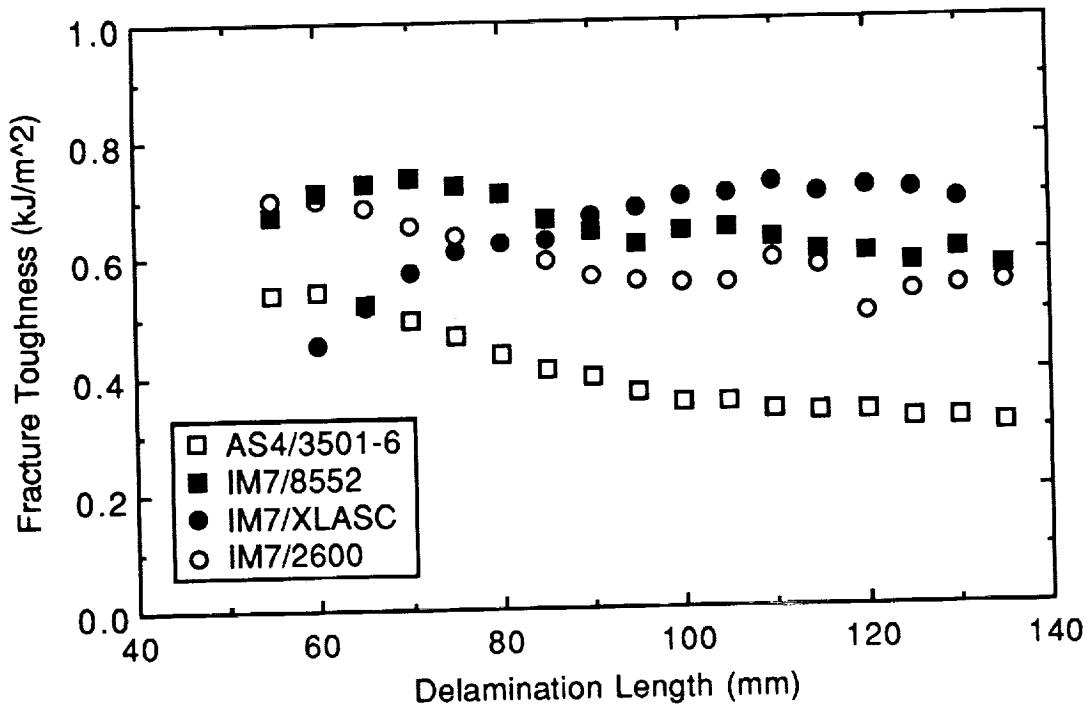


Figure 6.3: Mode I fracture toughness as a function a delamination length for all materials following mixed-mode precracking using a mode I to mode II ratio of 4:1

$$\text{AS4/3501 - 6} \quad G_{Ic} = 0.28 \pm 0.02 \text{ kJ/m}^2$$

$$\text{IM7/2600} \quad G_{Ic} = 0.50 \pm 0.02 \text{ kJ/m}^2$$

$$\text{IM7/8552} \quad G_{Ic} = 0.60 \pm 0.10 \text{ kJ/m}^2$$

$$\text{IM7/XLASC} \quad G_{Ic} = 0.66 \pm 0.04 \text{ kJ/m}^2$$

The steady state toughnesses were independent of the precracking mode ratio. The steady state results were reproducible with the most variable results coming from the IM7/8552 laminates. For the first 60 mm of crack growth, the mode I toughnesses of each material may differ significantly from its steady state toughness. The remainder of this section discusses the effect of precracking on the early mode I crack growth.

Figure 6.3 shows the mode I toughness of each material following a precracking mode I to mode II ratio of 4 to 1. Of the ratios we used, this ratio had the highest amount of mode I loading and should therefore be expected to produce the smallest effects. All materials, except IM7/XLASC,

showed a slight decreasing trend in mode I toughness during early crack growth. For these materials the initial mode I toughnesses were 10% to 40% higher than the steady state toughnesses. As crack growth increased the mode I toughnesses decreased towards the steady state toughnesses. For IM7/XLASC, the initial mode I toughness was about 35% lower than the steady state toughness. The IM7/XLASC was unique in using toughening interlayers. These results suggest that materials with toughening interlayers are susceptible to decreases in mode I toughness when they experience mixed-mode precracking.

Figure 6.4 shows the mode I toughness of each material following a precracking mode I to mode II ratio of 1 to 1. The two toughened materials (solid symbols in Fig. 6.4) showed a slightly lower (10% to 35%) mode I toughness at early stages in crack growth relative to the steady state toughness. The two untoughened systems (open symbols in Fig. 6.4) showed a slightly higher (15% to 50%) mode I toughness at early stages in crack growth. An interesting observation is that both of the untoughened composite material systems have a higher mode I toughness during early stages of crack growth than either of the toughened systems. These results suggest that toughening methods that enhance pure mode I toughness may be ineffective or less effective following mixed-mode crack growth histories.

Figure 6.5 shows the mode I toughness of each material following a precracking mode I to mode II ratio of 1 to 4. Of the ratios we used, this ratio had the highest amount of mode II loading. The two toughened materials (solid symbols in Fig. 6.5) showed a significantly lower (40% to 70%) mode I toughness at early stages in crack growth relative to the steady state toughness. The two untoughened systems (open symbols in Fig. 6.5) showed little or no effect from this predominantly mode II precracking.

It is interesting to cross-plot the results and give plots for a single material at the three different mode ratios. The results for AS4/3501-6 and for IM7/XLASC at the three different precracking

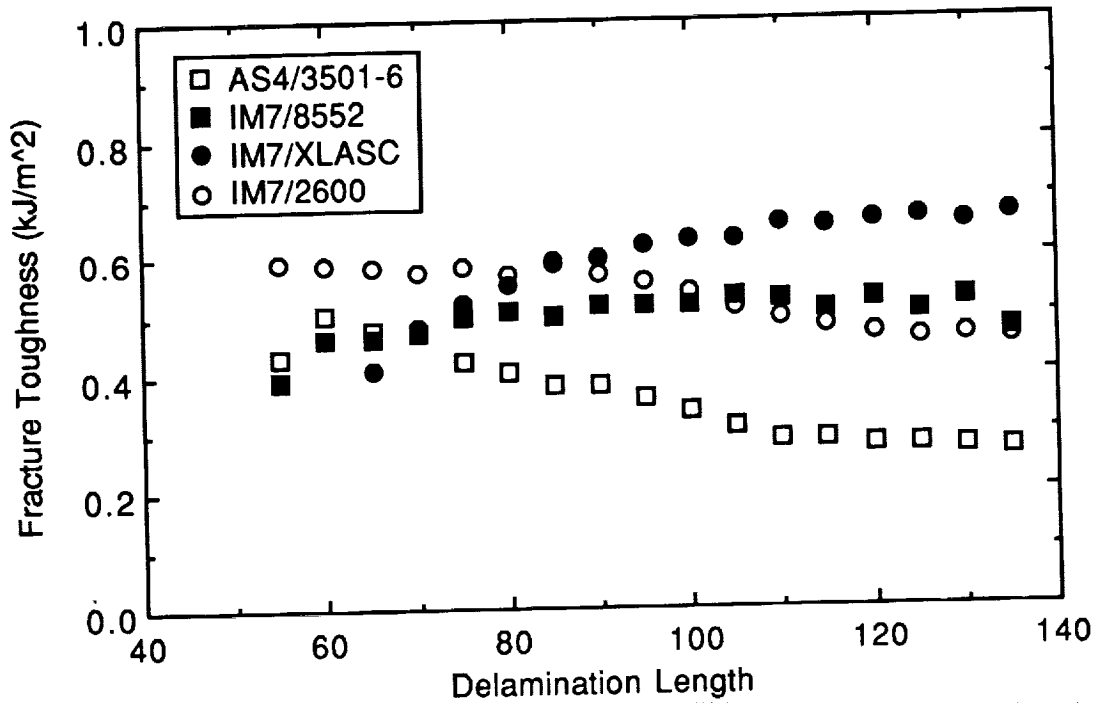


Figure 6.4: Mode I fracture toughness as a function a delamination length for all materials following mixed-mode precracking using a mode I to mode II ratio of 1:1

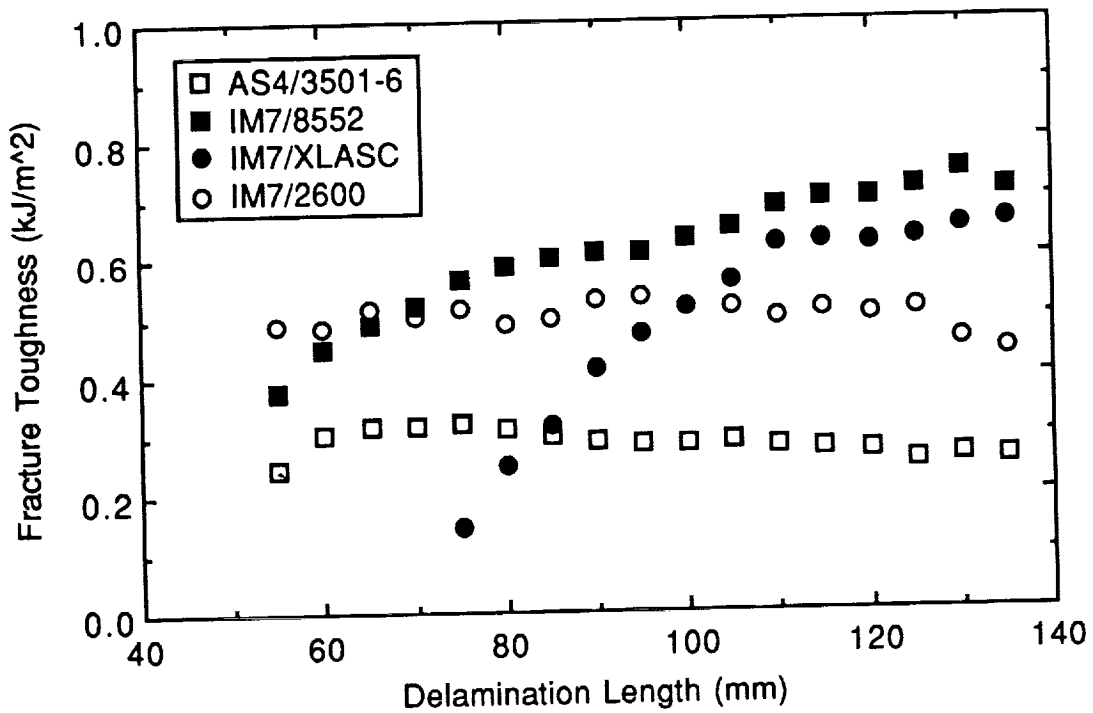


Figure 6.5: Mode I fracture toughness as a function a delamination length for all materials following mixed-mode precracking using a mode I to mode II ratio of 1:4

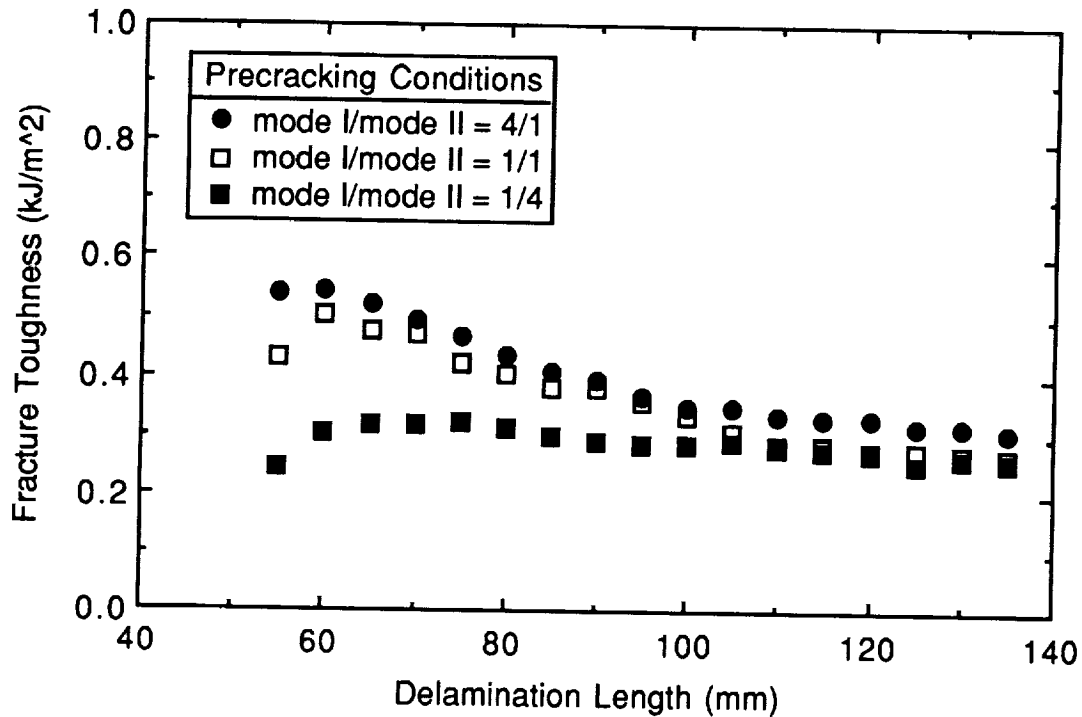


Figure 6.6: Mode I fracture toughness as a function of delamination length for AS4/3501-6 laminates following different mixed-mode precracking using different mode I to mode II ratios.

mode ratios are shown in Figs. 6.6 and 6.7, respectively. The untoughened AS4/3501-6 laminates showed no effect of precracking or a slightly higher mode I toughness at early stages of crack growth. The increase in mode I toughness got larger as the amount of mode I loading in the precracking increased. The IM7/XLASC laminates, which were toughened with an interlayer, showed only a lower mode I toughnesses at early stages of crack growth. The decrease in mode I toughness got larger as the amount of mode II loading in the precracking increased. After the most extreme mode II precracking (mode I to mode II ratio of 1 to 4), the initial mode I toughness of IM7/XLASC was 70% lower than its steady state toughness. The results for the second untoughened material, IM7/2600, were similar to those of AS4/3501-6. Likewise, the results for the second toughened material, IM7/8552, were similar to those of IM7/XLASC.

To gain some insight into mechanisms, we observed the fracture surfaces of the precrack and of the mode I crack. There was a distinct contrast between the two regions showing that the

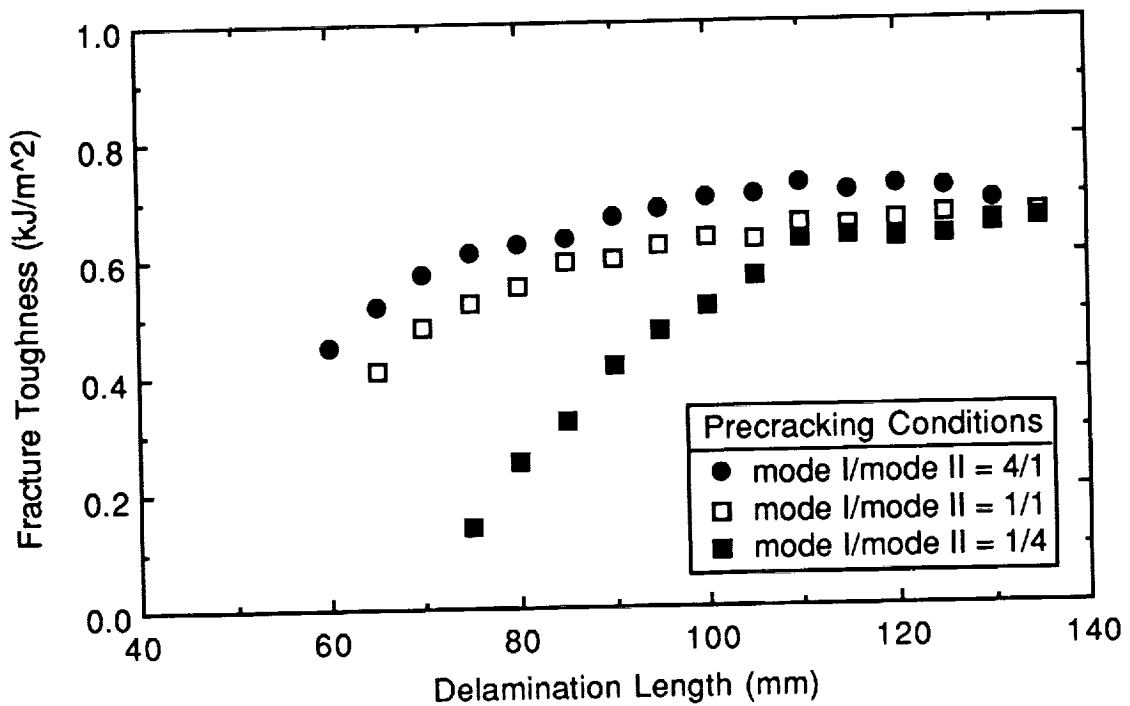


Figure 6.7: Mode I fracture toughness as a function of delamination length for IM7/XLASC laminates following different mixed-mode precracking using different mode I to mode II ratios.

delaminations grew by different growth mechanisms. As might be expected, the contrast was largest when using the mode I to mode II ratio of 1 to 4. As the amount of mode I loading in the precracking stage increased, the fracture surface contrast decreased. We attempted to assess the extent of fiber bridging. There appeared to be significantly more fiber bridging in the mode I fracture surface than in the precracking fracture surface.

6.4 Discussion and Conclusions

Our experimental results show that the mixed-mode precracking can have a profound effect on the initial mode I fracture toughness of subsequent mode I crack growth. The precracking can cause mode I toughness increases as high as 40% as well as mode I toughness decreases as high as 70%. These increases and decreases are relative to the steady state toughness for each material. Surprisingly, we found that the effect of the precrack persists for a macroscopic distance of about

60 mm. After 60 mm of crack growth all specimens approached a steady state mode I fracture toughness.

The two toughened materials, IM7/8552 and IM7/XLASC, tended to show decreases in mode I toughness following mixed-mode precracking. The amount of decrease increased as the mode II component of the precracking increased. We can arrive at a speculation for the effect of mode II precracking on mode I toughness by considering mode II stress states around crack tips in isotropic, homogeneous materials. When a material can yield easily, the singular stresses near the crack tip are more realistically imagined as being limited by the yielding process. If one assumes a yield criterion (*e.g.* Von Mises or Tresca), it is possible to estimate the yield zone size for any loading condition. For delamination specimens, the most relevant dimension of the yield zone is the one directly ahead of the crack tip. For plane-strain conditions in isotropic, homogeneous materials, the extent of yielding ahead of the crack tip is profoundly affected by stress state. It is at a minimum for pure mode I loading and increases dramatically as the amount of mode II loading increases.

To interpret the results in this paper, we suggest that the rubber toughened matrix in IM7/8552 and the toughening interlayer in IM7/XLASC are prone to yielding or have a low yield strength. During the precracking stage, any mode II loading will therefore lead to a yielded damage zone ahead of the crack tip. We suggest that the mode I toughness of the damage zone is low and thus precracking causes an initial reduction in mode I toughness. This model predicts that the larger the amount of mode II loading, the larger would be the reduction in mode I toughness. This prediction agrees with the observations in Fig. 6.7. The AS4/3501-6 and IM7/2600 laminates are different because their untoughened matrices have higher yield strengths. The observation that mode II precracking does not decrease their subsequent mode I toughness suggests that the higher yield strength matrices did not become damaged by the mode II loading present during precracking.

When the precracking mode I to mode II ratio was 4 to 1, we observed an increased initial mode

I toughness (see Fig. 6.3). It is difficult to imagine a precracking mechanism that would enhance the subsequent mode I toughness. The increase could possibly be related to fibers bridging from the precrack zone into the mode I crack growth. However, we have no evidence to prove or disprove this claim. For now, the apparent increase in mode I toughness remains unresolved.

In conclusion, the closer we look, the more we realize that the characterization of delamination toughness is a complex problem. It is clearly insufficient to study only mode I, mode II, or mixed-mode crack growth emanating from a crack starter. The delamination process is now seen to have *memory*. In other words, the delamination toughness is not only a function of the loading conditions but also a function of the loading conditions that gave the initial crack. A good example from this paper concerns the development of tougher composites. The IM7/8552 and IM7/XLASC composites are tougher materials by standard mode I testing. When subjected to precracking with a high component of mode II loading, however, these materials become less tough than untoughened composite systems. The design implication is that *so-called* toughened materials will not always produce tougher structures than their untoughened counterparts. We suggest there is something deficient, or rather specific, about the toughening mechanisms taking place in today's toughened composites. Their toughening mechanisms work for mode I loading but can be rendered ineffective by various precracking conditions

Bibliography

- 1 B. W. Rosen, "Mechanics of Composite Strengthening," in *Fiber Composite Materials*, pp. 37-75 (American Society of Metals, Metals Park, Ohio, 1964).
- 2 P. D. Ewins and R. T. Potter, "Some Observations on the Nature of Fibre Reinforced Plastics and Implications for Structural Design," *Phil Trans. R. Soc. Lond.*, **A294**, 507-517 (1980).
- 3 A. Proctor and P. M. A. Sherwood, "X-Ray Photoelectron Spectroscopic Studies of Carbon Fiber Surfaces. I. Carbon Fibre Spectra and the Effects of Heat Treatment," *J. Electron Spectroscopy and Related Phenomena*, **27**, 39 (1982).
- 4 T. Takahagi and A. Ishitani, "XPS Studies by use of the Digital Difference Spectrum Technique of Functional Groups on the Surface of Carbon Fibers," *Carbon*, **22**, 43 (1984).
- 5 R. L. Brady and R. S. Porter, "Interfacial Crystallization and Adsorption in Polycarbonate/Carbon Fiber Composites," *J. Thermoplastic Comp.*, **2**, 164-171 (1989).
- 6 R. L. Brady, R. S. Porter, and J. A. Donovan, "A Buckled Plate Test to Measure Interfacial Toughness in Composites," *J. Mat. Sci.*, **24**, 4138-4143 (1989).
- 7 W. D. Bascom and L. T. Drzal, "The Surface Properties of Carbon Fibers and Their Adhesion to Organic Polymers," NASA Contractor Report 4084, Contract NAS1-17918 (1987).

- 8 L. T. Drzal, M. J. Rich, J. D. Canning, and W. J. Park, "Interfacial Shear Strength and Failure Mechanisms in Graphite Fiber Composites," *Proc. 35th Conf. SPI Reinforced Plastics Div.*, Section 20-C, 1 (1980).
- 9 L. T. Drzal, M. J. Rich, and P. F. Lloyd, "Adhesion of Graphite Fibers to Epoxy Matrices: I. The Role of Fiber Surface Treatment," *J. Adhesion*, **16**, 1 (1983).
- 10 L. T. Drzal, M. J. Rich, M. F. Koenig, and P. F. Lloyd, "Adhesion of Graphite Fibers to Epoxy Matrices: II The Effect of Fiber Finish," *J. Adhesion*, **16**, 133-152 (1983).
- 11 L. T. Drzal, M. J. Rich, and M. F. Koenig, "Adhesion of Graphite Fibers to Epoxy Matrices: III. The Effect of Hygrothermal Exposure," *J. Adhesion*, **18**, 49-72 (1985).
- 12 M. J. Rich and L. T. Drzal, "Interfacial Properties of Some High-Strain Carbon Fibers in an Epoxy Matrix," *Proc. 41st Conf. SPI Reinforced Plastics Div.*, Section 2-F, 1 (1986).
- 13 W. D. Bascom and R. M. Jensen, "Stress Transfer in Single Fiber/Resin Tensile Tests," *J. Adhes.*, **19**, 219 (1986).
- 14 L. DiLandro, A. T. DiBenedetto, and J. Groeger, "The Effect of Fiber-Matrix Stress Transfer on the Strength of Fiber-Reinforced Composite Materials," *Polym. Comp.*, **9**, 209-221 (1988).
- 15 A. N. Netravali, R. B. Henstenburg, S. L. Phoenix, and P. Schwartz, "Interfacial Shear Strength Studies Using the Single-Filament-Composite Test. I: Experiments on Graphite Fibers in Epoxy," *Polym. Comp.*, **10**, 226-241 (1989).
- 16 W. D. Bascom, K-J. Yon, R. M. Jensen, and L. Cordner, "The Adhesion of Carbon Fibers to Thermoset and Thermoplastic Polymers," *J. Adhesion*, **34**, 79-98 (1991).

- 17 B. Yavin, H. E. Gallis, J. Scherf, A. Eitan, and H. D. Wagner, "Continuous Monitoring of the Fragmentation Phenomenon in Single Fiber Composite Materials," *Polym. Comp.*, **12**, 436 (1991).
- 18 N. Melanitis, C. Galiotis, P. L. Tetlow, and C. K. L. Davies, "Interfacial Shear Stress Distribution in Model Composites Part 2: Fragmentation Studies on Carbon Fibre/Epoxy Systems," *J. Comp. Mat.*, **26**, 574 (1992).
- 19 J. A. Nairn, "A Variational Mechanics Analysis of the Stresses Around Breaks in Embedded Fibers," *Mech. of Materials*, **13**, 131-154 (1992).
- 20 P. M. Knauer, "Single Carbon Fiber Flaw Characteristics," BS Thesis, Material Science and Engineering Department, University of Utah, 1990.
- 21 D. J. Boll, R. M. Jensen, L. Cordner, and W. D. Bascom, "Compression Behavior of Single Carbon Filaments Embedded in an Epoxy Polymer," *J. Comp. Mat.*, **24**, 208 (1990).
- 22 M. J. Folkes and W. K. Wong, "Determination of Interfacial Shear Strength in Fibre-Reinforced Thermoplastic Composites," *Polymer*, **28**, 1309 (1987).
- 23 J. B. Ha, "The Compression Study of Unidirectional Single-Ply Composites," PhD Thesis, Material Science and Engineering Department, University of Utah, 1992.
- 24 W. D. Bascom, J. A. Nairn, and D. J. Boll, "Studies of Fiber-Matrix Adhesion on Compression Strength," *Proc of the 1st NASA Advanced Comp. Tech. Conf.*, Seattle, WA, Oct. 29 to Nov. 1, 1990 (1990).
- 25 E. M. Odom and D. F. Adams, "Failure Modes of Unidirectional Carbon/Epoxy Composite Compression Specimens," *Composites*, **21**, 289 (1990).

- 26 D. C. Leach, "Continuous Fibre Reinforced Thermoplastic Matrix Composites," in *Advanced Composites*, pp. 43-109 (ed., I. K. Partridge, Elsevier Applied Science, London, 1989).
- 27 Hercules Carbon Fiber Product Data Sheets, Hercules, Inc., Hercules Plaza, Wilmington, DE 19895.
- 28 J. L. Kardos, "Regulating the Interface in Graphite/Thermoplastic Composites," *J. Adhesion*, **5**, 119-138 (1973).
- 29 J. L. Kardos, F. S. Cheng, and T. L. Tolbert, "Tailoring the Interface in Graphite-Reinforced Polycarbonate," *Polym. Eng. & Sci.*, **13**, 455-461 (1973).
- 30 T. Bessel and J. B. Shortall, "The Crystallization and Interfacial Bond Strength of Nylon 6 at Carbon and Glass Fibre Surfaces," *J. Mat. Sci.*, **10**, 2035-2043 (1975).
- 31 P. O. Frayer and J. B. Lando, "Polymerization in Electric Fields of Hexamethylenediammonium Adipate Crystallized on Graphite Fibers," *J. Polym. Sci., Polym. Lett. Ed.*, **10**, 29-34 (1972).
- 32 F. Tuistra and E. Baer, "Epitaxial Crystallization of Polyethylene on Graphite," *J. Polym. Sci., Polym. Lett. Ed.*, **8**, 861-865 (1970).
- 33 S. Y. Hobbs, "Row Nucleation of Isotactic Polypropylene on Graphite Fibers," *Nature Phys. Sci.*, **234**, 12-13 (1971).
- 34 D. Campbell and M. M. Qayyum, "Melt Crystallization of Polypropylene: Effect of Contact with Fiber Substrates," *J. Polym. Sci., Polym. Phys. Ed.*, **18**, 83-93 (1980).
- 35 D. Campbell and M. M. Qayyum, "Enhanced Fracture Strain of Polypropylene by Incorporation of Thermoplastic Fibres," *J. Mat. Sci.*, **12**, 2427-2434 (1977).

- 36 Y. C. Lee and R. S. Porter, "Crystallization of Poly(etheretherketone) PEEK in Carbon Fiber Composites," *Polym. Eng. & Sci.*, **26**, 633-639 (1986).
- 37 P. Chang and J. A. Donovan, "Crack Size Independence of the Crack Driving Force in the Buckled Plate Specimen," *J. Mat. Sci.*, **24**, 816-820 (1989).
- 38 J. M. Jonza and R. S. Porter, "High-Melting Bisphenol-A Polycarbonate from Annealing of Vapor Induced Crystals," *J. Polym. Sci., Polym. Phys. Ed.*, **24**, 2459-2472 (1986).
- 39 "Standard Test Method for Density of Plastics by the Density-Gradient Technique," ASTM Designation D1505-68, Method C (Continuous Filling with Liquid Entering Gradient Tube Becoming Progressively More Dense), American Society for Testing and Materials (1968).
- 40 J. B. Ha and J. A. Nairn, "Compression Failure Mechanisms of Unidirectional Single-Ply Composites," *SAMPE Quarterly*, **23**, 29 (1992).
- 41 P. Maivald, H. J. Butt, S. A. C. Gould, C. B. Prater, B. Drake, J. A. Gurley, V. B. Elings, and P. K. Hansma, "Using Force Modulation to Image Surface Elasticities with the Atomic Force Microscope," *Nanotechnology*, **2**, 103-106 (1991).
- 42 P. D. Ewins and R. T. Potter, "Some Observations on the Nature of Fibre Reinforced Plastics and Implications for Structural Design," *Phil Trans. R. Soc. Lond.*, **A294**, 507-517 (1980).
- 43 J. R. Reeder and J. H. Crews, Jr., "Nonlinear Analysis and Redesign of the Mixed-Mode Bending Delamination Test," *NASA Technical Memorandum 102777*, 1991.
- 44 J. R. Reeder and J. H. Crews, Jr., "Mixed Mode Bending Method for Delamination Testing," *AIAA J.*, **28**, 1270-1276 (1990).
- 45 S. Hashemi, A. J. Kinloch, and J. G. Williams, "The Analysis of Interlaminar Fracture in Uniaxial Fibre Reinforced Polymer Composites," *Proc. R. Soc. Lond.*, **A347**, 173-199 (1990).



REPORT DOCUMENTATION PAGE			Form Approved OMB No. 0704-0188	
Public reporting burden for this collection of information is estimated to average 1 hour per response, including the time for reviewing instructions, searching existing data sources, gathering and maintaining the data needed, and completing and reviewing the collection of information. Send comments regarding this burden estimate or any other aspect of this collection of information, including suggestions for reducing this burden, to Washington Headquarters Services, Directorate for Information Operations and Reports, 1215 Jefferson Davis Highway, Suite 1204 Arlington, VA 22202-4302, and to the Office of Management and Budget, Paperwork Reduction Project (0704-0188), Washington, DC 20503.				
1. AGENCY USE ONLY (Leave blank)	2. REPORT DATE May 1994	3. REPORT TYPE AND DATES COVERED Contractor Report		
4. TITLE AND SUBTITLE Effects of Fiber, Matrix, and Interphase on Carbon Fiber Composite Compression Strength			5. FUNDING NUMBERS C NAS1-18883 WU 510-02-11	
6. AUTHOR(S) John A. Nairn, Sheila I. Harper and Willard D. Bascom				
7. PERFORMING ORGANIZATION NAME(S) AND ADDRESS(ES) University of Utah Department of Materials Science and Engineering 304 EMRO Building Salt Lake City, Utah 84112			8. PERFORMING ORGANIZATION REPORT NUMBER	
9. SPONSORING / MONITORING AGENCY NAME(S) AND ADDRESS(ES) National Aeronautics and Space Administration Langley Research Center Hampton, Virginia 23681-0001			10. SPONSORING / MONITORING AGENCY REPORT NUMBER NASA CR-4601	
11. SUPPLEMENTARY NOTES Langley Technical Monitor - Jeffrey A. Hinkley Final Report				
12a. DISTRIBUTION / AVAILABILITY STATEMENT Unclassified/Unlimited Subject Category 24			12b. DISTRIBUTION CODE	
13. ABSTRACT (Maximum 200 words) The major goal of this project was to obtain basic information on compression failure properties of carbonfiber composites. To do this, we investigated fiber effects, matrix effects and fiber/matrix interface effects. Using each of nine fiber types, we prepared embedded single-fiber specimens, single-ply specimens and full laminates. From the single-fiber specimens, in addition to the standard fragmentation test analysis, we were able to use the low crack density data to provide information about the distribution of fiber flaws. The single-ply specimens provided evidence of a correlation between the size of kink band zones and the quality of the interface. Results of the laminate compression experiments mostly agreed with the results from single-ply experiments, although the ultimate compression strengths of laminates were higher. Generally, these experiments showed a strong effect of interfacial properties. Matrix effects were examined using laminates subjected to precracking under mixed-mode loading conditions. A large effect of precracking conditions on the mode I toughness of the laminates was found. In order to control the properties of the fiber/matrix interface, we prepared composites of carbon fiber and polycarbonate and subjected these to annealing. The changes in interfacial properties directly correlated with changes in compression strength.				
14. SUBJECT TERMS Composites, Interfaces, Compression, Delamination			15. NUMBER OF PAGES 112	
			16. PRICE CODE A06	
17. SECURITY CLASSIFICATION OF REPORT Unclassified	18. SECURITY CLASSIFICATION OF THIS PAGE Unclassified	19. SECURITY CLASSIFICATION OF ABSTRACT Unclassified	20. LIMITATION OF ABSTRACT	

